UC Riverside
UC Riverside Electronic Theses and Dissertations

Title

Layered Dependence of the Magneto Transport Properties of Metallic Ferromagnets: Fe5Ge2Te2, Fe3GeTe2

Permalink

https://escholarship.org/uc/item/5np9c96g

Author

Alghamdi, Mohammed

Publication Date

2022

Supplemental Material

https://escholarship.org/uc/item/5np9c96g#supplemental

Peer reviewed|Thesis/dissertation

UNIVERSITY OF CALIFORNIA
RIVERSIDE

Layered Dependence of the Magneto Transport Properties of Metallic Ferromagnets:
$Fe_5Ge_2Te_2$, Fe_3GeTe_2

A Dissertation submitted in partial satisfaction of
the requirements for the degree of

Doctor of Philosophy

in

Physics

by

Mohammed A. Alghamdi

March 2022

Dissertation Committee:

    Dr. Jing Shi, Chairperson
    Dr. Boniface P. T. Fokwa
    Dr. Peng Wei

The Dissertation of Mohammed A. Alghamdi is approved:

_____

_____

_____
Committee Chairperson

University of California, Riverside

Acknowledgement of previously published material

To my parents for faithful support

To my wife for all her much-needed support

To my kids for their fun support

ABSTRACT OF THE DISSERTATION

Layered Dependence of the Magneto Transport Properties of Metallic Ferromagnets:
$Fe_5Ge_2Te_2$, Fe_3GeTe_2

by

Mohammed A. Alghamdi

Doctor of Philosophy, Graduate Program in Physics
University of California, Riverside, March 2022
Dr. Jing Shi, Chairperson

The recent advent of 2D atomically layered ferromagnetic materials has brought a great deal of excitement in condensed matter physics and materials science. Despite the intense ongoing research, the physics of many fascinating phenomena is still not completely understood. We explore several physical properties of a special type of 2D ferromagnets: Fe_3GeTe_2 (FGT) and $Fe_5Ge_2Te_2$ (FG2T) in my dissertation research. FGT and FG2T are layered metallic ferromagnets with the phase transition from paramagnetic to ferromagnetic phase near room temperature, the highest among other known 2D magnets. The high Curie temperature, strong magnetic anisotropy, and the metallicity make them the best candidate materials for the next generation of high-density memory and logic devices.

In this dissertation, I will present my study of the 2D FGT and FG2T nanodevices from the perspective of magneto-transport measurements. I present and discuss the fabrication process challenges in fabricating FGT and FG2T flakes with nanometer dimensions, the layer dependence of the low-temperature Kondo behaviors and the linear

magnetoresistance, and the layer dependence of the perpendicular magnetic anisotropy field, Curie temperature, longitudinal and anomalous Hall conductivities. In addition, I will discuss the effect of the spin current generated in Pt on the FGT magnetization reversal due to the damping-like spin-orbit torque. Also, we quantify the magnitude of the SOT effect by measuring the second harmonic Hall responses as the applied magnetic field rotates the FGT magnetization in the plane.

Table of Contents

List of Figures

Chapter 1

Introduction

1.1 VdW ferromagnetic material

Two-dimensional (2D) atomically layered systems, "our generation's glory", are considered the major exciting research frontier in condensed matter physics because they offer us an opportunity to study truly 2D physics. This research field started when a single layer of carbon atoms (graphene) was successfully exfoliated, and its electrical properties were measured in 2004.[1] This breakthrough was quickly reproduced in a large number of cleavable materials with different crystal structures including {G, BN, MX, YGX (G-group 14 elements, M-transition metals, X-chalcogen, Y-group 8 elements)}. The existence of the weak interlayer VdW force between layers enables us to precisely control the layer numbers. Searching for new physics in 2D materials becomes a necessity especially for magnetic materials due a magnetic ordering that is very useful in spintronic applications.[2-12]

2D magnetic materials represented by Fe_3GeTe_2 (FGT), $Cr_2Ge_2Te_6$ (CGT), and CrI_3. have unique magnetic properties. They are ideal for studying the basic 2D magnetism and for fabricating heterostructures with other 2D materials. Recently, 2D magnetic monolayer flakes have been exfoliated and their magneto-transport properties have been measured. The fact that a monolayer ferromagnet holds its magnetic order itself is fascinating. Many reports showed layer-dependent magnetism down to a single layer. FGT is a metallic near room temperature ferromagnet with a high anisotropy energy. Magnetic properties have layer-number dependence and can be gate tuned to enhance its ferromagnetism above

room temperature. CGT is a semiconductor with a band gap of 0.95 eV, Curie temperature of 80 K, and magnetic anisotropy energy of (1.4×10^5 erg/cm^3 vs 1.1×10^7 erg/cm^3 at 4 K) lower than FGT.[11-16] CrI$_3$ bulk is ferromagnetic but thin layers have an antiferromagnetic interlayer interaction.[17] The ferromagnetic state was achieved in bilayer CrI$_3$ from antiferromagnetic state by gating.[18] These materials are considered the next generation materials to be used for high-density memory and logic devices.

Understanding the 2D ferromagnetism of a single 2D atomic layer and the interlayer exchange interaction in multi-atomic layers is very important. 2D magnetic materials provide an opportunity for us to study phenomena in truly 2D magnetic systems. The gate tunability of 2D magnet materials further gives us the ability to investigate interesting quantum physics in thin 2D layers and heterostructure. The focus of my study in this dissertation is on the metallic FGT and Fe$_5$Ge$_2$Te$_2$ (FG2T) discussed several different properties. We will go over the crystal structure, fabrication process, the magneto-transport measurements, and finally the spin-orbit torque in FGT/Pt heterostructures as an application.

FGT has a hexagonal structure with a space group of P6$_3$/mmc. It consists of a Fe-Ge layer sandwiched between two Te layers. As can be seen in **Fig. 1.1**. FGT has lattice parameters of a=3.991(1) Å and c=16.33(3) Å. Each unit cell consists of 2 layers of FGT with AB stacking. FG2T on the other hand is similar to the crystal structure of FGT with a space group of P-3m1 and the number of Ge/Fe layers building a slab is the basic difference. FG2T has lattice parameters of a=4.0121(3) Å and c=10.7777(8) Å. FG2T contains a 7 thick layer slab with two Ge/Fe layers while there are five in FGT with one

2

Ge/Fe in the center and both ended by a layer of Te on each side. The stacking of extra 2 layers of Fe and Fe-Ge required only a single slab per unit cell. Inter-slab interaction in FGT is weakly antiferromagnetic while FG2T is weakly ferromagnetic.[2-7,11,12,16]

The Curie temperature of FGT is high compared to other 2D magnets and it can be further tuned up to above room temperature. Many groups have reported[2-5] a drop in Curie temperature below 5 layers of FGT from steady bulk value using different techniques such as RMCD and magneto-transport measurements. Even growth of FGT films by molecular beam epitaxy was successfully demonstrated and a thickness dependence of Curie temperature was reported.[6] Not only the high Curie temperature, but also the high anisotropy energy and metallic behavior are attractive for practical applications employing FGT. It is important to show a layer-dependence of a new physics quantity. For example, the longitudinal resistivity, the anomalous Hall conductivity, anisotropy field, and Kondo temperature.

Fe₃GeTe₂		Distance/Å
	Fe1-Fe1	2.554
$P6_3/mmc$	Fe1-Fe2	2.634
$a = 3.991(1)$ Å		
$c = 16.33(3)$ Å	Te-Te	3.740

Fe₅Ge₂Te₂		Distance/Å
	Fe1-Fe2	2.579
P-3m1	Fe1-Fe3	2.689
$a = 4.001(1)$ Å	Fe2-Fe3	2.604
$c = 10.837(2)$ Å	Te-Te	3.728
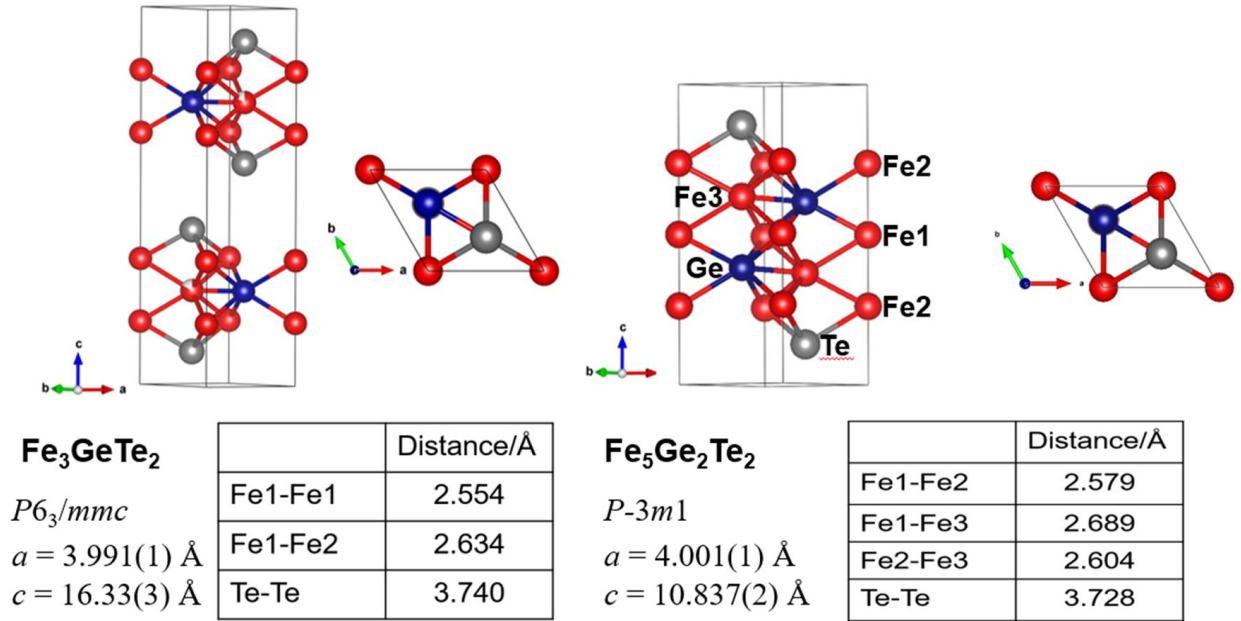
Fig. 1.1. Crystal Structure of FGT and FG2T. The crystal structure of FGT consists of 2 layers with a total thickness of 1.6 nm for both layers while FG2T has a single layer with a thickness 1.08nm.

1.2 Longitudinal resistance

One of the methods to examine the material properties is the transport measurements. This measurement technique provides information about the band structure and electron scattering mechanism which are considered as the basic electronic properties of the material. Electrical voltage and current signals are the collected data from the circuit shown in **Fig. 1.2**. The resistance is derived from the voltage and current signals as a function of external parameters such as temperature, magnetic field, and gate voltage. **Fig. 1.2** shows a typical layout of the measurement configuration for measuring the 2-terminal, 4-terminal, and Hall resistances. When the voltage and current are taken from the same pair of electrodes, it is the 2-terminal measurement. This simple measurement is usually used in a neglected contact resistance compared to the sample resistance.
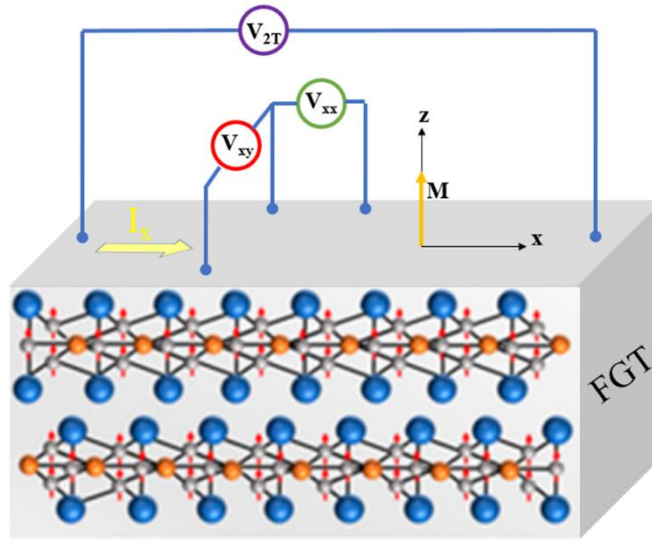
Fig. 1.2 Magneto-Transport Measurement Set. shows an illustration of the measurement style. The current is in the x-axis. 2-terminal measurement is source-drain measurements. V_{xx} is the voltage drop along the channel. V_{xy} the voltage drops across the channel. The FGT magnetization is out-plane all the time in the z-axis.

The 4-terminal [longitudinal resistance (LR)] resistance measurement is a basic method

to characterize the material's transport property in the presence or absence of a magnetic

field. It is the voltage drop between a pair of electrodes in a part of the sample divided by

the driving current from a different pair of electrodes which is usually supplied by a

constant current source. When we measure the longitudinal resistance, we still want to have

low contact resistance even though it does not include the contact resistance. Obtaining

low contact resistance itself is a challenge in FGT due to degradation and oxidation during

contact opening and contact metal deposition. We added a new additional step in the

fabrication to achieve it as will be discussed in Chapter 2.

Longitudinal resistivity (ρ_{xx}) is the quantity used to compare the electric properties of

different materials because it does not depend on the material volume or shape. The sample

cross-section and electrode separation length are required to calculate ρ_{xx} and it represents

5

the intrinsic property. It is given by $\rho_{xx}=R_{xx}A/L$, where R_{xx} is LR and A is cross-sectional area [the width (W) multiplied by thickness (t)], and L is the distance between the two voltage electrodes. Its value is used to characterize the material (metal, semiconductor). For 2D materials, the devices are usually micro-sized exfoliated flakes on a large wafer and the flake geometry is found by using an atomic force microscope and the optical microscope. The flake width is only taken in the active measurement part between the electrodes. FGT is a poor metal if we compare its longitudinal resistivity with Gold (~2 micro-Ohm.cm) or Copper (~1.7 micro-Ohm.cm) at room temperature. The range of the measured longitudinal resistivity of FGT is found to be between 200 to 1000 micro-Ohm.cm and around 405 micro-Ohm.cm for FG2T which is an indication of metallic nature of FGT.[2-6,11] One question about thin flake devices is whether this value depends on the layer number as the thickness is reduced. Does the monolayer have the same bulk value of ρ_{xx}?

Magnetoresistance (MR) is mainly the effect of LR of the material in the presence of a magnetic field. The parabolic MR is present in most materials (metals, semiconductor, insulators) due to the effect of the Lorentz force, but the linear magnetoresistance is unusual and only found in some materials.[19-21] It is important to measure the MR in 2D materials to understand the effect of the magnetic field. Negative MR found in metals containing magnetic impurities and ferromagnetic metals due to suppression of spin disorders. Here spin disorders can be random orientation of local moments (for impurities) or spin waves (for ordered FM). While positive MR is found in non-magnetic metals and today the

semimetals show interesting behaviors at low thickness. FGT is an example of quasi semimetals, and it will be exciting to study its MR response as a function of layer-number.

Hall effect measures the transverse resistance in the Hall channel orthogonal to the current direction and in the presence of a perpendicular magnetic field due Lorentz force. Or so-called ordinary Hall effect discovered by Hall in 1879 by probing a cross voltage drop through an active current flowing in a gold leaf (nonmetallic material). Introducing a magnetic field as an external parameter he found a nonsystematic linear response. This voltage drop happened because of the charge pushed to the sample edge and it was the beginning to examine the different material response. Later, he tested different ferromagnetic metals and found the response no longer linear. It began to increase sharply and saturate at a certain high magnetic field. Then anomalous Hall (AH) effects become a tool to examine any conducting magnetic materials.[22,23] AH effect happens in solids with broken time-reversal symmetry in the ferromagnetic state. For example, FGT has a linear Hall response with a magnetic field at paramagnet state above Curie temperature. While in the ferromagnetic state the AH dominates. AH resistance is generated from the magnetism and spin-orbit coupling (SOC).[22-23]

AH resistance saturates above a certain magnetic field, and it is empirically proportional to the magnetization. This concept can also be used to describe the magnetization as a function of temperature. AH resistivity was introduced as $\rho_{xy} = R_o H_z + R_s M_z$ where the first part on the right-hand side of this equation is the ordinary Hall part that contains only the linear dependence of the magnetic field, while the second part is proportional to the magnetization (**See Fig. 1.3**). Notice that it does not depend on the

applied magnetic field and only can be explained by the magnetic moment inside the magnetic material.[22-23]
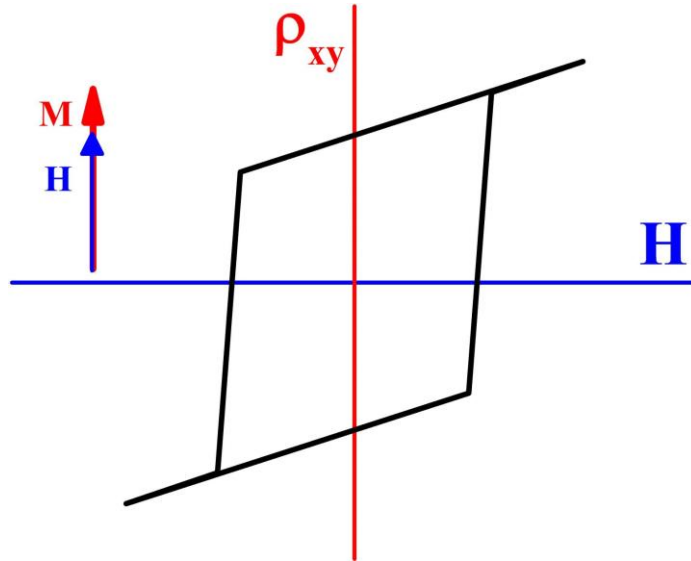
Fig. 1.3 Field Dependance of Typical Response of AH resistivity. The AH resistivity is calculated from the magento-transport measurements. The equation to describe this plot is $\rho_{xy} = R_oH_z + R_sM_z$.

FGT and FG2T both have perpendicular magnetic anisotropy, and the anisotropy axis is perpendicular to the atomic planes. In the AH experiments, we sweep the perpendicular magnetic field and monitor the AH resistance. The AH response shows magnetic hysteresis loops, just as the magnetization as a function of the applied field. At zero magnetic field, there are bi-stable states and therefore two different AH resistance values. The saturation AH resistance is proportional to material magnetization and widely used in transport measurements as a tool to identify magnetism. In 2D ferromagnets, in the limit where the thickness goes to zero it is fairly said that $\rho_{xy}=R_{xy}$. The AH effect is related to SOC of the ferromagnets that can be caused by either intrinsic or extrinsic mechanism. Understanding the physical origin of the AH effect has been an important topic in condensed matter

physics for decades. Now it is interesting to explore the dimensionality effect on AH physics especially in the 2D limit in FGT and FG2T. **Fig. 1.3** shows an illustration of the Hall effect and AH effect.[24]
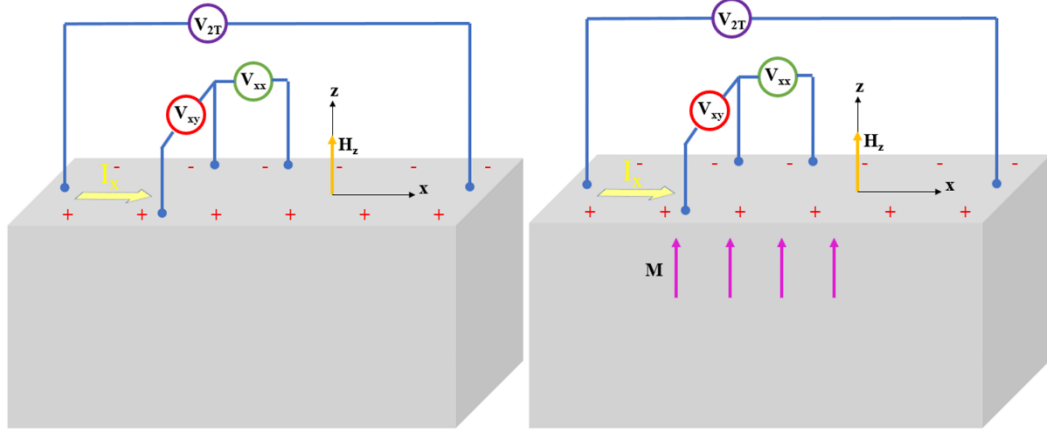
Fig. 1.3. Transport Measurement Set. This is an illustration of the transport measurements set of the Hall effect (left) and AH effect(right.)

The ability of the material to conduct electricity is called longitudinal conductivity σ_{xx} or the inverse of the resistivity. The general definition of the conductivity tensor must be used in term of the longitudinal resistivity and AH hall resistivity and given by

$$\sigma_{xx}=\rho_{xx}/(\rho^2_{xx}+\rho^2_{xy}) \text{ and } \sigma_{xy}=-\rho_{xy}/(\rho^2_{xx}+\rho^2_{xy}) \quad\quad (1.1)$$

where ρ_{xx} is the longitudinal resistivity and giving by $\rho_{xx}=R_{xx}A/L$, and is the AH resistivity ρ_{xy} and giving by $\rho_{xy}=R_{xy}t$. In the case of a 2D system where thickness goes to zero (t→0), the 2D longitudinal and AH resistivities are defined as $\rho_{xx}=R_{xx}W/L$ and $\rho_{xy}=R_{xy}$. And the 3D conductivity unit changes from $(\Omega.m)^{-1}$ to 2D conductivity of the unit $(\Omega)^{-1}$. There is another unit of conductivity widely used in the 2D material world: e^2/h (25812.8 Ohms $=h/e^2$). The conductivity is similar to the resistivity used to describe the material. If we find that the 2D conductivity is proportional to the number of layers, it means that each layer

for the 2D ferromagnet contributes equally to the conductance. This itself is worth investigating as the number of layers varies.[24]

FGT and FG2T have uniaxial magnetic anisotropy in c-axis as shown in **Fig 1.1**. The magnetic anisotropy energy (MAE) is given by MAE=K_u $Sin^2\Theta$ as shown in **Fig. 1.4**. The anisotropy field H_k is the field required to saturate all the moments when the field is applied perpendicular to the easy axis at zero degree. It is giving by H_k=2K_u/M_s where K_u is the magnetic anisotropy constant and M_s is the material saturated magnetization. Another quantity is the coercive field H_c, in a single domain material H_k=H_c. But this is not the case if there is the presence of multi domains in this case H_k>H_c. The anisotropy field for perpendicular anisotropy can be found from the transport measurement for AH resistance after aligning the magnetic field in-plane. The easy axis when it is parallel to the material magnetization, we can find the field required to saturate the AH voltage signal and so called the coercive field H_c.[5,7]
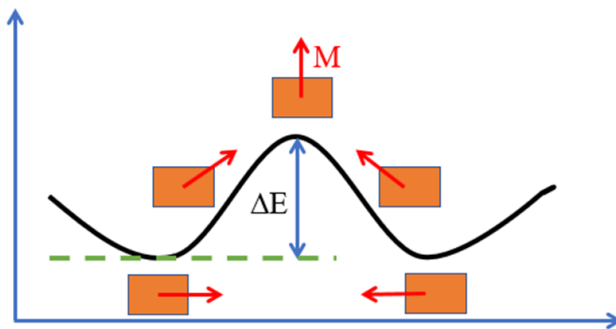
Fig. 1.4 Uniaxial Anisotropy Energy Representation.

1.3 Spin orbit torques

If we consider a bilayer system consisting of a heavy metal and a ferromagnetic material. If a charge current flows in the heavy metal, because of strong SOC, it generates a spin current due to the spin Hall effect. Then, this spin current is injected from the heavy metal into the ferromagnet and transfers angular momentum that exerts a torque to local magnetic moments. There are two kinds of torque namely damping-like torque (DLT) and field-like torque (FLT). DLT is dominant in the magnetization switching while FLT is effectively reducing the critical switching current and accelerating the switching process. If the ferromagnet is a metal, we need to consider the effective charge current in the heavy metal using a parallel resistance model. In Chapter 5 we discuss the SOT in FGT/Pt heterostructure and **Fig. 1.5** illustrates the studied system.[26-28]
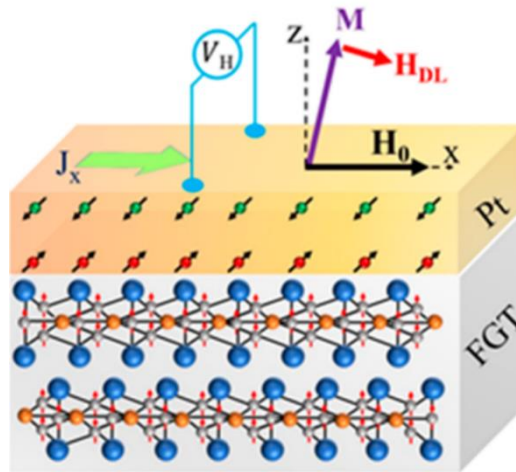
Fig. 1.5. SOT FGT/Pt Heterostructure device. Schematic illustration of the effective field responsible for switching the magnetic state of FGT in our FGT/Pt hybrid devices. J is the injected current density, H_x is the applied in-plane field, HDL is the effective field from damping-like SOT, and M is FGT`s magnetization.

References

1. Novoselov, K. S., Geim, A. K., Morozov, S. V., Jiang, D. E., Zhang, Y., Dubonos, S. V., ... & Firsov, A. A. (2004). Electric field effect in atomically thin carbon films. *science*, *306*(5696), 666-669.

2. Deng, Y., Yu, Y., Song, Y., Zhang, J., Wang, N. Z., Sun, Z., ... & Zhang, Y. (2018). Gate-tunable room-temperature ferromagnetism in two-dimensional Fe3GeTe2. *Nature*, *563*(7729), 94-99.

3. Fei, Z., Huang, B., Malinowski, P., Wang, W., Song, T., Sanchez, J., ... & Xu, X. (2018). Two-dimensional itinerant ferromagnetism in atomically thin Fe3GeTe2. *Nature materials*, *17*(9), 778-782.

4. Gong, C., Li, L., Li, Z., Ji, H., Stern, A., Xia, Y., ... & Zhang, X. (2017). Discovery of intrinsic ferromagnetism in two-dimensional van der Waals crystals. *Nature*, *546*(7657), 265-269.

5. Ta Tan, C., Lee, J., Jung, S. G., Park, T., Albarakati, S., Partridge, J., ... & Lee, C. (2018). Hard magnetic properties in nanoflake van der Waals Fe3GeTe2. *Nature communications*, *9*(1), 1-7.

6. Tan, C., Lee, J., Jung, S. G., Park, T., Albarakati, S., Partridge, J., ... & Lee, C. (2018). Hard magnetic properties in nanoflake van der Waals Fe3GeTe2. *Nature communications*, *9*(1), 1-7.

7. Liu, S., Yuan, X., Zou, Y., Sheng, Y., Huang, C., Zhang, E., ... & Xiu, F. (2017). Wafer-scale two-dimensional ferromagnetic Fe3GeTe2 thin films grown by molecular beam epitaxy. *npj 2D Materials and Applications*, *1*(1), 1-7.

8. Zhang, K., Han, S., Lee, Y., Coak, M. J., Kim, J., Hwang, I., ... & Park, J. G. (2021). Gigantic current control of coercive field and magnetic memory based on nanometer-thin ferromagnetic van der Waals Fe3GeTe2. Advanced Materials, 33(4), 2004110.

9. Lohmann, M., Su, T., Niu, B., Hou, Y., Alghamdi, M., Aldosary, M., ... & Shi, J. (2019). Probing magnetism in insulating Cr2Ge2Te6 by induced anomalous Hall effect in Pt. *Nano letters*, *19*(4), 2397-2403.

10. Su, T., Lohmann, M., Li, J., Xu, Y., Niu, B., Alghamdi, M., ... & Shi, J. (2020). Current-induced CrI3 surface spin-flop transition probed by proximity magnetoresistance in Pt. *2D Materials*, *7*(4), 045006.

11. Alghamdi, M., Lohmann, M., Li, J., Jothi, P. R., Shao, Q., Aldosary, M., ... & Shi, J. (2019). Highly efficient spin–orbit torque and switching of layered ferromagnet Fe3GeTe2. *Nano letters*, *19*(7), 4400-4405.

12. Jothi, P. R., Scheifers, J. P., Zhang, Y., Alghamdi, M., Stekovic, D., Itkis, M. E., ... & Fokwa, B. P. (2020). Fe5− xGe2Te2—a New Exfoliable Itinerant Ferromagnet with High

Curie Temperature and Large Perpendicular Magnetic Anisotropy. *physica status solidi (RRL)–Rapid Research Letters*, *14*(3), 1900666.

13. Zhang, X., Zhao, Y., Song, Q., Jia, S., Shi, J., & Han, W. (2016). Magnetic anisotropy of the single-crystalline ferromagnetic insulator Cr2Ge2Te6. *Japanese Journal of Applied Physics*, *55*(3), 033001.

14. Zhuo, W., Lei, B., Wu, S., Yu, F., Zhu, C., Cui, J., ... & Chen, X. (2021). Manipulating Ferromagnetism in Few-Layered Cr2Ge2Te6. *Advanced Materials*, *33*(31), 2008586.

15. Selter, S., Bastien, G., Wolter, A. U., Aswartham, S., & Büchner, B. (2020). Magnetic anisotropy and low-field magnetic phase diagram of the quasi-two-dimensional ferromagnet Cr 2 Ge 2 Te 6. *Physical Review B*, *101*(1), 014440.

16. Deiseroth, H. J., Aleksandrov, K., Reiner, C., Kienle, L., & Kremer, R. K. (2006). Fe3GeTe2 and Ni3GeTe2–Two New Layered Transition-Metal Compounds: Crystal Structures, HRTEM Investigations, and Magnetic and Electrical Properties.

17. Li, T., Jiang, S., Sivadas, N., Wang, Z., Xu, Y., Weber, D., ... & Shan, J. (2019). Pressure-controlled interlayer magnetism in atomically thin CrI3. *Nature materials*, *18*(12), 1303-1308.

18. Jiang, S., Li, L., Wang, Z., Mak, K. F., & Shan, J. (2018). Controlling magnetism in 2D CrI3 by electrostatic doping. *Nature nanotechnology*, *13*(7), 549-553.

19. Thomson, W. (1857). XIX. On the electro-dynamic qualities of metals:—Effects of magnetization on the electric conductivity of nickel and of iron. *Proceedings of the Royal Society of London*, (8), 546-550.

20. McGuire, T., & Potter, R. L. (1975). Anisotropic magnetoresistance in ferromagnetic 3d alloys. *IEEE Transactions on Magnetics*, *11*(4), 1018-1038.

21. Ali, M. N., Xiong, J., Flynn, S., Tao, J., Gibson, Q. D., Schoop, L. M., ... & Cava, R. J. (2014). Large, non-saturating magnetoresistance in WTe2. *Nature*, *514*(7521), 205-208.

22. Hall, E. H. (1879). On a new action of the magnet on electric currents. *American Journal of Mathematics*, *2*(3), 287-292.

23. Nagaosa, N., Sinova, J., Onoda, S., MacDonald, A. H., & Ong, N. P. (2010). Anomalous hall effect. *Reviews of modern physics*, *82*(2), 1539.

24. Tong, D. (2016). The Quantum Hall Effect. TIFR Infosys Lectures. *arXiv preprint arXiv:1606.06687*.

25. Garello, K., Miron, I. M., Avci, C. O., Freimuth, F., Mokrousov, Y., Blügel, S., ... & Gambardella, P. (2013). Symmetry and magnitude of spin–orbit torques in ferromagnetic heterostructures. *Nature nanotechnology*, *8*(8), 587-593.

26. Avci, C. O., Garello, K., Gabureac, M., Ghosh, A., Fuhrer, A., Alvarado, S. F., & Gambardella, P. (2014). Interplay of spin-orbit torque and thermoelectric effects in ferromagnet/normal-metal bilayers. *Physical Review B*, *90*(22), 224427.

27. Li, J., Yu, G., Tang, C., Liu, Y., Shi, Z., Liu, Y., ... & Shi, J. (2017). Deficiency of the bulk spin Hall effect model for spin-orbit torques in magnetic-insulator/heavy-metal heterostructures. *Physical Review B*, *95*(24), 241305.

28. Pai, C. F., Mann, M., Tan, A. J., & Beach, G. S. (2016). Determination of spin torque efficiencies in heterostructures with perpendicular magnetic anisotropy. *Physical Review B*, *93*(14), 144409.

Chapter 2   Device fabrication of van der Waals ferromagnets: FGT and FG2T

2.1 Device fabrication and protection

Device fabrication of vdW ferromagnet is relatively straightforward. The fabrication processes start by exfoliating the flakes on Si/SiO_2 wafer. 2 layers of 200 nm of PMMA e-beam resist are spin-coated on the wafer. Electron beam lithography (EBL) performed after designing the desired electrodes on the chosen flake. Pt (70nm)/Cr (5nm) deposited using the AJA sputtering system at a base pressure 5×10^{-8} torr. Optional cleaning of the contact areas before the deposition. This optional step is to enhance electrical contact to achieve very low contact resistance. ICP etcher can also be used to do the cleaning (we did that at first device fabrication stages because there is a handling time). The low contact resistance is very important in studying the intrinsic material properties. Low thickness devices were protected by depositing a Al_2O_3 film of a thickness between 20 to 100 nm using AJA sputtering system. Some devices are protected by using h-BN flakes transferred into FGT flakes. This thin film of Al_2O_3 or h-BN flakes are adequate to protect the flake from degradation. **Fig. 2.1** shows a fabrication process of a FGT flake with the optional protection step. **Fig. 2.3** shows some of the fabrication steps of BN/FGT heterostructure devices.

For Al_2O_3 film deposition, the flake is exposed to air for a short period (after exfoliation and lifting off before deposition). Even if this exposure time is minimized, this time is still a long period of time for oxidation to take place according to the mean free path theory. **Fig. 2.2** shows devices protected with 20 nm of Al_2O_3 film and with 2D h-BN flake. The beauty of using sufficiently large h-BN flakes as a protection layer is that we

can minimize the air exposure time to zero. h-BN/FGT heterostructure can be fabricated inside a glove box. The large h-BN flake not only covers the FGT top surface but also seals the flake on all sides. This way the device is fully protected against damages or creating a rough surface by sputtering. These two ways of protection are effective to protect the flake from degradation.
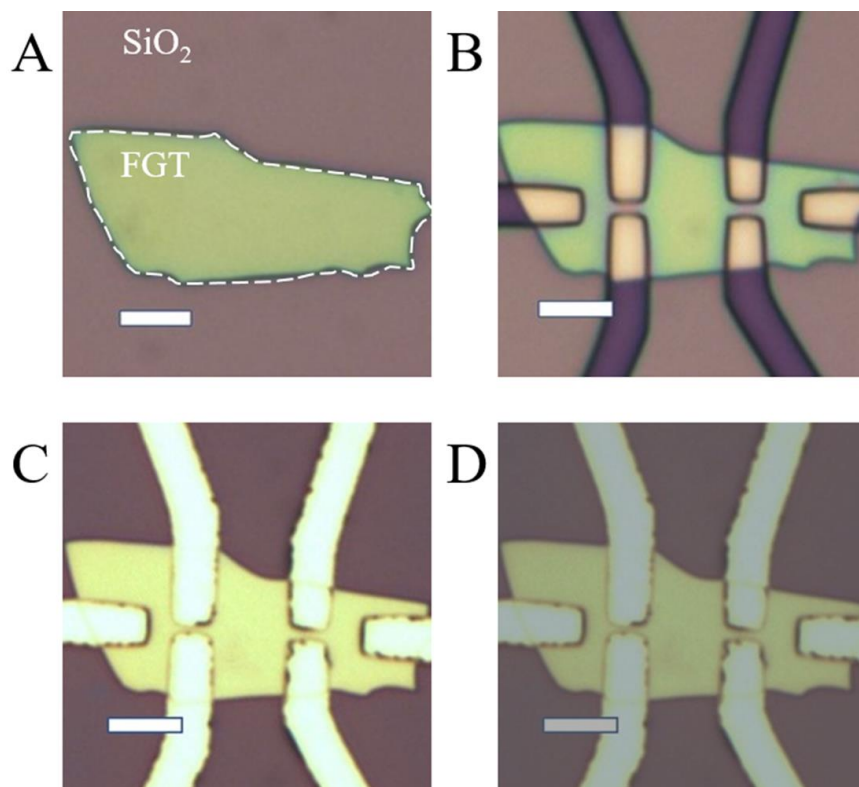
Fig. 2.1. Fabrication Steps of FGT Flakes. 53L FG2T microscope picture is shown and the scale bar is 5 um. (A) Chosen flake picture after exfoliation. (B) The same flake after electrode definition using EBL. (C) The device after electrode deposition. (D) Optional post-fabrication step of depositing Al_2O_3 thin film for protection.
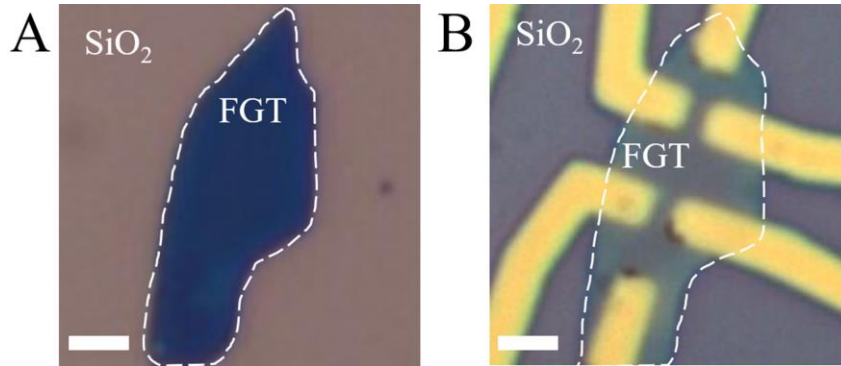
Fig. 2.2. 3L FGT Protected Devices Microscope Pictures. The dash white line showing the SiO_2 and 3L FGT in the microscope picture and the scale bar is 2 um. (A) shows 3L FGT flake in SiO_2 wafer before performing the electrodes. (B) shows the final device picture after depositing 20nm of Al_2O_3.
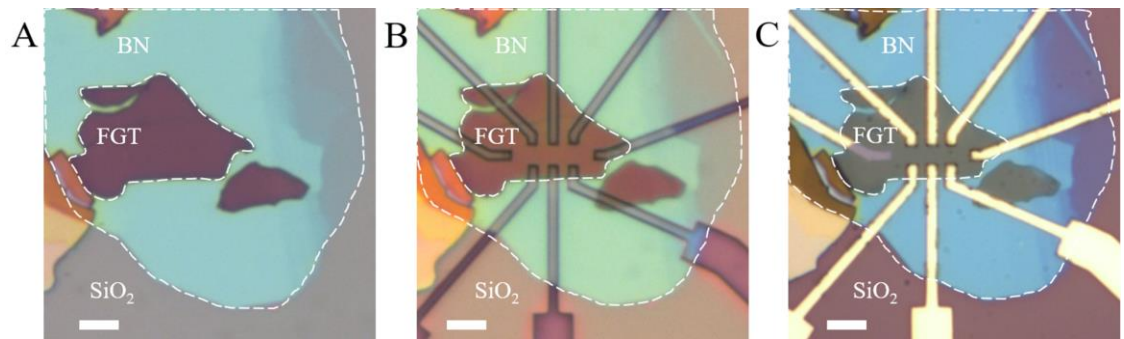
Fig. 2.3. Fabrication Steps for h-BN/FGT Heterostructure. The white dash line shows the FGT, BN, and SiO2. The scale bar is 3um. (A) h-BN/FGT heterostructure picture after h-BN transfer. (B) The heterostructure after performing EBL. (C) The final device photo of the same heterostructure after electrode deposition.

To investigate the effect of degradation, **Fig. 2.4** shows the longitudinal resistance as a function of temperature with the same applied current for the protected device. Notice that the protected device held its longitudinal resistance over more than 6 months, which is strong evidence that the material properties remain unchanged. **Fig. 2.5** shows the longitudinal resistance of unprotect devices that slowly changes over time. We can estimate it loses a layer every 2-3 week and it is clear that the flake surface becomes rougher over time.
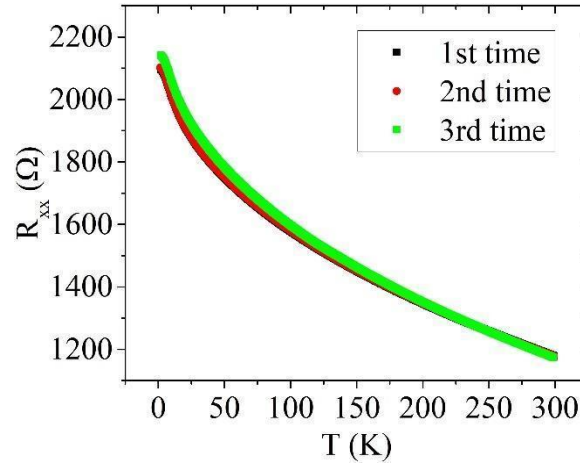
Fig. 2.4. Temperature Dependence of Longitudinal Resistance of 1L FG2T. shows LR of the protected device of 1L FG2T. The 1st time is measured a few days after fabrication. The 2nd time is the same device measured 2 months later. The 3rd time is measured 5 months after fabrication.
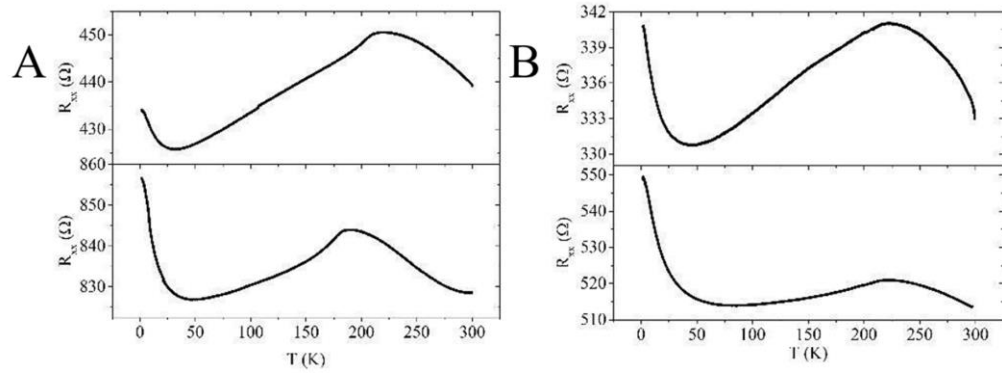
Fig. 2.5. Temperature Dependence of Longitudinal Resistance of 5L and 12L. LR as a function of temperature of the unprotect devices of 12L (A) and 5L (B) of FG2T. Upper shows the measurements a few days after fabrication, and the lower shows 6 months after fabrication.

2.2 Heterostructure Fabrication

The transfer microscope can be used to build a heterostructure. It consists of two stages to manipulate the flake position namely bottom and top stages. The bottom stage has a feature of space movements (X, Y, Z) direction plus a rotation (R) of the flake. The top stage also has a space movement (X, Y, Z) plus a tilt axis (T). PPC is used to pick up

18

the 2D h-BN flake from the Si wafer after heating up to 45 C^o and cooldown to 25 C^o. Then dropped on the FGT flake at 110C^o. The picture of the transfer microscope is shown in **Fig. 2.6** outside and inside the glovebox. **Fig. 2.7** shows the building of the heterostructure using the transfer microscope. In order to build h-BN/FGT heterostructure we first exfoliate h-BN flakes into SiO_2 wafer and the wafer placed in the bottom stage. Then in a glass slide the PDMS stamp is attached followed by spin coat the PPC at 2000 rpm for 40 sec. The glass slide then baked at 180 C^o for 10 minutes in order to get good adhesive to the PDMS stamp. The result is a clear thin polymer used to pick up the BN later. The glass slide is mounted in the top stage in the transfer microscope and uses the objective lens to locate the BN flake by the coordinate manipulators. The PPC film was brought to contact then the heater set 40 C^o to soften the PPC film. The glass transition in PPS flattens and cover the whale flake. The heater turned off to cold down to reach 25 C^o. After that BN flake picked up using the Z manipulator in the top stage. PPC contrasts over the BN and holds force on the BN surface. The SiO_2 wafer with other BN flakes then removed and replaced with another SiO_2 that has a freshly exfoliated FGT. The top stage was manipulated with the help of the objective lens then used to drop the BN flake. Again, the glass slide brought contact and the heater set at 110 C^o. This temperature is enough to drop the PPS film that has BN. Now the BN/FGT Heterostructure built after cleaning the PPC film with acetone and the Heterostructure is ready for a further fabrication.
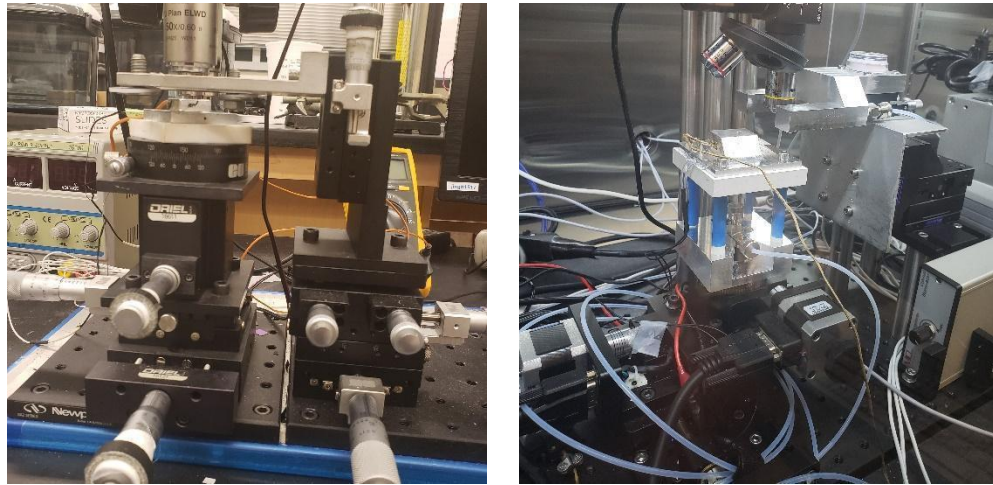
Fig. 2.6 Transfer Microscope Picture. The transfer microscope picture (Left). The glovebox transfer microscope (Right).
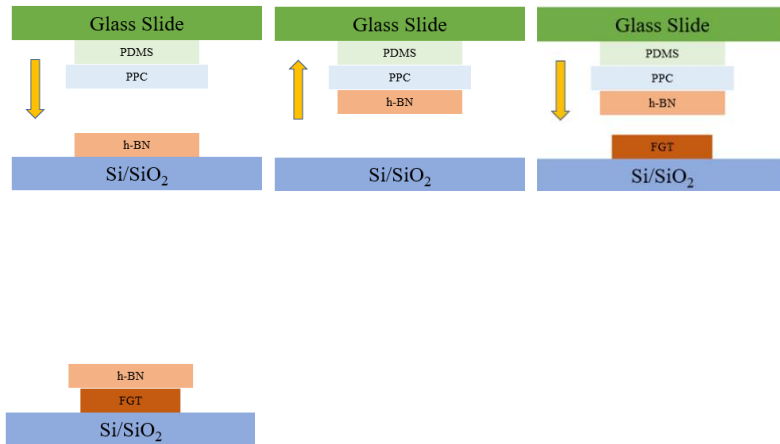
Fig. 2.7. Fabrication Steps for h-BN/FGT Heterostructure. There are 4 steps to fabricating the h-BN/FGT heterostructure. Starting from the left, the PPC thin film brought to contact and then pick up the h-BN flake. The h-BN flake then dropped into a fresh exfoliated FGT. The final h-BN/FGT heterostructure clean with acetone to remove any organic residue from the PPC.

2.3 Electrical transport measurements

The transport measurements for the FGT devices are performed in the Physical Properties Measurement System by Quantum Design over a temperature range of 300 to

1.6 K. Some of the devices were measured in a 4K closed cycle system. Lakeshore 332 and Lakeshore 425 were used to control and measure the temperature. For DC measurements, we kept a fixed current in the flake with a Keithley 2400 source meter which also monitors the two-terminal resistance. To measure the longitudinal and Hall resistances, Keithley 2182A nanovoltmeter and Keithley 2000 multimeter were used.

Chapter 3

Layer dependence of Kondo temperature and linear magnetoresistance of 2D Ferromagnets: $Fe_5Ge_2Te_2$ and Fe_3GeTe_2

3.1 Background and Motivation

The presence of local magnetic moments in a metal host leads to scattering of conduction electrons by them. The local moment is screened by the free electrons, which form a spin Kondo singlet. The result is a change in the electrical resistivity to cause a minimum at low temperatures. A great physicist, Jun Kondo, first theoretically explained the new phenomenon in alloys at low temperatures which was named the Kondo effect in 1965.[1] Many other theorists and experimentalists contributed to the explanation of this phenomenon.[2,3] Since the Kondo effect was first discovered in crystalline and amorphous metal films, this phenomenon was recently revisited in the 2D materials (VSe_2, VTe_2, and Fe_3GeTe_2 etc.)[4-7] In an angle-resolved photoemission spectroscopy (ARPES) study[4], heavy Fermion states with the Kondo lattice were observed in FGT. Fe-vacancies in FGT were also explained with Kondo screening. The existence of the resistivity minimum at low temperatures was displayed in some papers but it has not been explained by the Kondo effect.[8-12]

The existence of magnetic vacancies and Fe-impurities cause changes in Curie temperature (T_c), magnetic anisotropy, and magnetization in FGT. These also have a direct impact on the electrical resistance. The vacancies introduce an interaction between local defect states and the free electrons. This interaction atomically changes the magnetic interactions. Kondo screening may vary in the vacancies. While Fe free atoms scattered in the FGT lattice went in Kondo behavior because of the appearance of singlet state Kondo.[5]

The electrical resistance in the present or absence of the magnetic field probe of these vacancies and impurities. We choose 2 different metallic layered ferromagnets FGT and FG2T with different T_c, anisotropy fields and longitudinal resistivities to study the effect of Kondo.[13-16]

3.2 Introduction

Recently, we found a minimum in the LR as a function of temperature before it increases and saturates at low temperatures in some FGT devices. The low-temperature diverging feature in resistivity may be caused by weak localization (WL), variable-range hopping (VRH), or/and Kondo effects (KE). WL is basically due to quantum interference between the two time-reversal paths and causes a logarithmic temperature dependence, while VRH gives rise to an exponential temperature dependence. Both mechanisms cannot explain the low-temperature saturation behavior observed in FGT. However, KE not only explains the resistivity minimum and low-temperature divergence, but also the saturation behavior. The best way to describe FGT and FG2T low-temperature resistivity behavior in the ferromagnetic phase is to include 4 different terms shown in Eq. 3.1. The first one is the residue resistance R_o at zero temperature due to impurities and defects. The second is $\sim T^2$ that comes from both electron-magnon interaction and electron-electron interaction. The third is $\sim T$ that comes from electron-phonon interaction. The fourth term is the Kondo part that comes from magnetic impurities and defects.[6-7,17-18] This part is responsible for the insulating behavior at low temperatures.

$$R_{xx} = R_o + qT^2 + pT + R_{ko}\left(\frac{T`^2_k}{T^2+T`^2_k}\right)^S$$

(3.1)

Were $T`_k = \dfrac{T_k}{\left(2^{\frac{1}{0.225}}-1\right)^{\frac{1}{2}}}$ and $T_k = 4.5\,T`_k$. The above combination represents the

metallic temperature dependence and insulating temperature dependence at low

temperatures.

In this work we chose flakes with different thickness and fabricated electrodes to

measure the 4-terminal longitudinal resistance at zero magnetic field. We fit equation 3.1

that includes the Kondo effect in the LR of different FGT and FG2T flakes at a relatively

low fixed current density of $\sim 5\times10^8$ A/m^2. We have chosen this relatively low current

density to minimize the effect of heating to ensure the accurate temperature readings

because the Joule heating affects the low temperature data more significantly. We

performed our fitting study at the low temperature ferromagnetic conductive phase of FGT.

Also, we performed the magnetoresistance measurements at high out-of-plane fields for

different layer numbers.

3.3 Longitudinal Resistance at H=0

Figs. 3.1 and **3.2** show the temperature dependence of LR of different layer

numbers of FGT and FG2T flakes on a semi-log scale for the temperature axis. The red

line is the best fit using equation 3.1 with fitting parameters (see 3.8.1), namely, the Kondo

temperature, the residue resistance at zero temperature, and the conductive contribution constants, p and q. Most sample`s temperature dependence of LR curves were fitted in the low temperature range below 100K. At low thicknesses (i.e., 1L and 3L for FG2T and 3L for FGT), the resistance starts to show an insulating behavior over the entire temperature range including the ferromagnetic and paramagnetic phases. This insulating behavior may be due to the intrinsic or extrinsic effect. For the intrinsic one, it may be caused by a stronger correlation effect in thinner samples. For the extrinsic effect, it may be due to surface layer modification caused by oxidation or off stoichiometry which becomes more pronounced for small thicknesses or larger surface/bulk ratios. To distinguish these two effects, more experiments are needed. One control sample would be thin flake samples covered by a BN layer inside the glovebox so that the surface is well protected against exposure to air or other organic substances during the lithography processes. For thicker FG2T and FGT samples, they show metallic resistivity below T_c, but resistivity shows a minimum at low temperatures. This minimum resistivity and low-temperature saturation agree with the Kondo effect, which is repeated in a different FGT sister material ($Fe_{2.78}GeTe_2$). Chen B. tried to fit ~T^2 the longitudinal resistivity and did not explain the low temperature increase because of the missing Kondo term.[19]
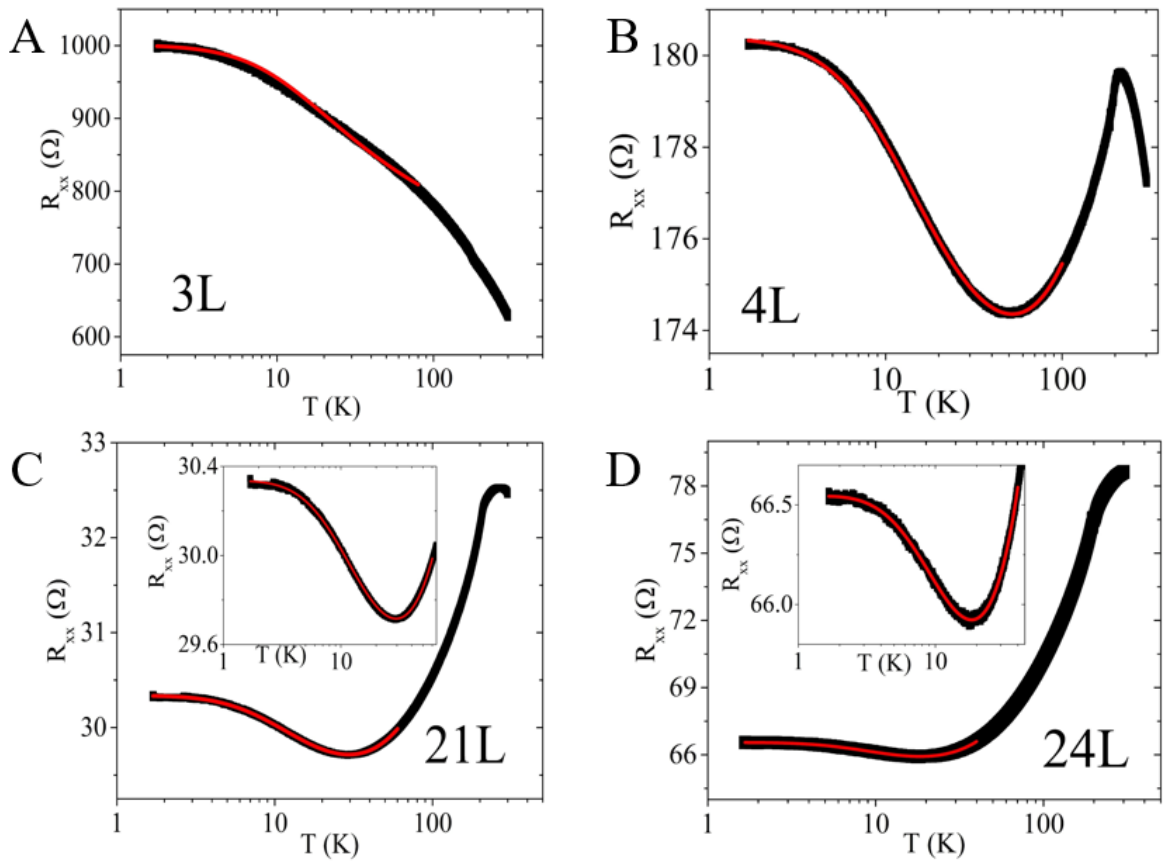
Fig. 3.1 Temperature Dependence of LR of FGT. Longitudinal resistance as a function of temperature in log scale for (A) 3L, (B) 4L, (C) 21L, (D) 24L. The response of the longitudinal resistance varies from the different thickness.
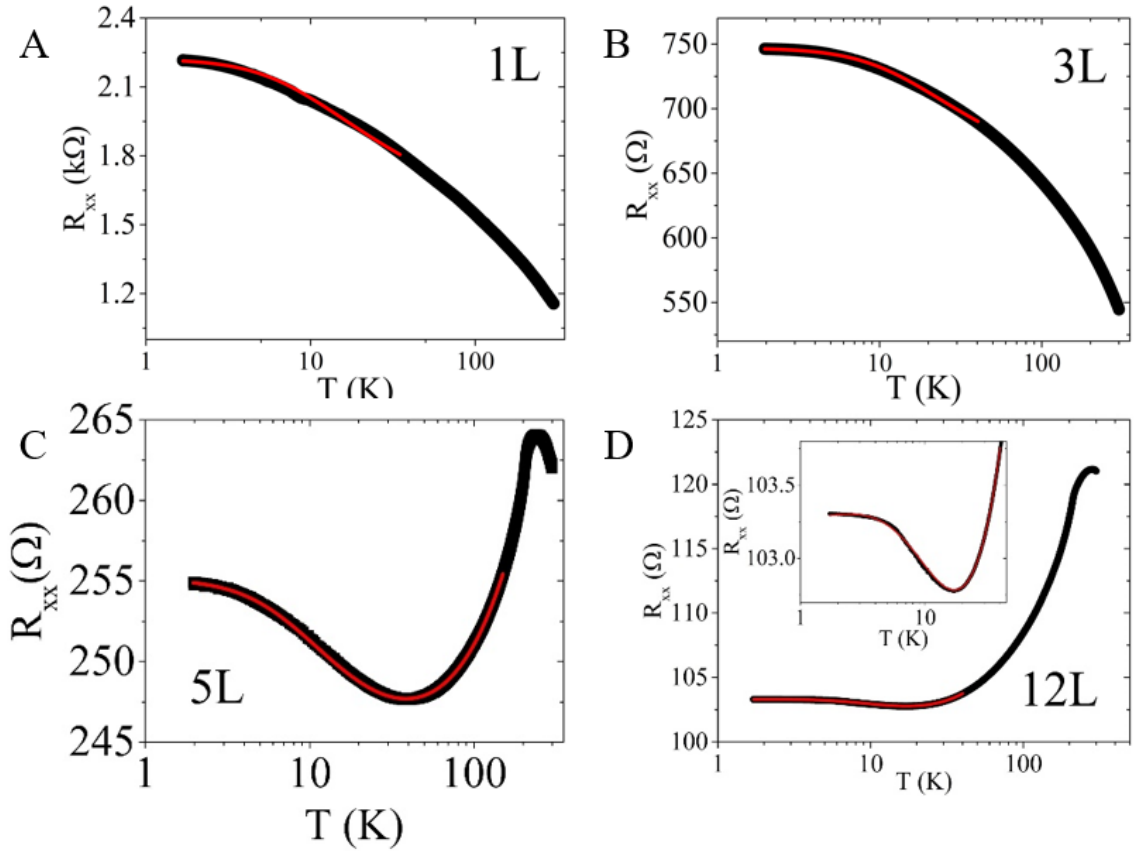
Fig. 3.2 Temperature Dependence of LR of FG2T. Longitudinal resistance as a function of temperature in log scale for (A) 1L, (B) 3L, (C) 4L, (D) 12L. The response of the longitudinal resistance varies from the different thickness.

3.4 Kondo Temperature

The Kondo temperature T_k can be extracted from the fitting using equation (3.1). We plot T_k as a function of layer number for FG2T and FGT in **Fig. 3.3**. We notice that T_k approaches a nearly constant temperature of 34 K at large layer numbers, while at small layer numbers it has a rapid increasing trend as the layer number decreases. Below ~10 layers, the Kondo temperature shows a strong layer dependence as the system approaches the 2D limit. One possibility is that a stronger exchange interaction occurs to form Kondo singlet in a few layers' material. The detailed mechanism behind this is still unknown. A

caveat about the rapid rise in T_k is that the fitting using equation 3.1 only works for metallic behavior. For thin samples, the overall temperature dependence turns insulating; therefore, fitting artificially inflates T_k. Barua S. et. al. observed a minimum in LR the 2D VSe_2 and they extracted the Kondo temperature.[6] Liu, H. et al. used the same equation to fit LR of the 2D ferromagnet VTe_2 and replace the term ~T with ~T^5.[7] Providing the Kondo temperature over such a large range of layer numbers down to monolayer reveals a robust Kondo screening picture for FGT and FG2T.[6,7]
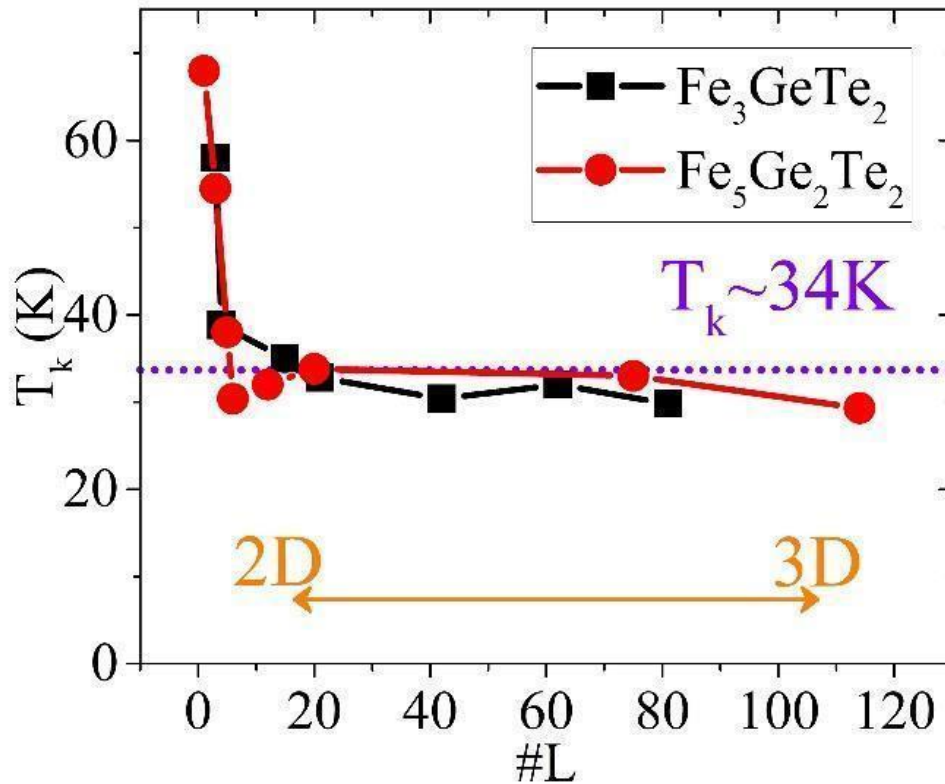
Fig. 3.3 Layer Dependence of Kondo Temperature. T_k as a function of the number of layers of FGT and FG2T using equation (3.1). The low thickness usage of the conductive terms of equation (3.1) invalid due to the insulator behavior in the conductive region exit.

3.5 Temperature Dependent of Magnetoresistance

Fig. 3.4. shows MR at different temperatures for 42L FGT flake. This linear MR response exists over the ferromagnetic state of FGT while it is not linear near the Curie temperature. It is about -1.75% at 2K to -0.29% at 200K. The linear MR is common in thick FGT and FG2T down to 4L as can been seen in **Fig. 3.6**. Liu. P., et al. shows a linear MR up to 8 Tesla for FGT flakes with near to previously reported Tc.[20] While Ke. J. et al. show a nonlinear MR with low Tc near a monolayer FGT of 138K of relatively thick metallic flakes.[21] The nonlinear MR below 3L is unusual and it needs a further investigation. Monolayer FG2T has a new feature, and it shows a positive MR as can be seen in **Fig. 3.5**. At 2 K the percentage of change in MR resistance for the value at zero applied out-of-plane field is +0.45%. It decreases until about 4 Tesla then it increases. At 20 K it is saturated with -0.55% negative MR. Then at room temperatures where it has a parabolic MR in the paramagnetic state of FGT of -0.1%. The transition temperature from positive MR to negative MR is about ~20 K. This positive MR will be considered for a further investigation.
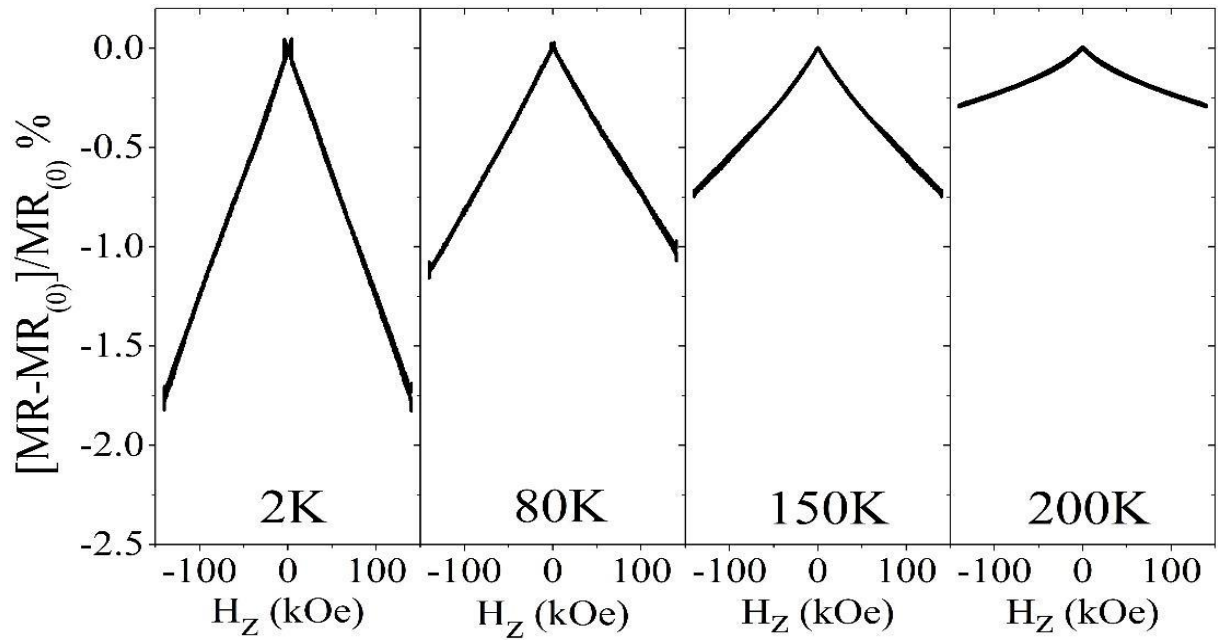
Fig. 3.4 Temperature dependence of Magnetoresistance of 42L FGT.
Shows the percentage of change of the MR of 42L FGT and it decreases
by increasing the temperature from 2K to 200k.
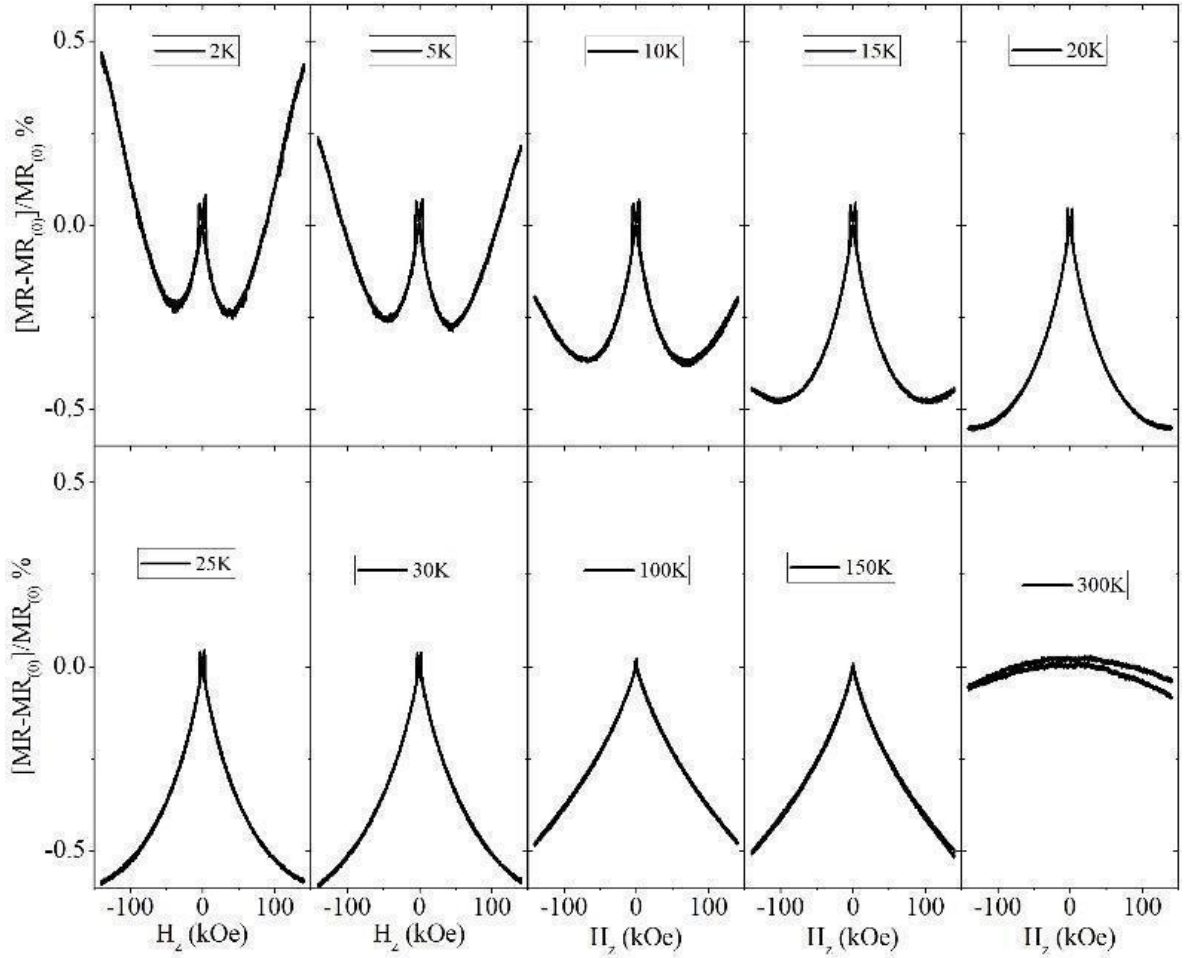
Fig. 3.5 Field Dependence of Magnetoresistance of 1L FG2T. MR is applied out of plane at different temperatures for monolayer FG2T devices.

3.6 Layered Dependance of Magnetoresistance

Fig. 3.6 shows the percentage of change in MR from its value at zero magnetic field as a function of applied out-of-plane fields for FG2T and FGT at 2K. For thickness > 3 L, the MR shows linear field dependence. This linear dependence of negative MR at high out-of-plane fields is surprising and rarely seen in other systems. Moreover, we also measured MR with the magnetic field parallel to the atomic planes. We found that the negative MR is not very sensitive to the direction of the magnetic field which is in direct contrast with

the highly anisotropic behavior for the weak localization. In the 1L FG2T sample, there is

a positive high-field MR superimposed on a negative low-field MR. On the other hand, the

high-field linear MR indicates that not all moments are saturated at 14 T and even higher

fields are needed to align the moments. At this point, it is not known what these unsaturated

magnetic moments are in FGT and FG2T lattices. The percentage of the change in MR is

approximately from -1.4% to -2.1% at 14 T for both FGT and FG2T, almost independent

of layer numbers, except for the 1L to 3L samples. It suggests that the negative MR is an

intrinsic property of the pristine materials. It keeps linear down to 4L of FGT but for 3L

and below it is not linear, and it may be due to a weak anisotropy field. The change of MR

of 3L of FGT is -0.9% and the 1L FG2T is showing a positive MR with a percentage of

change of +0.4%. At this point, the physical mechanism behind both negative and positive

MR in FGT and FG2T are not understood.
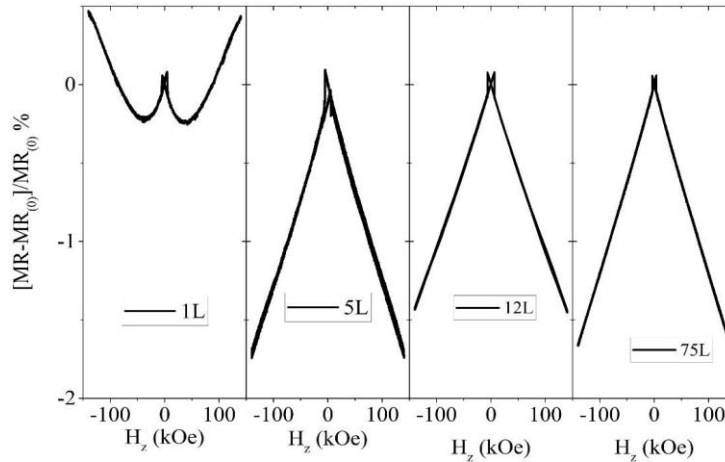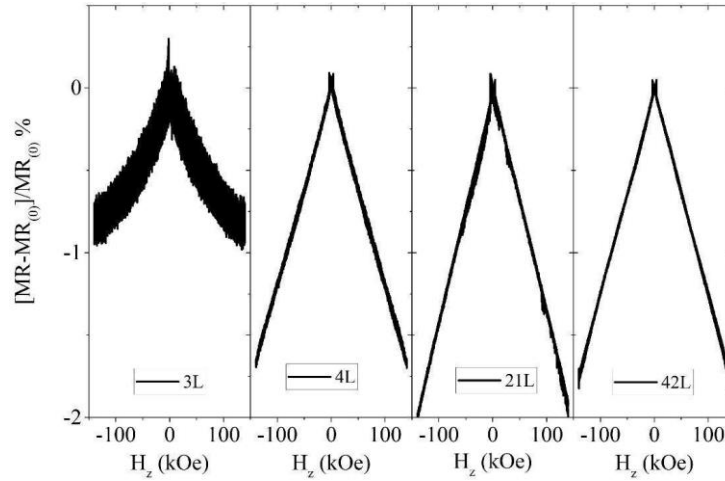
Fig. 3.6 Thickness Dependence of Magnetoresistance. MR of FG2T
(A) and FGT (B) as a function of applied out-of-plane magnetic field.

3.7 Summary

We describe the low temperature resistance minimum and explain it by the Kondo

effect in FGT and FG2T from the LR. Kondo temperature increases rapidly for thickness

below 6L. The MR has a linear response over a large range of magnetic fields up 14 T. The

linear negative MR in FGT and FG2T is independent of the magnetic field direction. The

low-temperature insulating behavior in LR and the negative MR in FGT and FG2T may be

both due to the Kondo effect related to the scattering for free electrons from s-d interaction.

3.8 Discussion

3.8.1 Extraction of the Kondo Temperatures

We used Eq 3.1 to extract the Kondo temperature. In that equation, the ~T and ~T^2

terms fit in the range below Curie temperature down to a little before reaching the minimum

while the fourth term is the insulating part arising from the Kondo effect. Combining the

2nd, 3rd, and the 4th terms generates a minimum. **Fig. 3.8 (A)** shows a reasonable fit LR

of 1L FG2T from 1.6 K up to 100 K. After using equation 3.1 to extract the parameters we find the Kondo temperature of 52 K and the ~T and ~T^2 goes to zero due to the existence of insulating behavior. If we look closely at the curve and the fitted line, we can tell that it somehow saturates at low temperatures but the minimum of the curve, if there is any, may be around 500 K, which is obviously not compatible with the Kondo theory that was formulated for low-temperature phenomena. Fig. 3.7 (A) shows LR of the 3L FGT and the red fitted line using equation 3.1. We find the Kondo temperature of 45K, and the coefficient of p and q goes to zero. **Fig. 3.8 (B)** on the other hand, shows LR of the 3L FG2T and the red fitted line using equation 3.1. We find the Kondo temperature of 54 K, higher than that for monolayer FG2T. Now, let us look at **Figs. 3.7 (B), (C), and (D) and 3.8 (C), and (D),** that show a collection of temperature dependence LR curves with fitting curves using equation 3.1. If we begin with **Fig. 3.8 (C) and (D)** that show LR curves of 5 L and 12 L of FG2T, the Kondo constant R_{ko} value is small compared to the residual resistance at zero temperature. And R_{ko} is also small in value compared to its value at room temperature is small for a thick 12 L FG2T. It increases as the thickness decreases to 5 L. This increase of Kondo constant due to the screening strength. The 12 L thick flake shows less screening while in 5 L FG2T flakes the screening strength increase. The strength of the screening is due to the high interaction between a few layers. The electron-electron interaction can be examined by focusing on parameter p, i.e., the coefficient of the ~T term. We notice from the fitting that p increases by reducing the layer number and this increase suggests strong electron-electron interaction in thinner samples (this is still the fact based on observation) the homogeneous distribution of the electron path in the material and high

sensitivity of the screening. While if we closely look at electron-photon interaction, it is finite in 12 L thick FG2T but vanishes below 6 L. This indicates that only electron-electron interaction is dominant in the thin samples.

Figs. 3.7 (B), (C), and (D) show temperature dependence of LR with a fitting of equation 3.1. Similar behaviors exist if we compare FGT to FG2T. In the thin flake limit, the metallic resistivity background is dominated by electron-electron interaction, which is common to FG2T. This indicates that although FGT and FG2T are different in Curie temperature and anisotropy energy, they share common physical behaviors.
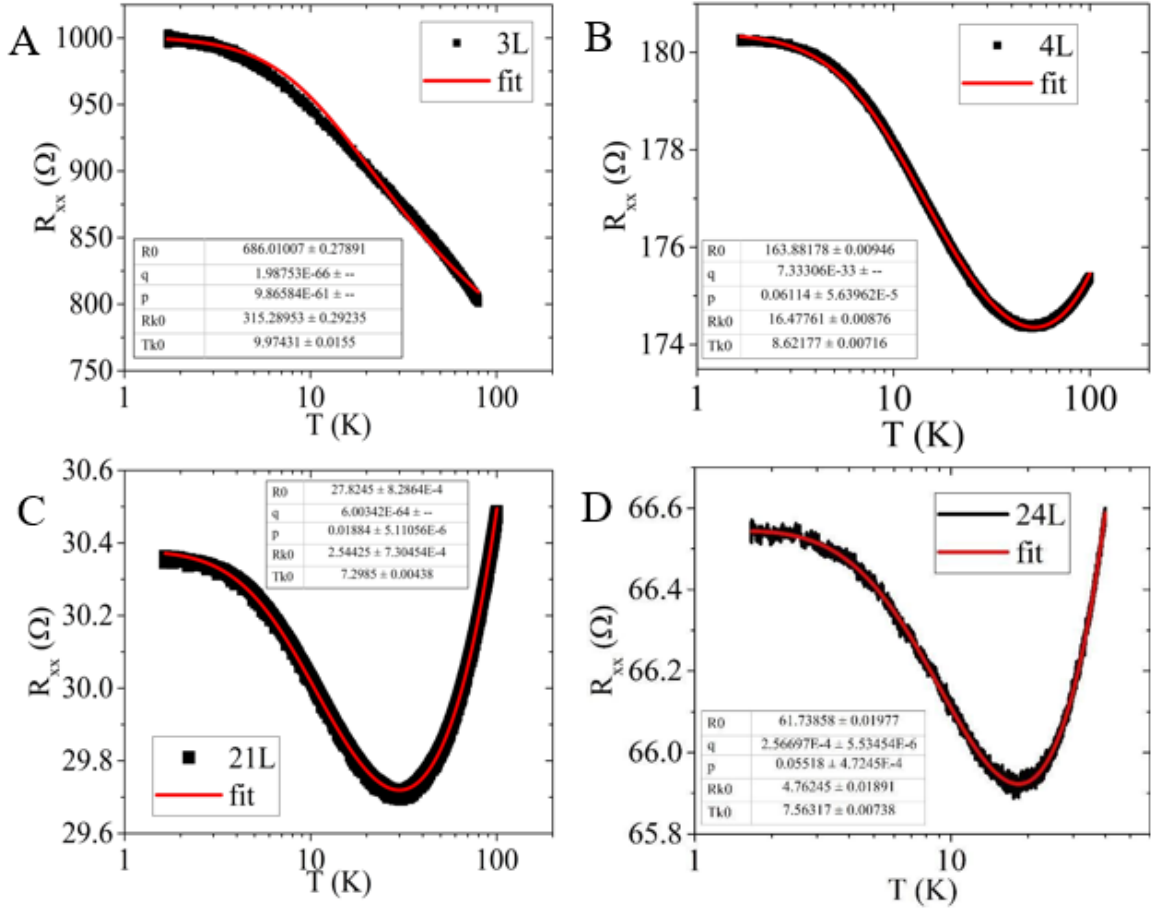
Fig. 3.7. Fitted Temperature dependence of LR of FGT. Shows LR of FGT for (A) 3L, (B) 4L, (C) 21L, (D) 24L. The variation for the LR

is different of different thickness and the inset shows the table of the fitted parameters of eq 3.1.
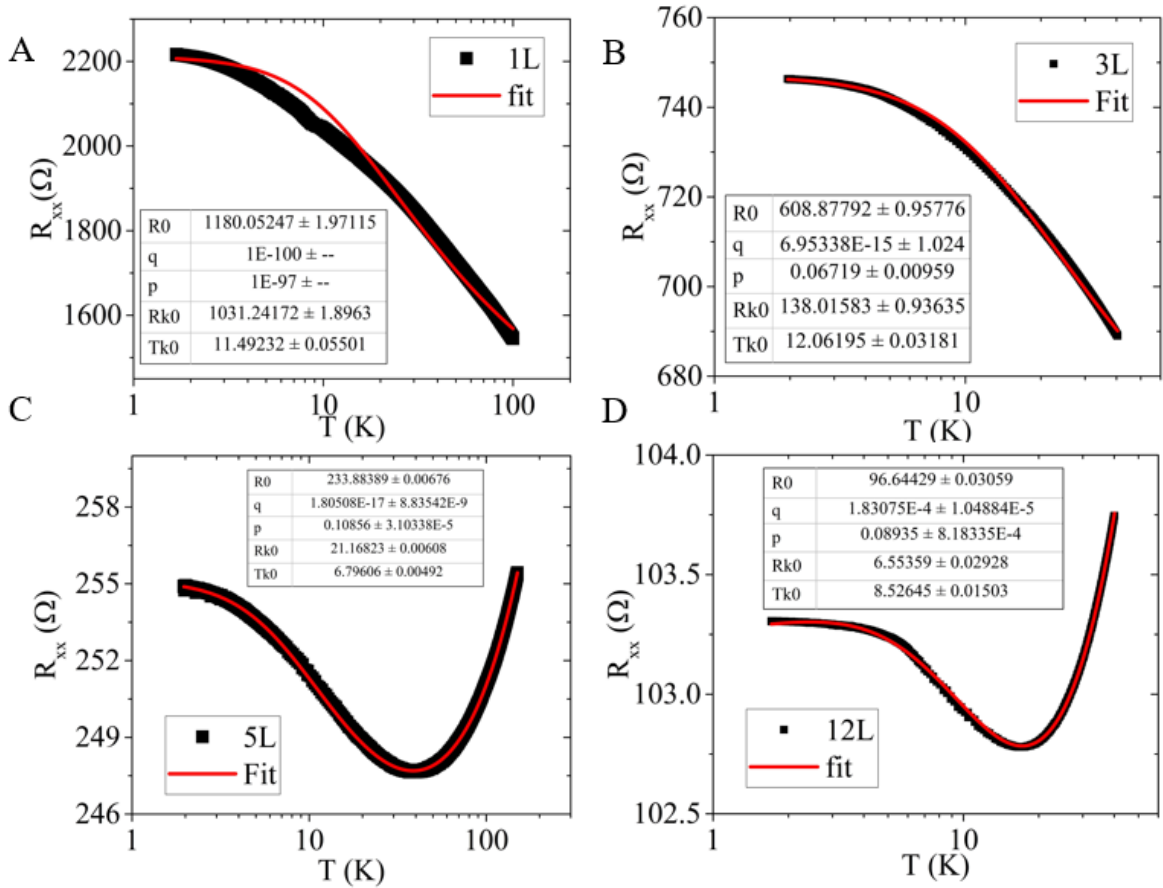
Fig. 3.8. Fitted Temperature dependence of LR of FG2T. Shows LR of FG2T for (A) 1L, (B) 3L, (C) 5L, (D) 12L. The variation for the LR is different of different thickness and the inset shows the table of the fitted parameters of eq 3.1.
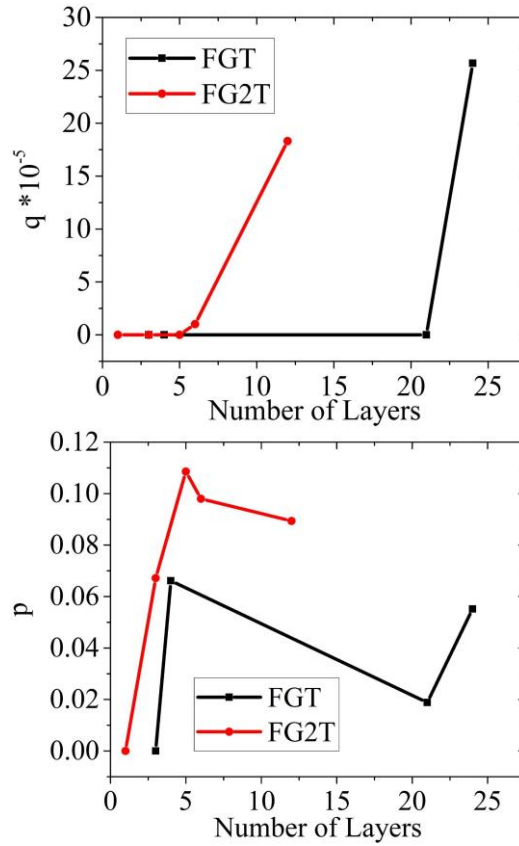
Fig. 3.9 Layer dependence of q and p Constant. The left figure shows q constant as a function of the number of layers. The low thickness shows almost zero value and starts to increase by increasing the layer number. The right figure shows the p constant which also almost has a zero value at thinner flakes and a reasonable value for higher thicknesses.

3.8.2 IV curves of the insulating FG2T

Figs 3.10 and 3.11 shows a linear IV curve of 1L and 3L FG2T at different temperatures. Over the wide temperature range from paramagnetic state to ferromagnetic state, the IV response is linear due to a nature of semi metallic behavior in FG2T, even at low temperatures where insulating behavior takes place. This nature in 2D ferromagnet is interesting and may reveal a new opportunity in fabrication of heterostructure. We will leave this insulator low thickness behavior for a further investigation.
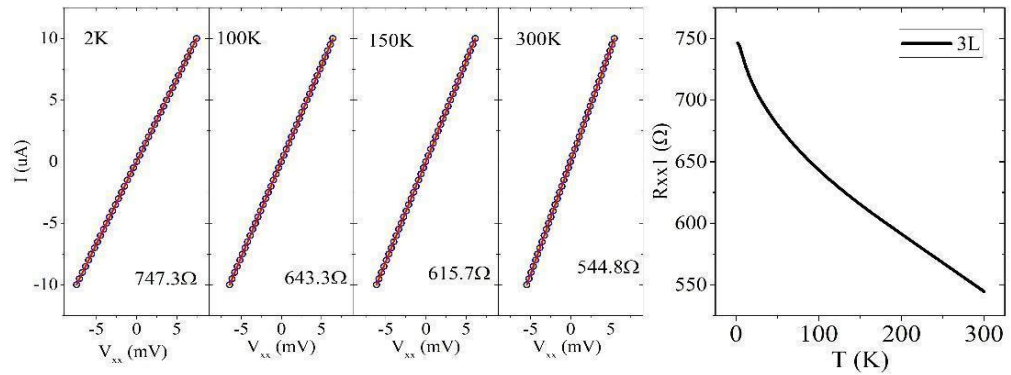
Fig. 3.10. Temperature Dependence of LR and IV of 3L FG2T. Longitudinal resistance as a function of T that shows the insulator behavior of 3L FG2T. The linear IV curve at different temperatures is shown.
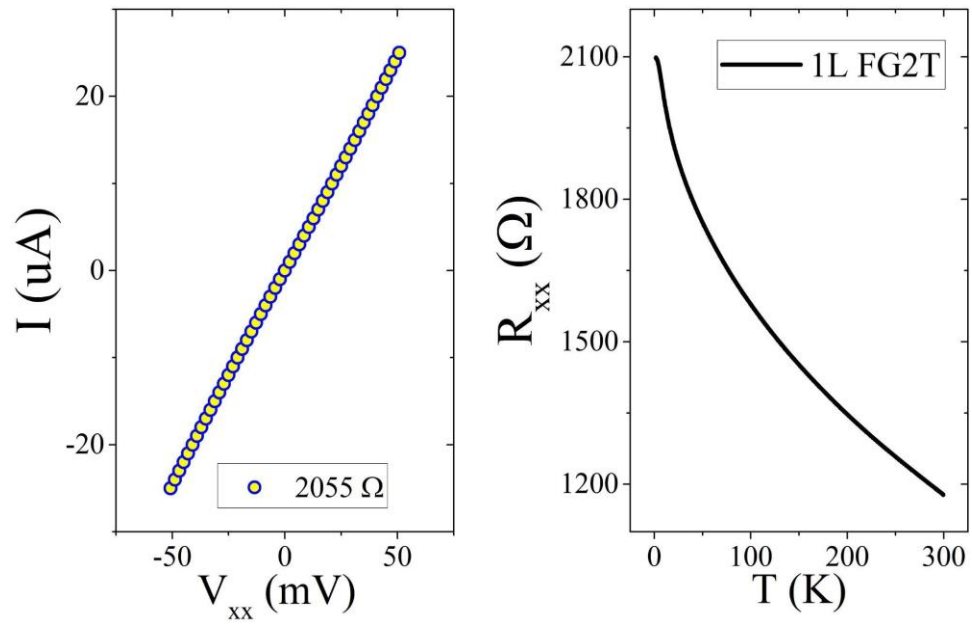
Fig. 3.11. Temperature Dependence of LR and IV of 1L FG2T. Longitudinal resistance as a function of T that shows the insulator behavior of 1L FG2T. The linear IV curve at 2K temperatures is shown.

References

1. Kondo, J. (1964). Resistance minimum in dilute magnetic alloys. *Progress of theoretical physics*, *32*(1), 37-49.

2. Nagaoka, Y. (1965). Self-consistent treatment of Kondo's effect in dilute alloys. *Physical Review*, *138*(4A), A1112.

3. Daybell, M. D., & Steyert, W. A. (1968). Localized magnetic impurity states in metals: Some experimental relationships. *Reviews of Modern Physics*, *40*(2), 380.

4. Zhang, Y., Lu, H., Zhu, X., Tan, S., Feng, W., Liu, Q., ... & Lai, X. (2018). Emergence of Kondo lattice behavior in a van der Waals itinerant ferromagnet, Fe3GeTe2. *Science advances*, *4*(1), eaao6791.

5. Zhao, M., Chen, B. B., Xi, Y., Zhao, Y., Xu, H., Zhang, H., ... & Du, Y. (2021). Kondo holes in the two-dimensional itinerant Ising ferromagnet Fe3GeTe2. *Nano Letters*, *21*(14), 6117-6123.

6. Barua, S., Hatnean, M. C., Lees, M. R., & Balakrishnan, G. (2017). Signatures of the Kondo effect in VSe2. *Scientific reports*, *7*(1), 1-10.

7. Liu, H., Xue, Y., Shi, J. A., Guzman, R. A., Zhang, P., Zhou, Z., ... & Gao, H. J. (2019). Observation of the kondo effect in multilayer single-crystalline VTe2 nanoplates. *Nano Letters*, *19*(12), 8572-8580.

8. Deng, Y., Yu, Y., Song, Y., Zhang, J., Wang, N. Z., Sun, Z., ... & Zhang, Y. (2018). Gate-tunable room-temperature ferromagnetism in two-dimensional Fe3GeTe2. *Nature*, *563*(7729), 94-99.

9. Tan, C., Lee, J., Jung, S. G., Park, T., Albarakati, S., Partridge, J., ... & Lee, C. (2018). Hard magnetic properties in nanoflake van der Waals Fe3GeTe2. *Nature communications*, *9*(1), 1-7.

10. Fei, Z., Huang, B., Malinowski, P., Wang, W., Song, T., Sanchez, J., ... & Xu, X. (2018). Two-dimensional itinerant ferromagnetism in atomically thin Fe3GeTe2. *Nature materials*, *17*(9), 778-782.

11. Ke, J., Yang, M., Xia, W., Zhu, H., Liu, C., Chen, R., ... & Wang, J. (2020). Magnetic and magneto-transport studies of two-dimensional ferromagnetic compound Fe3GeTe2. *Journal of Physics: Condensed Matter*, *32*(40), 405805.

12. Liu, S., Yuan, X., Zou, Y., Sheng, Y., Huang, C., Zhang, E., ... & Xiu, F. (2017). Wafer-scale two-dimensional ferromagnetic Fe3GeTe2 thin films grown by molecular beam epitaxy. *npj 2D Materials and Applications*, *1*(1), 1-7.

13. Verchenko, V. Y., Tsirlin, A. A., Sobolev, A. V., Presniakov, I. A., & Shevelkov, A. V. (2015). Ferromagnetic order, strong magnetocrystalline anisotropy, and

magnetocaloric effect in the layered telluride Fe3− δGeTe2. *Inorganic chemistry*, *54*(17), 8598-8607.

14. May, A. F., Calder, S., Cantoni, C., Cao, H., & McGuire, M. A. (2016). Magnetic structure and phase stability of the van der Waals bonded ferromagnet Fe 3− x GeTe 2. *Physical Review B*, *93*(1), 014411.

15. Kim, K., Seo, J., Lee, E., Ko, K. T., Kim, B. S., Jang, B. G., ... & Kim, J. S. (2018). Large anomalous Hall current induced by topological nodal lines in a ferromagnetic van der Waals semimetal. *Nature materials*, *17*(9), 794-799.

16. Park, S. Y., Kim, D. S., Liu, Y., Hwang, J., Kim, Y., Kim, W., ... & Ryu, H. (2019). Controlling the magnetic anisotropy of the van der Waals ferromagnet Fe3GeTe2 through hole doping. *Nano letters*, *20*(1), 95-100.

17. Lee, M., Williams, J. R., Zhang, S., Frisbie, C. D., & Goldhaber-Gordon, D. (2011). Electrolyte gate-controlled Kondo effect in SrTiO 3. *Physical review letters*, *107*(25), 256601.

18. Liang, V. K. C., & Tsuei, C. C. (1973). Kondo effect in an amorphous Ni 41 Pd 41 B 18 alloy containing Cr. *Physical Review B*, *7*(7), 3215.

19. Chen, B., Yang, J., Wang, H., Imai, M., Ohta, H., Michioka, C., ... & Fang, M. (2013). Magnetic properties of layered itinerant electron ferromagnet Fe3GeTe2. *Journal of the Physical Society of Japan*, *82*(12), 124711.

20. Liu, P., Liu, C., Wang, Z., Huang, M., Hu, G., Xiang, J., ... & Xiang, B. (2022). Planar-symmetry-breaking induced antisymmetric magnetoresistance in van der Waals ferromagnet Fe3GeTe2. *Nano Research*, *15*(3), 2531-2536.

21. Ke, J., Yang, M., Xia, W., Zhu, H., Liu, C., Chen, R., ... & Wang, J. (2020). Magnetic and magneto-transport studies of two-dimensional ferromagnetic compound Fe3GeTe2. *Journal of Physics: Condensed Matter*, *32*(40), 405805.

Chapter 4

Layer Dependence of the Longitudinal Resistivity, Anisotropy Field, and Curie Temperature of 2D Ferromagnets: $Fe_5Ge_2Te_2$ and Fe_3GeTe_2

4.1 Background and Motivation

Layered ferromagnets, a subset of the van der Waals family, exhibit many fascinating properties that have attracted a great deal of attention in the condensed matter physics community. $Fe_5Ge_2Te_2$ (FG2T) and Fe_3GeTe_2 (FGT) stand out among others due to their unusually strong magnetic anisotropy perpendicular to the atomic layers, metallicity, and high Curie temperatures.[1-3] The variation of the longitudinal resistivity for different thicknesses of FGT and its behavior is needed for further investigation. A comparison tool needed to track this change in longitudinal resistivity for different thicknesses. The reduction of Curie temperature was reported for FGT at low thicknesses; therefore, we need to study the thickness dependence of the Curie temperature in both FGT and FG2T as a generalized concept for any 2D layered ferromagnets and antiferromagnets.[2,4-5] The absence of a comparison of anisotropy energy of FG2T and FGT in the literature makes us revisit the anisotropy calculation from the magneto-transport measurement. 2D anomalous Hall conductivity per layer is reported to be 0.7 e^2/h at the large thickness limit in a density functional theory (DFT) calculation.[6] More interestingly, it was predicted by the same DFT calculations to oscillate at small thicknesses. Some experimental groups reported magneto-transport measurements data can be used to find the 2D conductivity.[1-3,7-11] It becomes an argument to confirm its intrinsic origin from an experimental point of view. The 2D quantized conductivity reveals the opportunity to study each layer contribution and

discover the interlayer interactions. The quantized 2D magnet is the future of spintronic applications.

4.2 Introduction

We have fabricated FG2T and FGT nanodevices with a range of thicknesses down to monolayers by exfoliating flakes from crystals grown by solid-state reaction as on the ref [7,8]. And we performed the magneto-transport measurements on the fabricated devices to extract the AH resistance and the LR. These two resistances help us to determine the AH conductivities. From the temperature dependence of the LR and AH measurements, we can determine the Curie temperature and longitudinal resistivity. By performing the saturation field in the hard-axis hysteresis loops, we can determine the anisotropy field. We compare the extracted data for different thicknesses down to the monolayer to study the effect of these properties as a function of thickness.[1-5,6-11]

4.3 Longitudinal Resistivity

Fig. 4.1 shows the value of longitudinal resistivity of the fabricated devices as a function of layer number (thickness) of FGT and FG2T at 300K. The longitudinal resistivity value is 405 um.cm for FG2T and it is 310 um.cm for FGT. These values are random, but it is in the range of the reported value of longitudinal resistivity of FGT flakes of 200-1000 um.cm and 405 um.cm for FG2T. Also, it is 300 um.cm for $Fe_{4.87}GeTe_2$ reported for FGT sister material. This is the typical range of the longitudinal resistivity of layered ferromagnetic materials.[1,3,5-11] There are different factors that may contribute to

43

this variation namely, chemical composite, purity, contact resistance, thickness. The temperature and time in the solid state reaction method used to grow the FGT crystals can directly contribute to the purity in the final crystal structure.[1-3,7,8,10] Also, the air exposure can affect the purity of the flakes due to easily oxidizing and degradation over time.[2,3,7-10] This slow rate of degradation can potentially be used to estimate the longitudinal resistivity without worry about changing the value (See Chapter 2.1). The existence of a barrier that needs to be broken in order to get a very good contact is still an arguing point. A reasonable high voltage breaks the barrier with relatively medium current density is a solution.[2,3,7,8,10] We develop a new additional step to get a very low contact resistance and stable device (See Chapter 2.1). **Fig. 4.2** shows $\rho_{xx}(T)/\rho_{xx}(300K)$ of FGT and FG2T as a function of temperature. **Fig 4.3** shows $(\rho_{xx}(2K)-\rho_{xx}(300K))/\rho_{xx}(300K)$ % as a function of the number of layers for FG2T and FGT. There is a large variation from the thick flakes down to thin flakes and a transition point from a metallic to insulating exists in both of the materials. A clear metallic behavior above 4L of FGT and FG2T flakes while it becomes insulating by reducing the layer number. Deng, Y. et al. reported the same behavior in different numbers of layers of FGT flake.[2] They show R/R(240K) as a function of temperature down to the monolayer. Their observation is similar to what we measure in our FGT and FG2T devices. Our data confirm this and generalize it to any layered metallic ferromagnets.
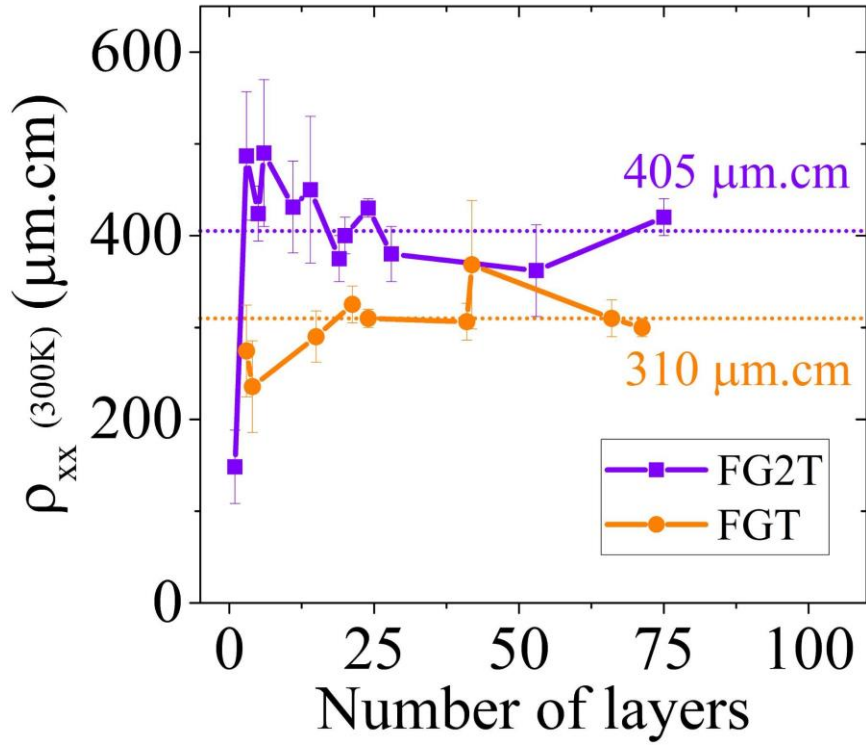
Fig. 4.1. Layer dependence of the longitudinal resistivity. The measured longitudinal resistivity of different fabricated flakes of FGT and FG2T at 300K. The average room temperature value of longitudinal resistivity of FGT is 310 um.cm and it is 405 um.cm for FG2T.
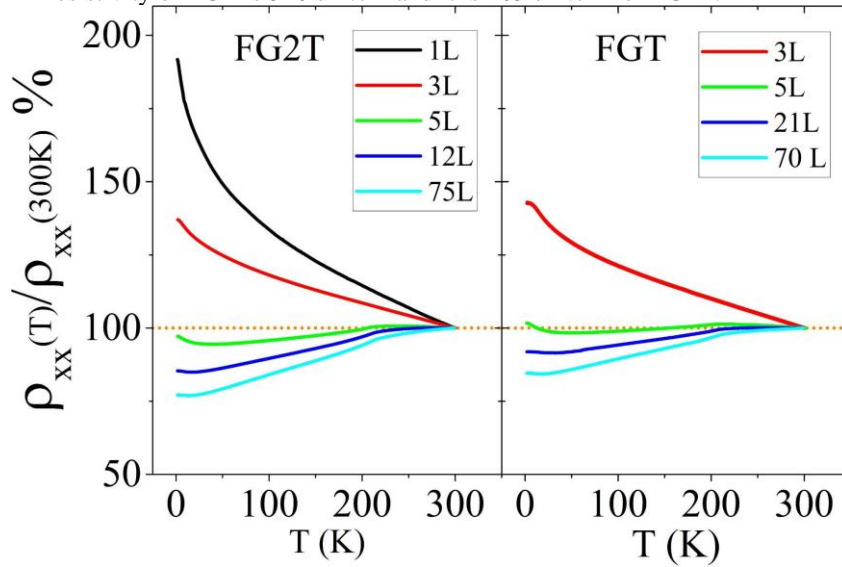
Fig. 4.2. Temperature Dependence of the flake longitudinal resistivity of FG2T and FGT. The longitudinal resistivity with varying

number of layers up to 75L. The longitudinal resistivity is normalized by their values at 300K. The typical behavior of all thick flakes (cyan) is also shown for reference.
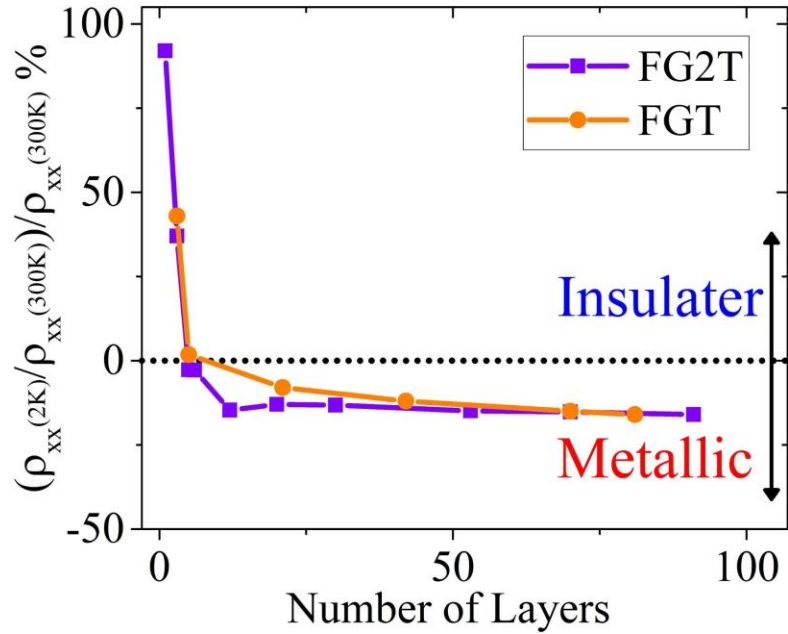
Fig. 4.3. Layer Dependence of the Residual Resistivity.
$(\rho_{xx}(2K)/\rho_{xx}(300K))/\rho_{xx}(300K)$ % as a function of the number of layers for FGT and FG2T. FGT and FG2T flakes have an insulator behavior below 4 Layer while they are metallic above that.

4.4 Anomalous Hall Resistance

Fig. 4.4 shows a selected AH resistances as a function of applied field for FGT and FG2T at 2K. The squire loop is common in thick flakes of FGT and FG2T for 4L and above. The loop shape is tilted for 3L and below for FGT and FG2T. Many reported the tilted shape of thinner FGT and the squire for a thickener one.[1,2,6] **Fig. 4.5** shows MR as a function of the applied field of a selected FGT and FG2T flakes. The linear MR is common

46

is up to 10 kOe. MR is 1 Ohms for both 3L of FGT and FG2T. It has been report this linear

response in FGT and FG2T is also have the same feature.[2,6]
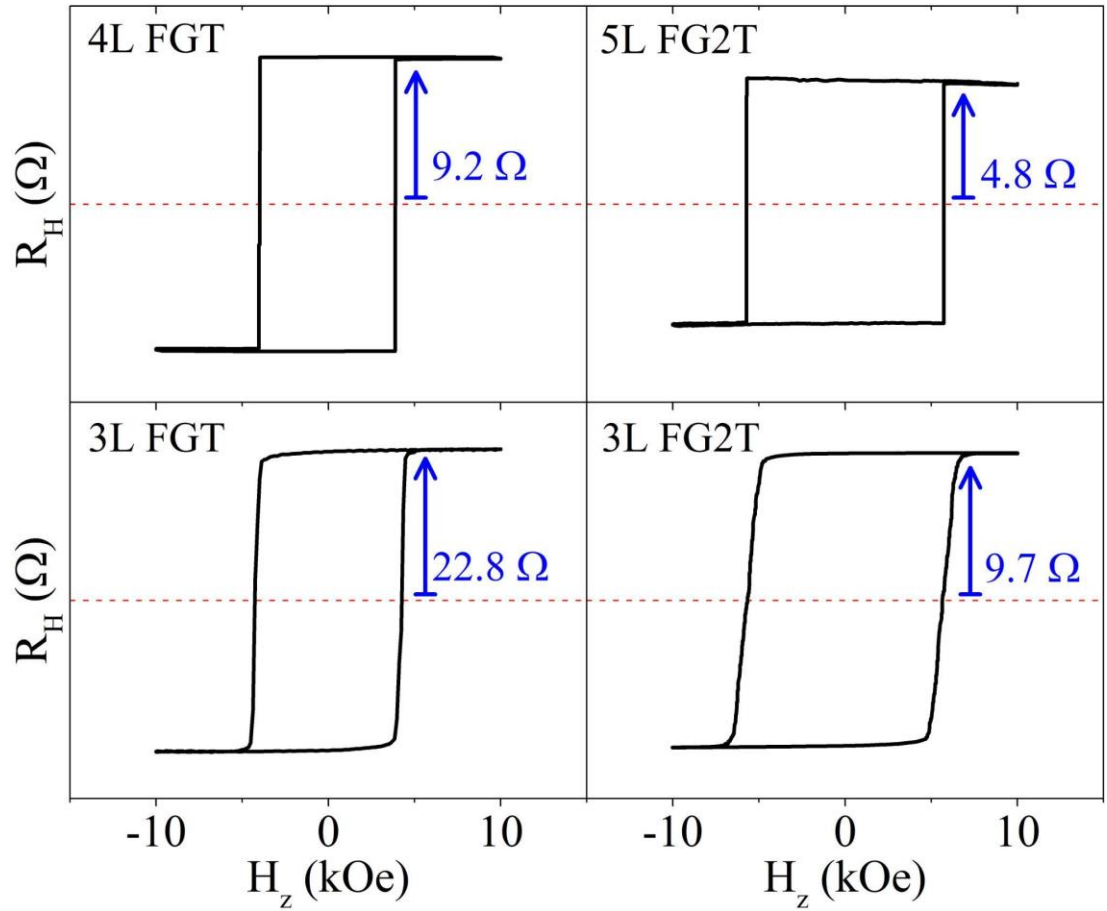
Fig. 4.4. AHR of a selected Flakes at 2K. The squire shape is typical in <4L of FGT and <5L of FG2T. The loop of 3L of FGT and FG2T is shown for comparison.
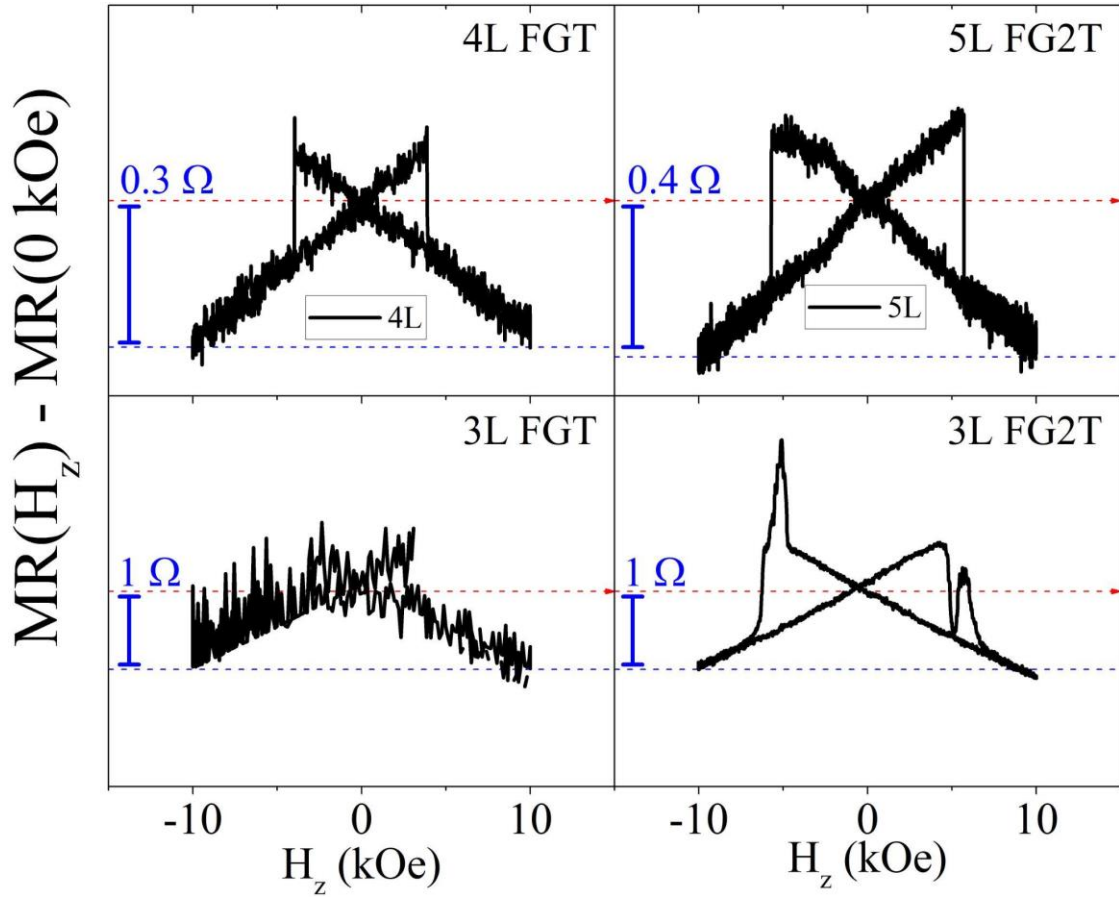
Fig. 4.5. MR of a Selected Flakes at 2K. MR is linear up to 10 kOe applied out of the plane field. MR of 3L of FGT and FG2T is about 1 Ohm and it is 0.3 Ohms for 4L FGT and 0.4 Ohms for 5L FG2T.

Fig. 4.7 shows the anomalous Hall resistance as a function of applied out of plane field for thin 3L flakes of FGT(A) and FG2T (B). The thin flake is showing a tilted square shape even at a very low temperature. The only assumption is that a weak magnetization of the flake. This agrees with the anisotropy field reduction with the same flake at **fig. 4.13**. The loop shape of the AH measurements agrees with the behavior in the measured device of 3L in ref **2**. While for thick flake **fig. 4.6** the AH resistance loop has a square shape at low temperatures, it starts to deviate from the square shape at high temperatures before it vanishes at the Curie temperature. The tilted shape indicates that the magnetic anisotropy

changes from out of plane to in plane. **Fig. 4.6** shows anomalous Hall resistance as a function of applied out-of-plane field for 75L FG2T and 20L FGT. **Fig. 4.6** and **4.7** represent the evolution from the ferromagnetic phase of FG2T and FGT to the paramagnetic phase across the Curie temperature T_c.
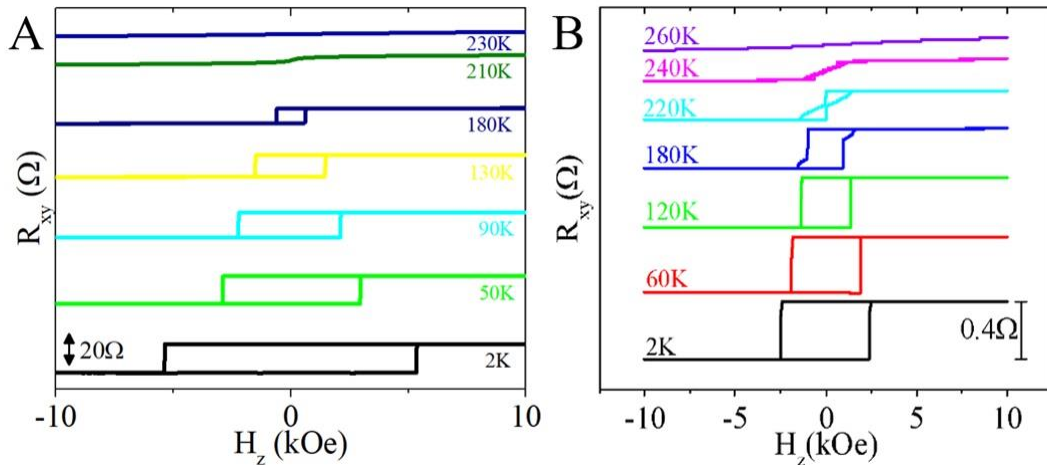
Fig. 4.6. Field Dependence of AHR at Different Temperatures. (A) AH resistance as a function of applied out of plane for 12L FGT from 2K to 230K. (B) AH resistance as a function of applied out of plane for 75L FG2T from 2K to 260K. At 2K, the loop shape is squire and shrinks by increasing temperature until it collapses at near Tc. Ordinary Hall is showing at a temperature above Tc, 230K for FGT and 260K for FG2T.
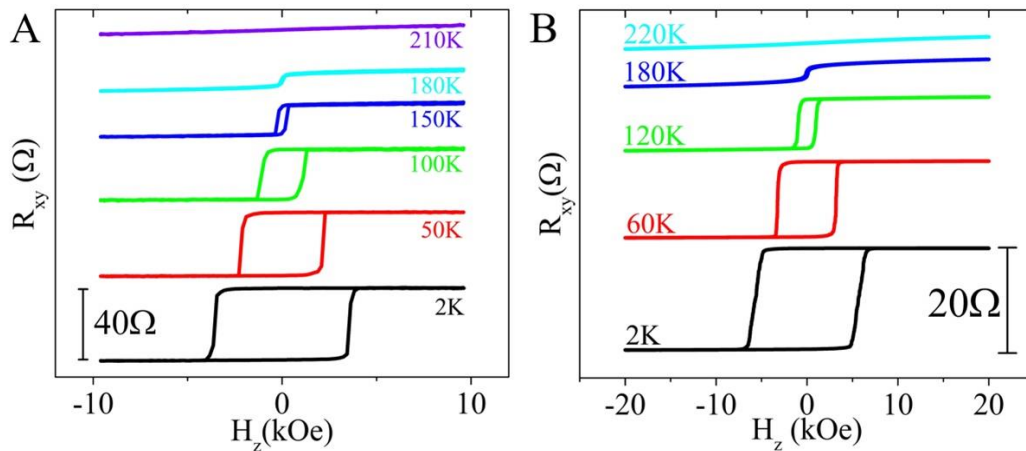
Fig. 4.7. Field Dependence of the 3L AH at different temperatures. AH response for 3L FGT (A) and 3L for FG2T (B) after applying out of plane field.

Now, let us look at the anomalous Hall resistance at zero field divided by the anomalous Hall resistance at the saturated field. This quantity is called the squareness of the anomalous Hall resistance loop. We can see in **fig. 4.5** that the loop squareness for the 22L thick flake has a sharp transition while it has a gradual transition for the 5L one of FGT. This transition is associated with the out of plane to in plane transition before the anomalous Hall gives place to the ordinary Hall signal. Similar features are observed for different thicknesses and for FGT and FG2T, indicating that magnetic anisotropy is weak in thinner flakes.
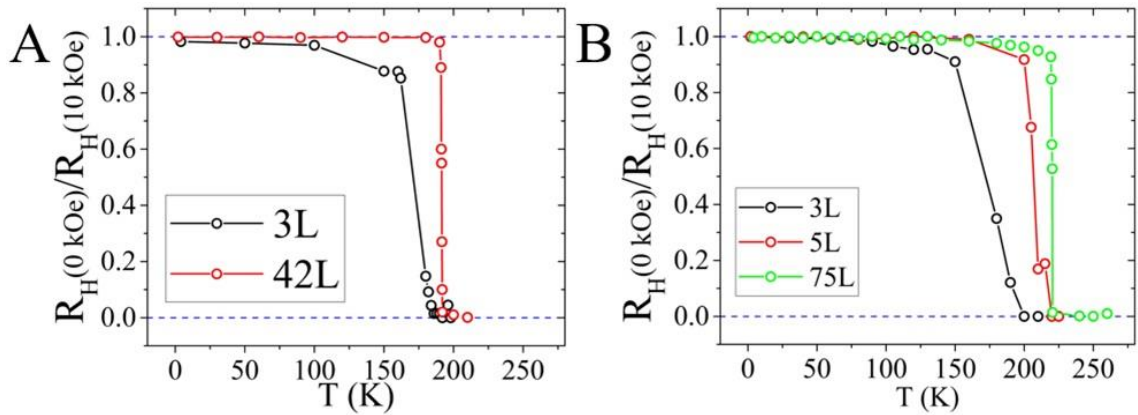
Fig. 4.8. Squareness of AHR loop. R_H(0 kOe)/R_H(10 kOe) as a function of temperature for FGT (A) and FG2T (B). The thickener flakes show a sharp transition at 191K for FGT (A) and 221 K for FG2T (B). This transition starts gradually expanding transit in a lower temperature.

Fig. 4.9 shows the temperature dependence of AH magnitude of the typical thicker flakes of FGT and FG2T. It is clear that the magnetization demolishes at 225K for FGT and 255K for FG2T correspond with Curie temperature. If we look at the special case of 3L for both FGT and FG2T **Fig. 4.10 (A)**. The AH magnitude as a function of temperature is somehow linear. This increase at low temperature is associated with the insulator behavior in the longitudinal resistance **Fig 4.2**.
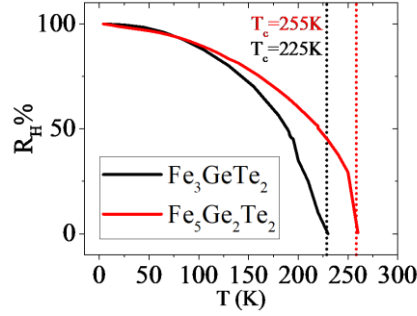
Fig. 4.9. Temperature Dependence of AH Magnitude.
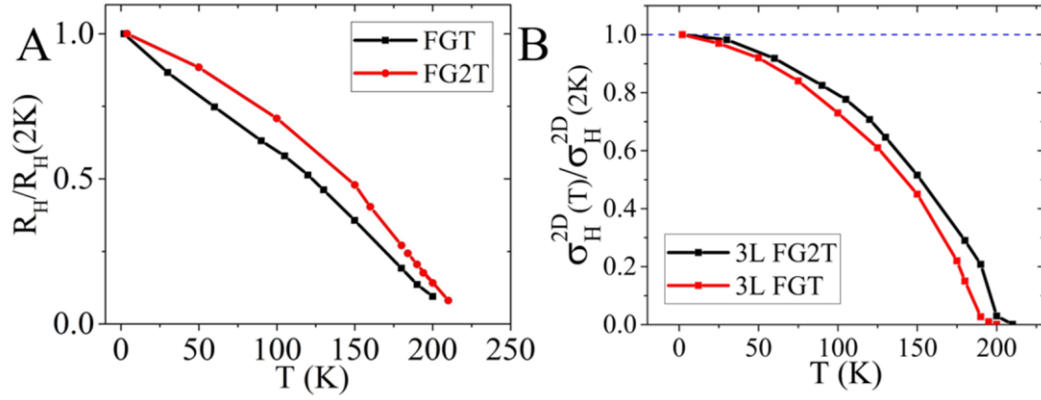
Fig. 4.10. Temperature Dependence of AH and Conductivity.

The anomalous Hall conductivity is calculated by using the equation $\sigma_{yx}^{2D} =$

$\frac{\rho_{xy}^{2D}}{\rho_{xy}^{2D^2} + \rho_{xx}^{2D^2}}$. This equation describes the 2D conductivity where $\rho_{xy}^{2D} = R_{xy}$ and $\rho_{xy}^{2D} = \frac{R_{xx}W}{L}$.

Fig.10 (B) shows The AH conductivity of 3L FGT and FG2T. The AH conductivity solves

the increase at low temperature. **Fig. 4.11 (A)** shows the 2D anomalous Hall conductivity

as a function number of layers. We find the anomalous Hall conductivity is approximately

proportional to the number of layers over a large range of thicknesses and it is higher for

FG2T than FGT. Each layer of FG2T contributes to the anomalous Hall conductivity by

0.13 e^2/h and each layer of FGT contributes by 0.1 e^2/h. Others reported similar linear

responses, but the slope (each layer contribution) varies.[4-6] **Fig. 4.11 (B)** shows the 2D

51

longitudinal conductivity as a function of the number of layers. The longitudinal conductivity has a linear response with the number of layers at each layer of FGT is contributed by 7.91 e^2/h higher than for FG2T of 6.93 e^2/h.

We find in our experiments that each layer contributes by about $0.1e^2/h$ to the total anomalous Hall conductivity. If we compare our data to the data reported previously, we find the following. It is 1.5 e^2/h calculated in Ref 9. It is about 0.1 e^2/h calculated in Ref 1 that agrees with our data while it is 0.05 e^2/h calculated in Ref 10 that is an even smaller slope than our data of 0.05 e^2/h. Theoretical calculations of the conductivity giving the bulk value of 0.7 e^2/h [4] which only agrees with only one ref 11. This variation can be attributed to many other extrinsic factors including oxidation, degradation, contact, and current. But the linear dependence is resembling the material response or an intrinsic property of FGT.
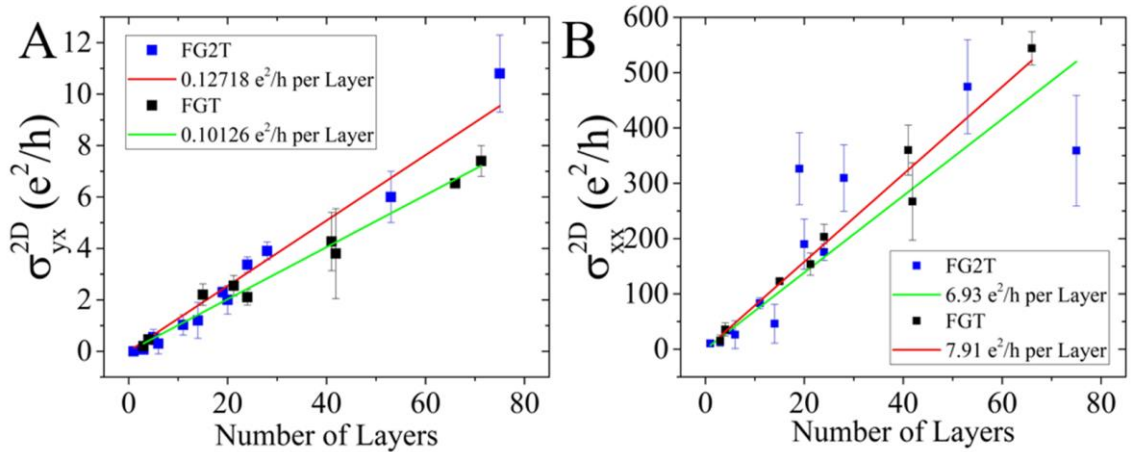
Fig. 4.11 Layer Dependence of AH and Longitudinal Conductivity.

4.5 Anisotropy Field

Fig. 4.12 shows the anomalous Hall resistance data as a function of temperature for different magnetic field angles with respect to the perfectly aligned angle perpendicular to the zero-field FGT magnetization, i.e., the atomic layers. At zero degree, the anomalous

Hall resistance signal almost vanishes in magnitude with some remaining features associated with the magnetization response. The anisotropy field of 15L FGT is about 61 kOe at 2K. **Fig. 4.13** shows the in-plane dependence of AH for 75L and 3L of FG2T. The anisotropy field is about 53 kOe for 75L FG2T and 45 kOe for 3L FG2T at 2K. **Fig. 4.14** shows the anisotropy field as a function temperature for 3L and 75L FG2T. It is decreasing linearly by increasing temperature. This linear response is common in all of the measured FGT and FG2T. Many report this linear decrease. **Fig. 4.15** shows the anisotropy field as a function of the number of layers for FGT and FG2T at 2K. It approaches constant when the thickness is above 10 layers. **Fig. 4.16** shows the coercive field extracted from AH measurements as a function of temperature. The coercive field decreases linearly with increasing temperature and is common in FGT. **Fig. 4.17** shows the coercive field at 2K as a function of thickness. The random variation due to multi domain existence in FGT and FG2T flakes.
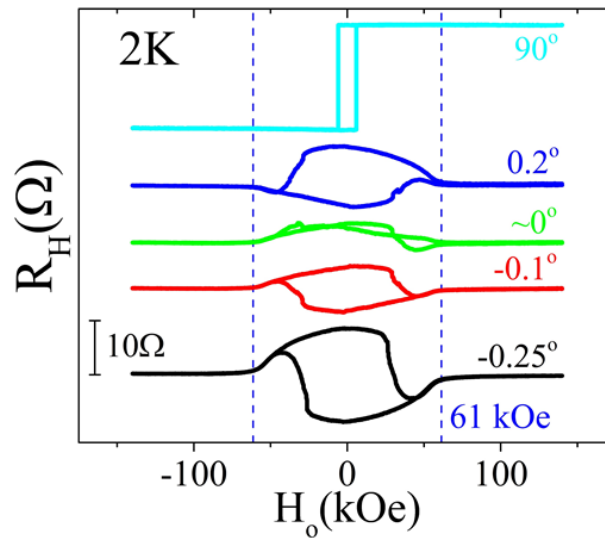
Fig. 4.12. Angular Field Dependence of AH. AHR as a function of applied field at 2K for different angles.
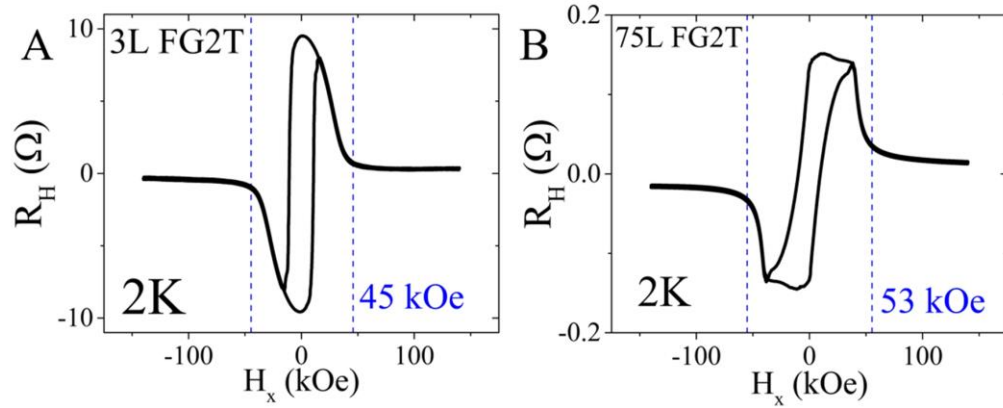
Fig. 4.13. In Plane Field Dependence of AH. AHR as a function of applied in-plane field at 2K for (A) 3L and, (B) 75L FG2T.
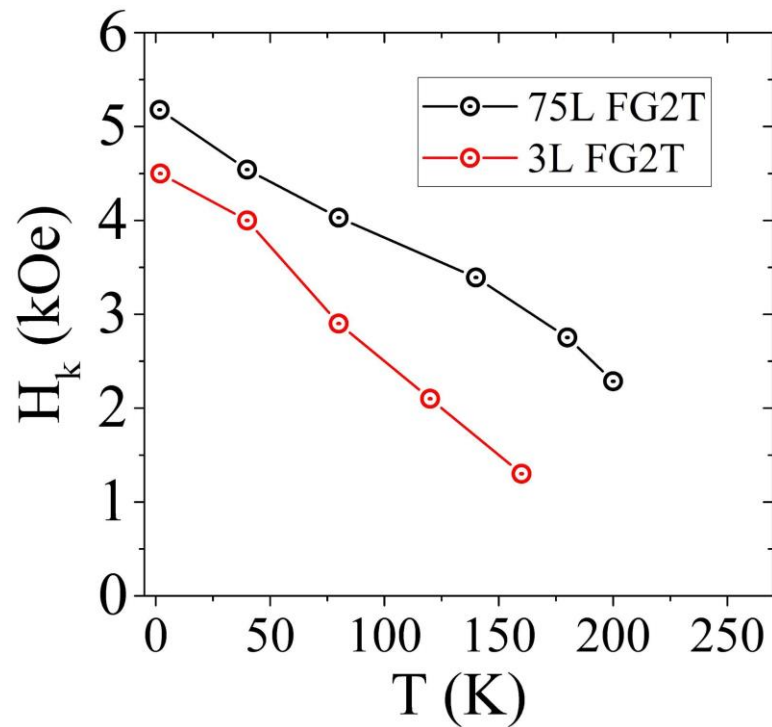
Fig. 4.14. Temperature dependence of Anisotropy field. H_k as a function temperature for 75L and 3L FG2T. The Anisotropy field linearly decreases by increasing the temperature and it is higher for 75L than 3L. The anisotropy field at zero temperature is 53 kOe for 75L and 45 kOe for 3L.
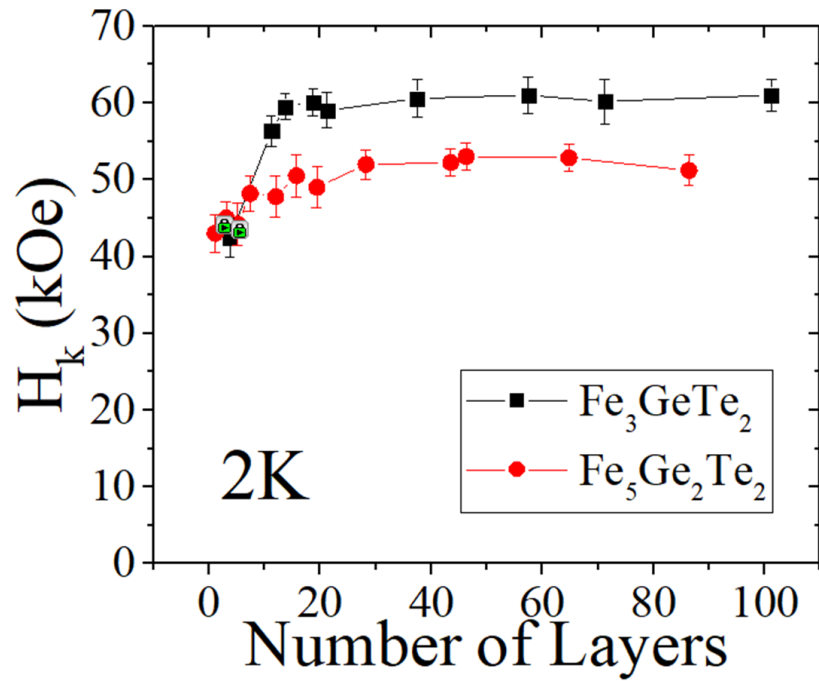
Fig. 4.15. Layer Dependence of Anisotropy Field. H_k as a function of thickness for FG2T and FGT. Hk saturates above 10L and reduced at low thickness.

Now, let us look at the coercive field data. **Fig. 4.6** shows the coercive field as a function of temperature. The coercive field linearly decreases by increasing the temperature before it vanishes near Curie temperature at a rate of -45 Oe/K. The linear decreasing rate is very common in FGT and FG2T.
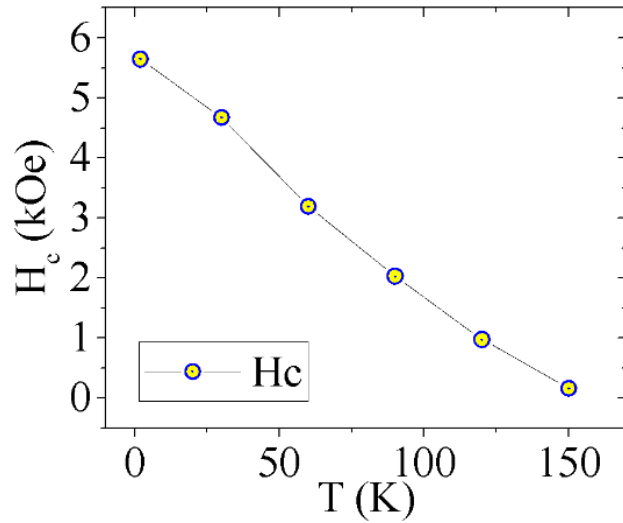
Fig. 4.16. Temperature Dependence of Coercive Field. The
temperature dependence of coercivity obtained from the AH data.
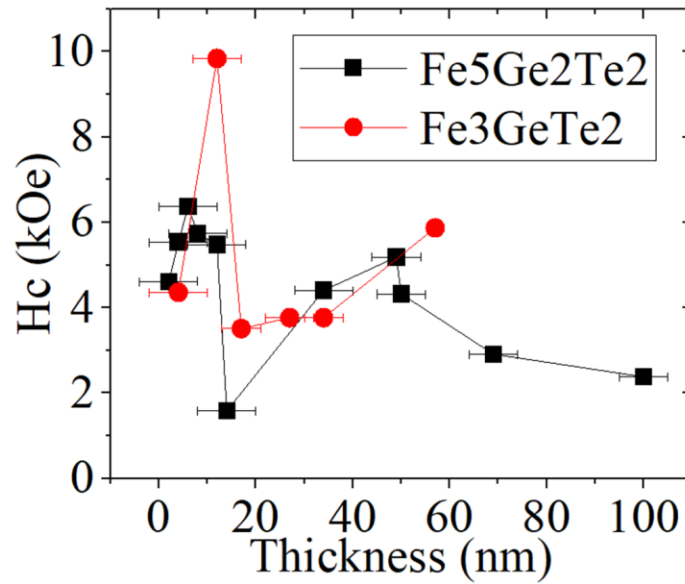
Fig. 4.17. Layer dependence of the Coercive Field.

4.6 Curie Temperature

Fig. 4.18 shows the AH measurements near Curie temperature. **Fig. 4.19** and **4.20**

show the Arrott plot used to determine the Curie temperature from the magnetization. The

zero intercept the correct reading of Curie temperature. Here we use the magneto-transport measurements as a tool to probe the magnetization. The method used to get the plot found in[7,8] and, in 5.12.1. We notice that the Curie temperature in FG2T is higher than that in FGT. The bulk value is about 255K for FG2T and 225K for FGT. **Fig. 4.21** shows T_c as a function of the number of layers. T_c decreases sharply below 6L for both FGT and F2GT. This drop in Curie temperature agrees with the trend reported in.[1-3,5] Our set of data in **fig. 4.7** and the previously reported data[1-3,5] is a clear indication of the reduction T_c for low thickness generally in all 2D magnetic materials.
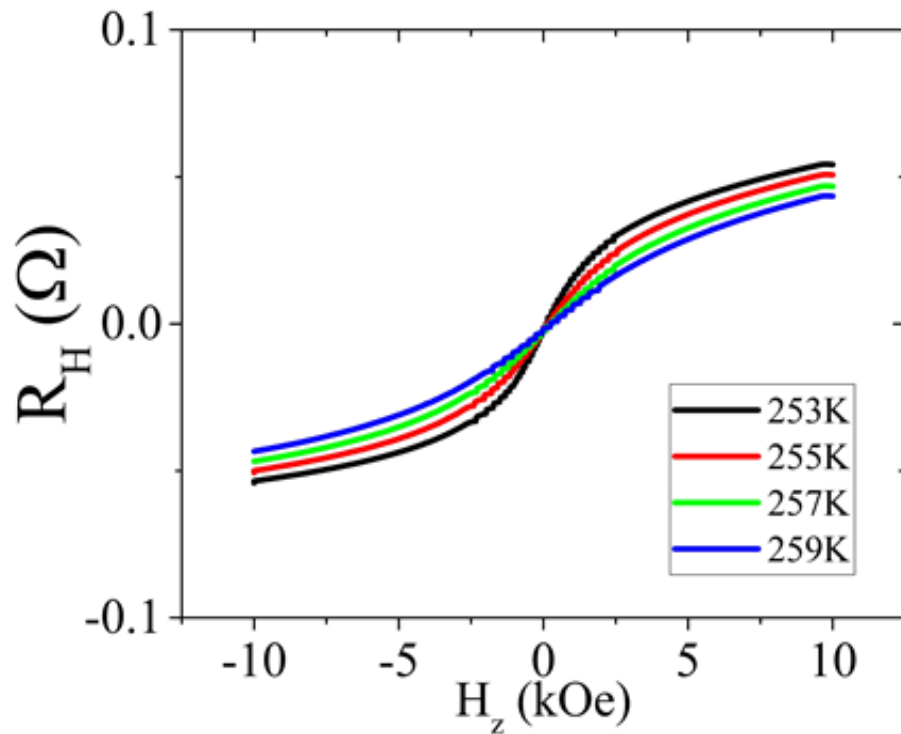
Fig. 4.17 Near Tc Field dependence of AH Resistance. There is a clear transition from the soft magnet behavior to ordinary Hall behavior.
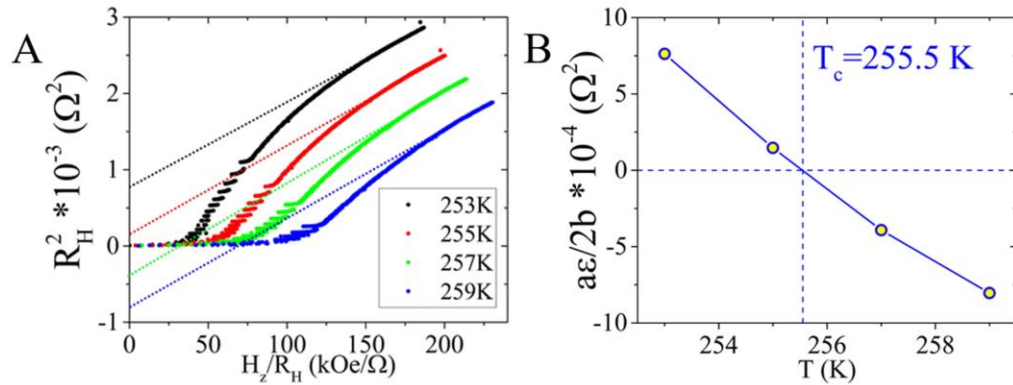
Fig. 4.18 Determination of Curie Temperature for 75L FG2T. (A) The squared AH resistance as a function of H_z/R_H. The extrapolation of the saturation of the squared AH resistance at H_z/R_H(0 kOe/Ohms) is shown. (B) The y-intercept of the Arrott plot as a function of the temperature, where, a/2b, is a constant and $\varepsilon=(T-Tc)/Tc$. The zero-crossing point is the Curie temperature.
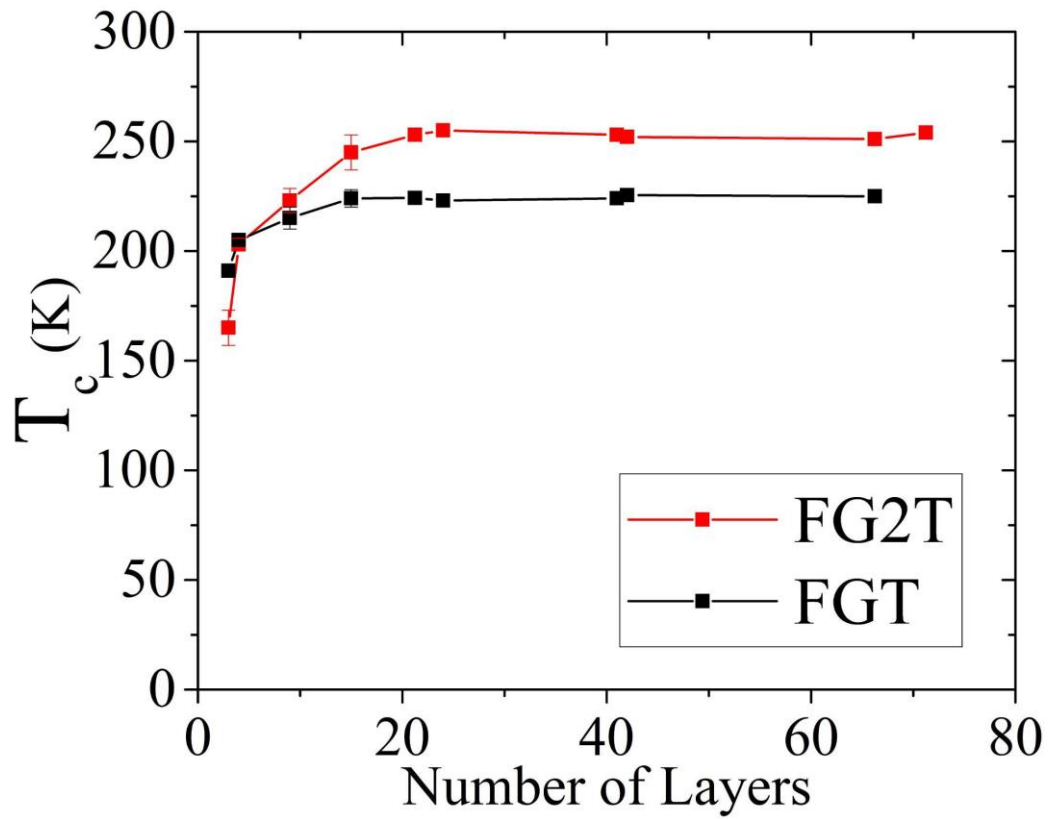
Fig. 4.19. Layer Dependence of Curie Temperature. T_c as a function thickness for FG2T and FGT. Tc saturates for the thicker flakes and drop below 6L for both FGT and FG2T.

4.7 Summary

The residual longitudinal resistance can be used to identify the number of layers (thickness) of metallic layered ferromagnets FGT and FG2T. The Curie temperature is higher for FG2T than FGT, and both sharply drop at low thickness (< 6 L). Indicating a change of the material strength in the 2D limit system and a proof that each layer can contribute to the flake magnetization. The anisotropy field of FG2T is smaller than in FGT. And it agrees with the energy calculated from the crystal structure of FGT. The anomalous Hall conductivity is approximately proportional to the number of layers, and it is higher for FG2T than for FGT. This response can indicate intrinsic properties of FGT.

References

1. Fei, Z., Huang, B., Malinowski, P., Wang, W., Song, T., Sanchez, J., ... & Xu, X. (2018). Two-dimensional itinerant ferromagnetism in atomically thin Fe3GeTe2. *Nature materials*, *17*(9), 778-782.

2. Deng, Y., Yu, Y., Song, Y., Zhang, J., Wang, N. Z., Sun, Z., ... & Zhang, Y. (2018). Gate-tunable room-temperature ferromagnetism in two-dimensional Fe3GeTe2. *Nature*, *563*(7729), 94-99.

3. Gong, C., Li, L., Li, Z., Ji, H., Stern, A., Xia, Y., ... & Zhang, X. (2017). Discovery of intrinsic ferromagnetism in two-dimensional van der Waals crystals. *Nature*, *546*(7657), 265-269.

4. Lin, X., & Ni, J. (2019). Layer-dependent intrinsic anomalous Hall effect in Fe 3 GeTe 2. *Physical Review B*, *100*(8), 085403.

5. Roemer, R., Liu, C., & Zou, K. (2020). Robust ferromagnetism in wafer-scale monolayer and multilayer Fe3GeTe2. *npj 2D Materials and Applications*, *4*(1), 1-7.

6. Liu, S., Yuan, X., Zou, Y., Sheng, Y., Huang, C., Zhang, E., ... & Xiu, F. (2017). Wafer-scale two-dimensional ferromagnetic Fe3GeTe2 thin films grown by molecular beam epitaxy. *npj 2D Materials and Applications*, *1*(1), 1-7.

7. Alghamdi, M., Lohmann, M., Li, J., Jothi, P. R., Shao, Q., Aldosary, M., ... & Shi, J. (2019). Highly efficient spin–orbit torque and switching of layered ferromagnet Fe3GeTe2. *Nano letters*, *19*(7), 4400-4405.

8. Jothi, P. R., Scheifers, J. P., Zhang, Y., Alghamdi, M., Stekovic, D., Itkis, M. E., ... & Fokwa, B. P. (2020). Fe5− xGe2Te2—a New Exfoliable Itinerant Ferromagnet with High Curie Temperature and Large Perpendicular Magnetic Anisotropy. *physica status solidi (RRL)–Rapid Research Letters*, *14*(3), 1900666.

9. Tan, C., Lee, J., Jung, S. G., Park, T., Albarakati, S., Partridge, J., ... & Lee, C. (2018). Hard magnetic properties in nanoflake van der Waals Fe3GeTe2. *Nature communications*, *9*(1), 1-7.

10. Zhang, K., Han, S., Lee, Y., Coak, M. J., Kim, J., Hwang, I., ... & Park, J. G. (2021). Gigantic current control of coercive field and magnetic memory based on nanometer-thin ferromagnetic van der Waals Fe3GeTe2. *Advanced Materials*, *33*(4), 2004110.

11. Xu, J., Phelan, W. A., & Chien, C. L. (2019). Large anomalous Nernst effect in a van der Waals ferromagnet Fe3GeTe2. *Nano Letters*, *19*(11), 8250-8254.

Chapter 5

Highly Efficient Spin-Orbit Torque and Switching of Layered Ferromagnet Fe₃GeTe₂

5.1 Background and Motivation

Fe_3GeTe_2 (FGT), a layered conducting ferromagnet, is an important member of the van der Waals (vdW) material family that has attracted a great deal of attention.[1,2] Similar to other known vdW ferromagnets such as $Cr_2Ge_2Te_6$ and CrI_3, FGT possesses the magnetic anisotropy perpendicular to the atomic layers which is retained down to monolayers. Different from the others, FGT stands out due to the following attractive properties. First, not only do FGT bulk crystals have the highest Curie temperature T_c (~230 K) but monolayer FGT also has the highest T_c (130 K) when compared to their vdW ferromagnetic counterparts.[1,3,4] Furthermore, the T_c of thin FGT can be dramatically elevated to room temperature using electrostatic gating.[2] Second, few-layer thick FGT films have been successfully grown by molecular beam epitaxy,[5] which makes ultimate wafer-scale monolayer all-vdW heterostructure fabrication possible. Third, although the other vdW magnets are semiconductors or insulators, FGT is a ferromagnetic metal which allows for studying its magnetism via magneto-transport measurements.

In conventional devices using conducting ferromagnets with perpendicular magnetic anisotropy (PMA) such as CoFeB, spin−orbit torques (SOT) have been exploited for switching the magnetization.[6] SOT efficiency, the figure-of merit for this application, contains both intrinsic properties such as the spin Hall angle of the heavy metals serving as the spin current source and extrinsic properties such as the transmission coefficient. The latter depends on the ferromagnet/heavy metal interface quality. Because of the vdW nature

that provides an atomically flat interface, FGT has the potential of having high SOT efficiency for switching its magnetization, especially in all-vdW heterostructures.

5.2 Introduction

In this work, we investigate the SOT effects in FGT/Pt heterostructure devices containing thin exfoliated FGT and sputtered Pt. In such devices, the spin Hall effect in Pt produces a pure spin current which enters the FGT layer and exerts on it both field-like and damping-like torques.[7] Different from magnetic insulator devices in which the magnetization state is read out by the induced anomalous Hall effect (AHE) in Pt via proximity coupling,[8,9] the large AHE response in FGT lends itself a sensitive detector of its own magnetization state. To quantify the effects of SOT, we carry out two types of measurements: pulsed current switching and second harmonic Hall measurements. From both measurements, we demonstrate that the SOT efficiency in FGT/Pt is significantly larger than that in devices containing conventional three-dimensional (3D) magnetic insulators and comparable with that in the best devices containing 3D ferromagnetic metals. In addition, we have observed SOT-induced switching of FGT magnetization with high switching efficiency.

5.3 Crystal Characterization

Fe_3GeTe_2 crystals were grown by solid-state reaction of the elements at 800 °C within 5 days. After mixing the elements Fe, Ge, and Te in their stoichiometric molar ratio, the mixture was pressed into a pellet, sealed in a quartz glass ampule under vacuum and loaded into the furnace for reaction. **Fig. 5.1** shows the X-ray diffraction (XRD) pattern of a bulk FGT single crystal which agrees with the literature.[10–14] The XRD pattern contains only

the (0 0 2n) Bragg peaks (n = 1, 2, 3, 4, 5, 6), indicating that the exposed surface is the ab-plane of the FGT crystal. Indexation of the peaks led to the c lattice parameter of 16.376 Å, which is consistent with the previously reported value.[10]
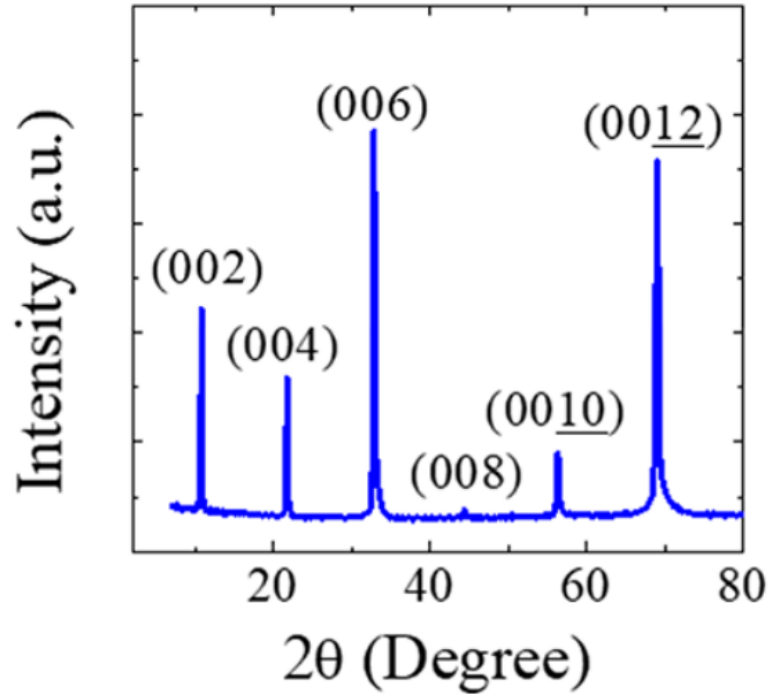
Fig. 5.1 X-ray Diffraction of FGT Crystal. Characterization of FGT bulk crystal by X-ray diffraction pattern for bulk FGT single crystal`s ab-plane.

5.4 Magneto-Transport Measurements

To characterize the magnetic properties of FGT, we have carried out AHE measurements. The fabrication consists of the following steps. We start with FGT crystals. After exfoliation, we locate a desired flake and perform electron beam lithography (EBL) and lift-off to fabricate Pt (30 nm) contacts to the chosen FGT flake. The process for the FGT only devices is similar to what will be illustrated in Figure 4.4 for FGT/Pt heterostructure devices except that there are fewer steps here.

The hysteresis loops of the anomalous Hall resistivity ρ_H for an FGT device with a thickness of 53 nm are displayed in **Fig. 5.2** for different temperatures ranging from 2 to 230 K (device image is shown in the inset of **Fig. 5.3**). Below 180 K, the ρ_H loops are squared with monotonically increasing coercive field H_c as the temperature is decreased. H_c reaches ∼7.5 kOe at 2 K, indicating very strong PMA. At 180 K, where we perform all SOT measurements to be presented later, H_c is ∼0.65 kOe. In hard-axis Hall measurements, we find the saturation field, denoted as H_k, to be ∼30 kOe, which is 46 times larger than Hc. Above 180 K, the ρH loops deviate from the squared shape, collapse at ∼210 K, and finally disappear at ∼230 K.
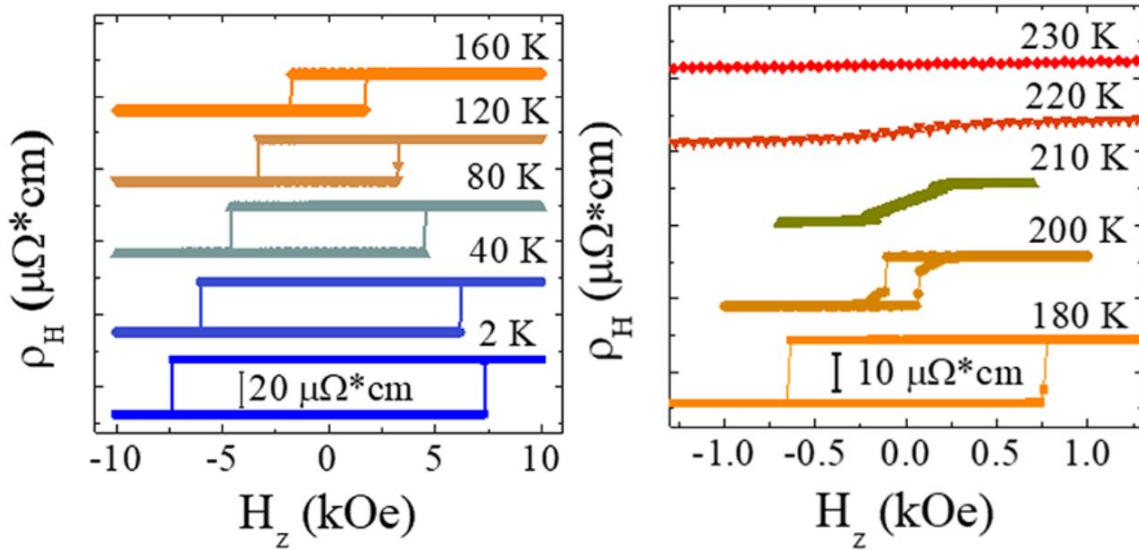
Fig. 5.2 Magneto-Transport of FGT flake. Characterization of FGT flakes by Hall resistivity as a function of applied field for a 53 nm thick flake of FGT at selected temperatures from 2−230 K.

In the meantime, the magnitude of ρ_H loops, that is, the height between the two saturated values, decreases as the temperature is raised and vanishes at the Curie temperature T_c as illustrated in **Fig. 5.3**. T_c of this FGT device is found to be ∼225 K. A more accurate

determination of Tc from the Arrott plot gives T_c = 224.5 K for the same device (see **Fig. 5.10**). The overall temperature dependence of ρ_H resembles but is slightly steeper than the mean-field magnetization of FGT (see Figure 4.3). We note that the low-temperature M_s value ranges from 285 to 393 emu/cm^3 . [11,15−19] Because most of our SOT experiments are carried out at 180 K, we take M_s = 170 emu/cm^3 at 180 K from ref 11, which is the lower-bound M_s value for FGT. Using this M_s value and the measured anisotropy field H_k, we obtain the minimum uniaxial PMA energy of 1.1×10^7 erg/cm^3 at 180 K, which is nearly 2 orders of magnitude greater than that of CGT of 1.4×10^5 erg/cm^3 at ∼4 K.[20]
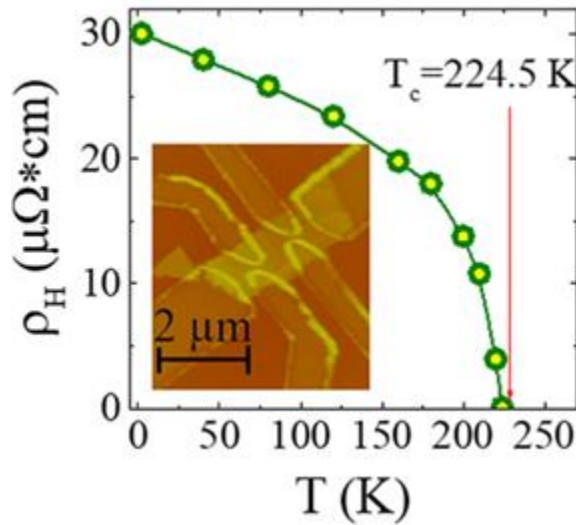
Fig. 5.3 Temperature Dependence of AH resistivity. Measured Hall resistivity as a function of temperature for the same FGT device with T_c determined by the Arrott plot (see Figure 5.10) labeled. Inset shows the AFM topographic image for our FGT device.

5.5 FGT/Pt Heterostructure Fabrication

To fabricate FGT/Pt bilayer devices for the SOT study, we adopt the fabrication processes as represented in **Fig. 5.4**. FGT flakes are first exfoliated from a small crystal shown in **Fig. 5.4A** and placed on a Si/SiO2 wafer. As schematically shown from **Fig. 5.4B−E**, a

65

suitable flake is chosen (**Fig. 5.4B**) and covered with a 5 nm layer of Pt (Fig. 5.4C) by sputtering. Cr (5 nm)/Au (85 nm) electrodes are formed by EBL, e-beam evaporation, and lift-off (**Fig. 5.4D**). The continuous Pt film covering the flake is etched by inductively coupled plasma to form isolated Cr/Au electrodes (**Fig. 5.4D**). The scanning electron micrograph of a final device is shown in **Fig. 5.4F**. Atomic force microscopy (AFM) imaging of both FGT and FGT/Pt (see **Fig. 5.11**) indicates atomic level flatness with the root-mean-square roughness of 0.2 nm, which is smaller than the atomic step height of FGT (0.8 nm).[2] and FGT layers, the former generates SOTs to act on the magnetization of the latter.

Fig. 5.4 Fabrication process for FGT/Pt hybrid devices. (A) Optical microscopic image of a bulk FGT piece on scotch tape. (B–E) Illustration of the fabrication process. First, FGT flakes are exfoliated onto 300 nm thick SiO2 substrates and a suitable flake is located, (B),

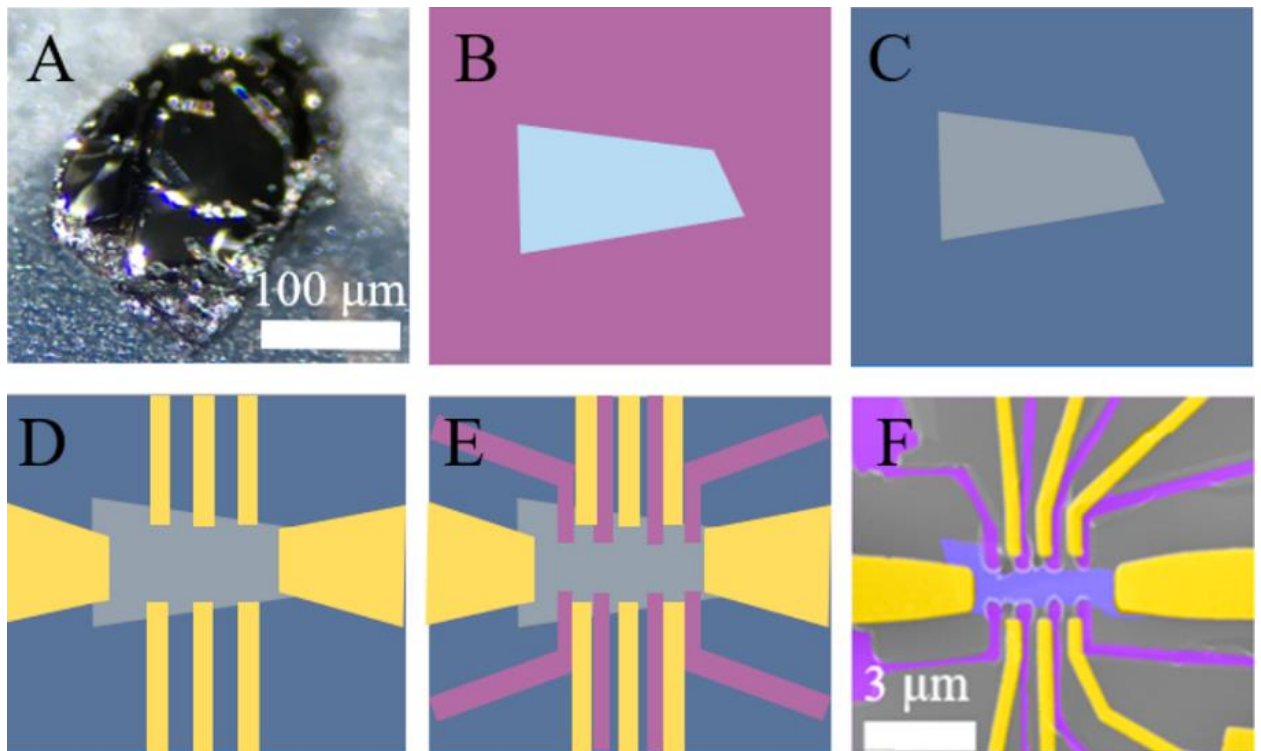followed by sputtering 5 nm of Pt, (C), then electrodes are placed on the flake, (D), and last the Pt and FGT is etched in order to define the Hall geometry and to remove any Pt connections between the electrodes, (E). (F) False-colored SEM image of the FGT (15 nm)/ Pt (5 nm) device used for SOT-induced magnetization switching. The device dimensions are 2.75 μm × 1 μm.

5.6 Switching FGT Magnetization

In the pulsed current switching experiments, we pass current pulses increasing in amplitude and interrogate the FGT magnetization state by measuring the AHE resistivity, ρ_H, after each pulse through a small constant current bias. As the current reaches a threshold, the magnetization state of FGT switches and produces a sign reversal of ρ_H. We measure the critical currents for different in-plane fields. To more accurately determine the current flowing in Pt which is responsible for the SOT acting on FGT, we use a parallel resistor model with resistivities measured separately for 5 nm Pt on SiO_2 and 53 nm FGT flake (see **Fig. 5.12**). To confirm the resistivity of the 5 nm Pt film, we deposit a 5 nm thick Pt on $Cr_2Ge_2Te_6$ which provides a comparable flat surface to FGT but does not shunt much current due to much higher resistance than Pt. The measurement results are compared in **Fig. 5.13**.

Before turning on sizable SOT, we first prepare the initial state of the FGT magnetization by applying an in-plane field H_x. **Fig. 5.5** is the AHE response of the FGT (15 nm)/Pt (5 nm) device to an H_x sweep measured at 180 K with a 50 μA current, which produces negligible SOT. This is a typical hard axis hysteresis loop for materials with PMA. The easy-axis ρ_H hysteresis loops are very similar to those of the FGT-only device shown in **Fig. 5.2** & **5.3** except that the presence of the Pt layer provides a shunting channel which reduces the ρ_H magnitude.
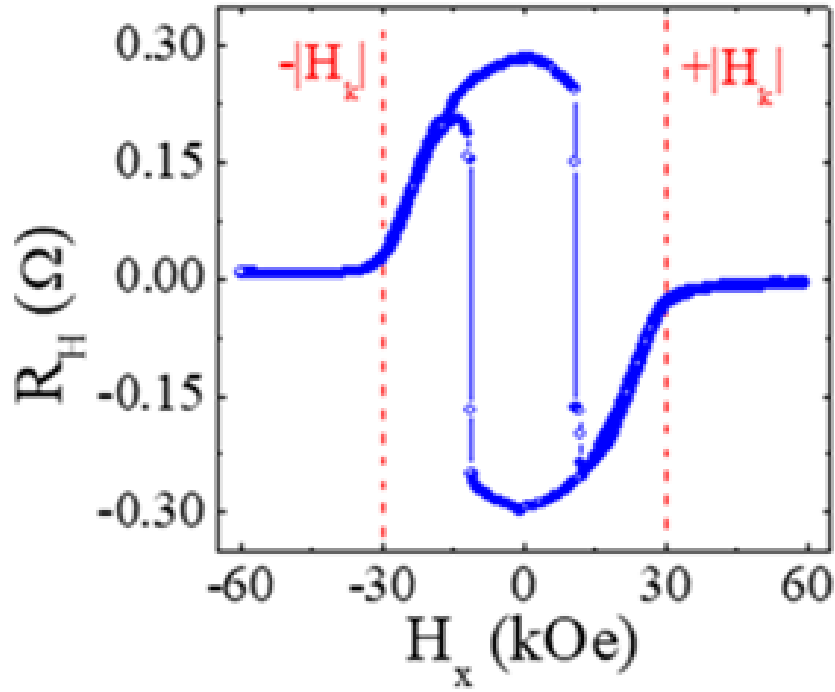
Fig. 5.5 Hard Axis AH resistance Loop. AH resistance for an applied in-plane magnetic field at 180 K for our FGT (15 nm) /Pt (5 nm) device (showing in Fig. 5.4F) with anisotropy field H_k labeled on the graph.

At $H_x = 0$, ρ_H retains the full saturation value of FGT/Pt for the easy-axis field sweeps, indicating that the initial magnetization is perpendicular to the ab-plane of the FGT. With a sufficiently strong H_x field, the magnetization is aligned to H_x which results in a vanishing ρ_H. This saturation field H_k is related to the strength of the PMA field H_u by $H_k = H_u - 4\pi M_s$. At an intermediate in-plane field $H_x = \pm 10$ kOe, the perpendicular component of the magnetization is reversed, which is caused by the incidental z-component of the applied magnetic field due to the misalignment of the applied field with the ab-plane. In our pulsed current switching experiments, we set the H_x field bias below this threshold and then apply current pulses to generate additional SOT fields to induce switching. Clearly, the effective field from the damping-like SOT, that is, HDL $\sim \sigma \times$ m, is responsible for the switching

with σ being the spin polarization direction of the spin current and m being the unit vector of the FGT magnetization. The critical current density J_c required to switch the magnetization depends on the magnitude of H_x.

The full H_x-current switching phase diagram is shown in **Fig. 5.6(C,D)** for negative and positive H_x fields, respectively. **Fig. 5.6(A,B)** shows the line cuts for three selected H_x fields: ±3, ±6, and ±9 kOe. At $H_x = -9$ kOe, switching occurs at $J_c \sim 1.5 \times 10^{11}$ A/m^2. The negative and positive in-plane fields are chosen to show the SOT switching effect in these figures because the in-plane field usually has a small Hz-component due to slight misalignment which would produce off-centered current loops if the same in-plane field is used. It is possible to generate more symmetric current loops with careful field alignment (see 5.12.5$-$5.12.7). Here the J_c value is the critical current density in Pt, which is 73.2% of the total current passing through the FGT/Pt device. This ratio is estimated based on the resistivity values of FGT and Pt (see **Fig. 5.12**) using the parallel resistor model. If the strength of H_x is decreased to 3 kOe in the negative direction, J_c increases to $\sim 2.0 \times 10^{11}$ A/m^2. We extrapolate J_c linearly to $H_x = 0$ along the line shown in **Fig. 5.6C** and find $J_c(H_x = 0) = 2.5 \times 10^{11}$ A/m^2. A similar J_c value is found for the positive H_x side, by performing the same extrapolation in **Fig. 5.6D**.
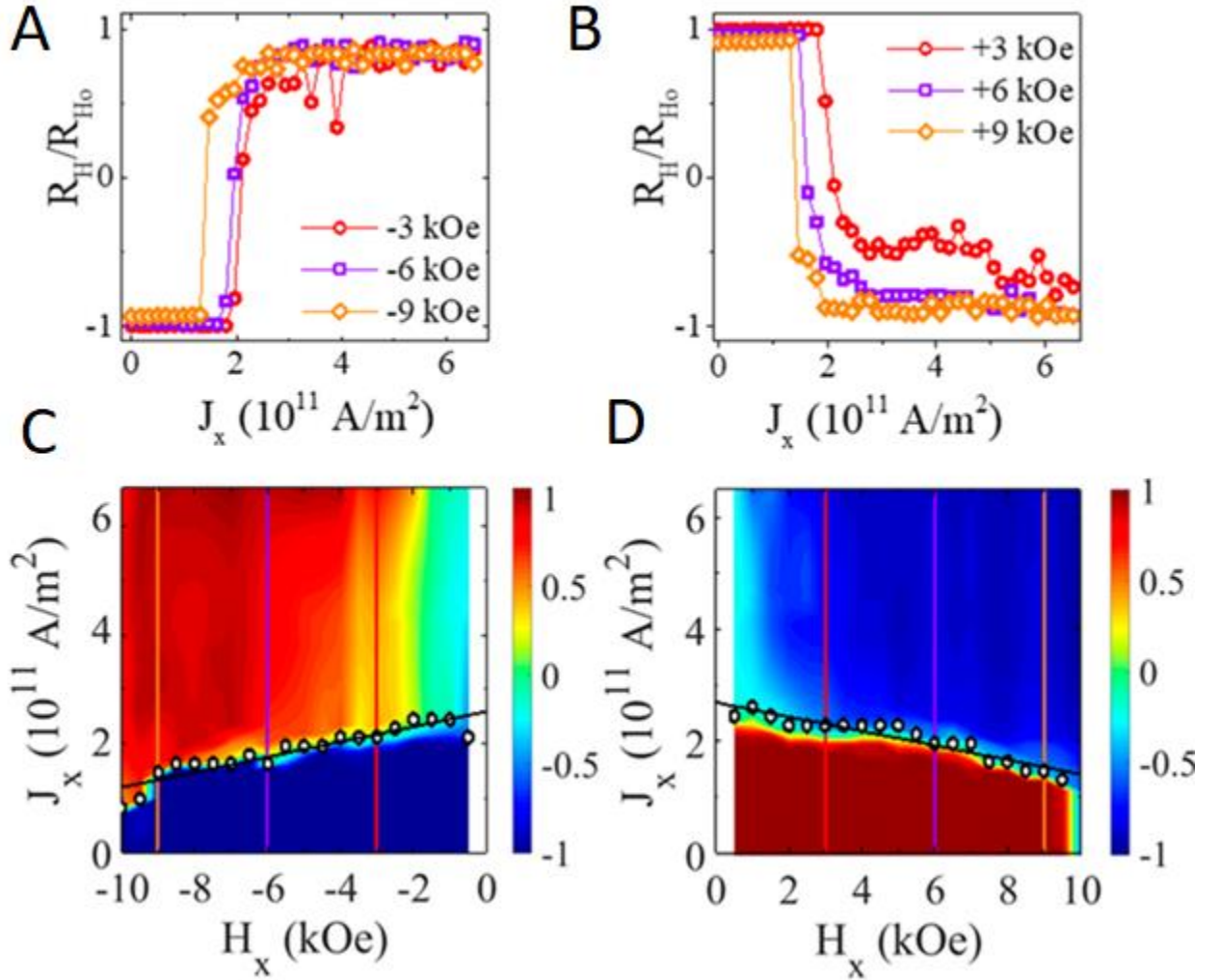
Fig. 5.6 SOT Magnetization Switching. (A−D) Effective switching current as a function of applied in-plane negative, (C), and positive, (D), bias field. The color scale represents the switching resistance as a percentage of the absolute value of the anomalous Hall resistance at zero current R_{H0}. (A,B) correspond to the line cuts in (C,D)

To compare the effectiveness of the SOT in switching, we calculate the switching efficiency parameter η using $\eta = \frac{2eM_s t H_c}{\hbar J_C(H_x=0)}$, [8] representing the ability of switching the magnetization with SOT. H_c is ~0.65 kOe for FGT at 180 K, much smaller than H_k (30 kOe), indicating that switching is by domain nucleation and domain wall depinning. If again taking the lower-bound value for M_s of 170 emu/cm^3 for our FGT/Pt device, we

obtain a minimum η value of 1.66. η can be as high as 2.2 if M_s is taken to be 225 emu/cm^3 at 180 K.[15] These η values are higher than those reported in $Tm_3Fe_5O_{12}$/W (0.95)[8] and $Tm_3Fe_5O_{12}$/Pt (0.014)[9] and suggest highly efficient SOT switching of FGT magnetization via local domain wall depinning.

5.7 Second-harmonic Hall measurements

To further quantify SOT, we perform second-harmonic (2ω) Hall measurements on FGT/Pt devices with the measurement geometry shown in Fig. 5.7. More details and application of the method were described in refs 21 and 22. We measure the 2ω responses in the Hall resistance, here ω being the frequency of the alternating current (ac) passing through the device. The 2ω signal is present only if there is a SOT acting on the magnetization. This harmonic signal is recorded as a function of a rotating in-plane magnetic field. We rotate the magnetization with an in-plane magnetic field of fixed magnitudes that are higher than H_k and measure the second harmonic Hall signal $R_H^{2\omega}$.
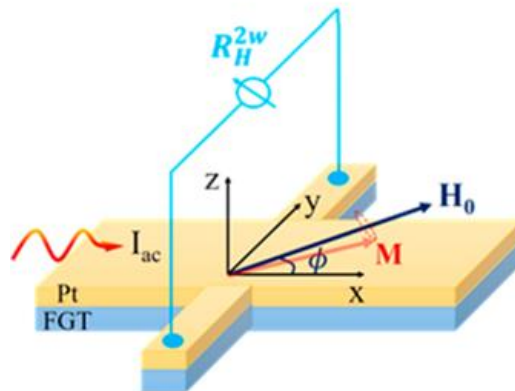

Fig. 5.7 2ω Measurement's geometry. Determination of SOT efficiency from second harmonic Hall measurements by showing schematic illustration of 2ω Hall measurement in FGT/Pt device. I_{ac}

represents the injected ac current amplitude, H_0 and M are the applied in-plane field and magnetic moment, respectively, and φ is the azimuthal angle.

As indicated in eq 5.1 below, $R_H^{2\omega}$ consists of both cos φ and cos(3φ) terms, here φ being the azimuthal angle between the magnetic field and current direction

$$R_H^{2\omega} = \left[R_{DL}^{2\omega} + R_{TH}^{2\omega} + \frac{R_{Oe}^{2\omega}+R_{FL}^{2\omega}}{2}\right] * \cos\cos\varphi + \frac{R_{Oe}^{2\omega}+R_{FL}^{2\omega}}{2} \cos\cos(3\varphi) \qquad (5.1)$$

In eq 5.1, the cos φ term contains the damping-like SOT contribution $R_{DL}^{2\omega}$ via AHE, thermoelectric contribution $R_{TH}^{2\omega}$ via anomalous Nernst effect, Oersted field contribution $R_{Oe}^{2\omega}$, and the field-like SOT contribution $R_{FL}^{2\omega}$ via the planar Hall effect. The cos(3φ) term contains the Oersted-field and the field-like SOT contributions $R_{Oe}^{2\omega} + R_{FL}^{2\omega}$. **Fig. 5.8** displays the total $R_H^{2\omega}$ signals from FGT (23 nm)/Pt (5 nm) device for different magnetic fields with the ac amplitudes of 2.2 mA and 2.4 mA in Pt, respectively. These results can be fitted very well by the cos φ-function only, indicating the negligible effect from the field-like SOT and the Oersted field, which is usually the case for ferromagnetic metal/heavy metal heterostructures. In FGT/Pt devices, the planar Hall resistance is found to be nearly 2 orders of magnitude smaller than the anomalous Hall resistance (Figure 4.14), which is the primary reason that the contributions from the field-like SOT and the Oersted field are negligibly small compared to the damping-like SOT.
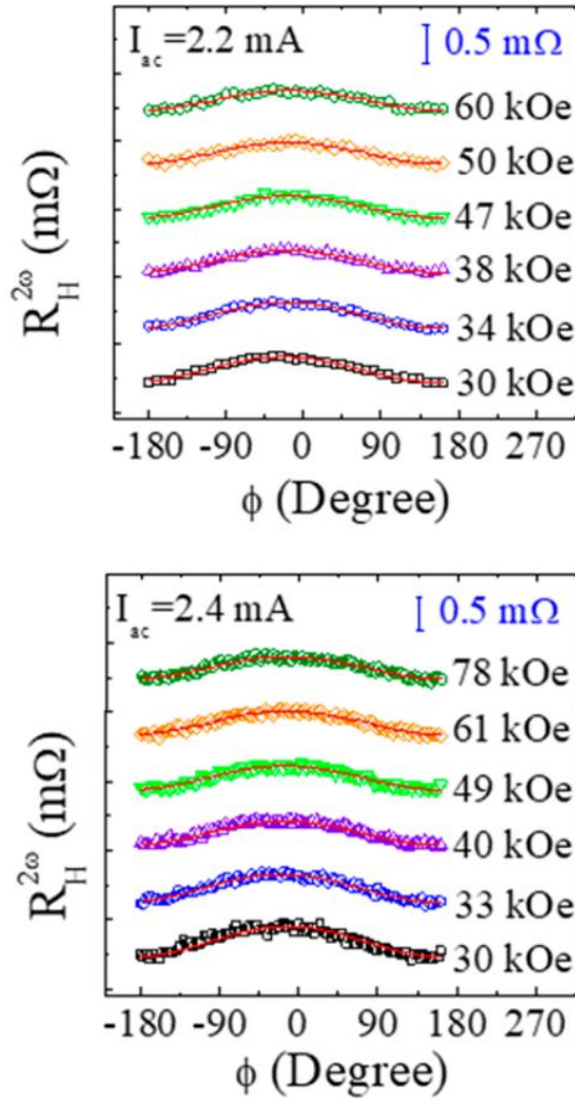
Fig. 5.8 2ω Hall measurements. The 2ω Hall resistance of a FGT (23 nm)/Pt (5 nm) device as a function of azimuthal angle for I = 2.2 mA and I = 2.4 mA. The width and the length of the Hall bar are 6 and 11 μm, respectively. Approximately 65% of the injected ac flows in Pt based on the parallel resistor model estimation. The symbols represent the raw data and red solid lines represent the fit to the theoretical model using eq 4.1.

5.8 Quantitative analysis

Further analysis of the external field strength dependence allows us to separate the damping-like SOT effect from the thermal effect, as shown in **Fig. 5.7**, which yields an effective SOT field HDL for each current. Using the smallest M_s value of 170 emu/cm^3 for FGT at 180 K, we calculate the lower-bound damping-like torque efficiency ξ_{DL} in FGT/Pt bilayer and obtain $\xi_{DL} = 0.11 \pm 0.01$ for 2.2 mA and $\xi_{DL} = 0.14 \pm 0.01$ for 2.4 mA. In our ξ_{DL} calculations, we only use the current in Pt based on the parallel resistor model; therefore, it should be valid to compare this ξ_{DL} for FGT/Pt with the available ξ_{DL} values for both ferrimagnetic insulator/heavy metal and ferromagnetic metal/ heavy metal heterostructures. We note that even the minimum ξ_{DL} value for FGT/Pt is significantly larger than ξ_{DL} in $Tm_3Fe_5O_{12}$/Pt (0.058 in ref 9 and 0.015−0.02 in ref 23). Interestingly, our minimum ξ_{DL} compares very well with the highest value of ~0.15 for CoFeB/Pt in literature.[24] Both the switching efficiency η and SOT efficiency ξ_{DL} in FGT/Pt are higher than or comparable with those in conventional SOT devices fabricated with 3D magnetic materials. It is worth pointing out that the single-domain requirement for eq 5.1 is fulfilled in the second harmonic Hall measurements, so that ξ_{DL} extracted from our experiments is reliable. By using the minimum M_s, this ξ_{DL} represents the lower bound value for SOT efficiency. The reason for this very high SOT efficiency in FGT/Pt is currently not completely understood. Here we believe that the excellent interface resulting from an atomically flat FGT surface plays an important role; therefore, the high SOT efficiency may be common to heterostructures fabricated with other vdW ferromagnets.
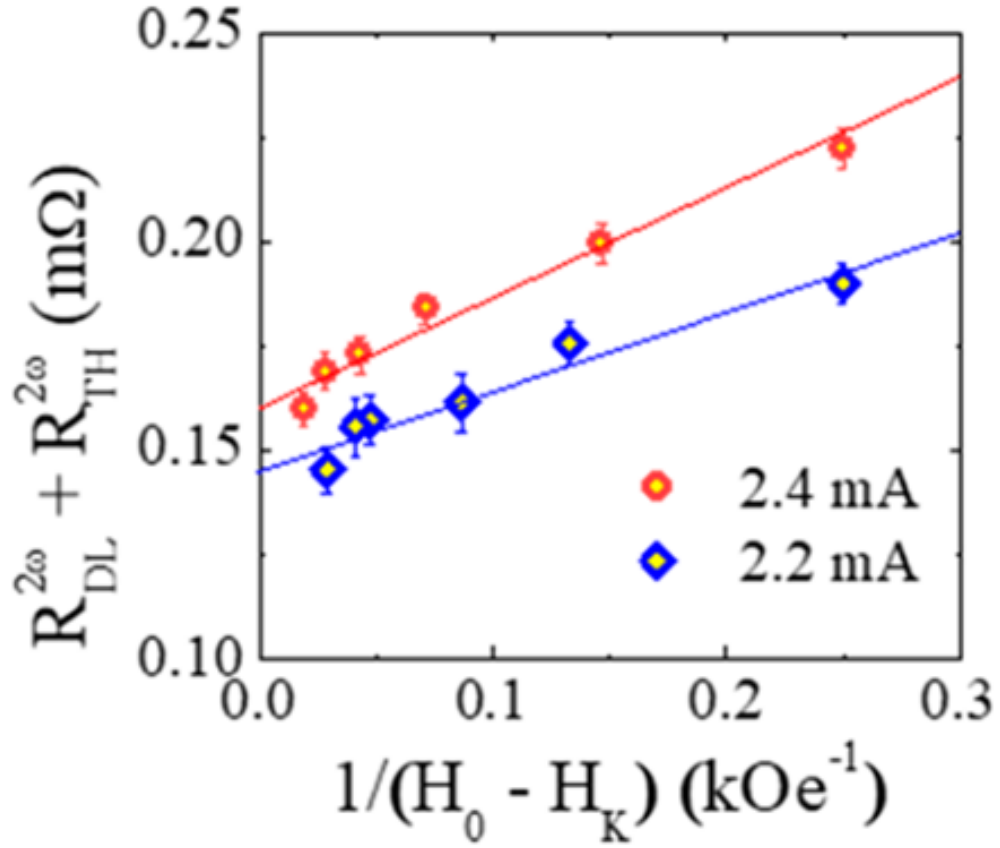
Fig. 5.9 SOT Efficiency. The amplitude of the cos(φ) coefficient from the fitting as a function of $1/(H_0 - H_K)$. H_K is 26.5 kOe at 180 K. The slope is used to determine the SOT efficiency of the system.

5.9 Summary

In summary, using both pulsed current switching and harmonic Hall measurements, we have demonstrated highly efficient SOT effects and magnetization switching in heterostructures containing a few-layer vdW ferromagnet and Pt. Because the atomic flatness of the vdW ferromagnets is an inherent property of the materials, it is expected that the high-quality interface can be retained even down to monolayers. Because of the strong

PMA, switching of monolayer FGT can be potentially achieved with a much lower critical current density, which leads to much more efficient spintronic nanodevices.

5.10 Device Fabrication

For the FGT device, the flake is exfoliated onto a Si/SiO2 substrate followed directly by spin coating 200 nm of PMMA and baking on a hot plate in air at 120 °C for 3 min. This low temperature helps protect the FGT flake from degradation and oxidation. Electrode patterns are then formed by EBL followed by sputtering a 30 nm of Pt. Before deposition of the electrodes, the contact region is plasma cleaned in the sputtering chamber with 15 W Ar plasma at a pressure of 30 mTorr for 30 s. Directly after lift-off, the device is mounted and loaded into an evacuated cryostat where the transport measurements are performed. For the FGT/Pt devices, the flakes are exfoliated onto a Si/ SiO2 substrate and instantly transferred into the load-lock of our sputtering system which is evacuated to a base pressure of 10^{-7} Torr. Once the base pressure is reached, the entire substrate is plasma cleaned with 15 W Ar plasma at a pressure of 30 mTorr for 30 s. Then a 5 nm layer of Pt is sputtered forming a continuous Pt film on the substrate. Once removed from the sputtering chamber, an optimal FGT/Pt flake is chosen by optical microscope and then EBL is performed to define an electrode pattern followed by immediate deposition of Cr(5 nm)/Au(85 nm) by electron beam evaporation. One last EBL step is then performed to define a mask to etch the FGT/Pt flake into the Hall geometry and remove all Pt connections between the electrodes. Inductively coupled plasma etching with Ar is then performed on the device and the completed device is placed into an acetone bath to remove the PMMA mask.

5.11 Electrical Transport Measurements

All transport measurements for the FGT and FGT/Pt devices are performed in the Physical Properties Measurement System by Quantum Design in a temperature range of 300 to 2 K. For the FGT device we kept a fixed current of 50 μA in the flake with a Keithley 2400 source meter which also monitored the two-terminal resistance. To monitor the longitudinal and Hall resistances, two Keithley 2182A nanovoltmeter were used. For the direct current (dc) switching measurements in the FGT/PT heterostructures, a similar setup was used to monitor the response of the Hall and longitudinal resistances whereas a Keithley 6221 ac source was used to pulse a square 0.5 microsecond dc through the device. For the 2ω Hall measurement, we fixed a constant ac at a frequency of 13.113 Hz in the device with the Keithley 6221 ac source. The 1ω and 2ω Hall responses were monitored with two Stanford Research SR830 AC lock-ins.

5.12 Discussion

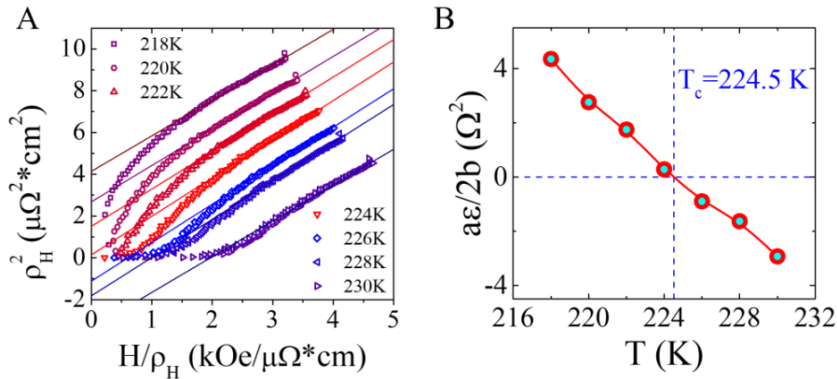### 5.12.1 Determination of Curie temperature of FGT flake by Arrott plot

Fig. 5.10 Determination of Curie temperature of FGT flake. (A) Arrott plot for determining the Curie temperature of the 53 nm thick FGT flake. (B) The y-intercept of the Arrott plot in (A) as a function of the temperature, where $\frac{a}{2b}$, is a constant and $\varepsilon = \frac{(T-T_c)}{T_c}$. The zero-crossing point is the Curie temperature.

5.12.2 Surface morphology of FGT flake determined by atomic force microscopy (AFM)
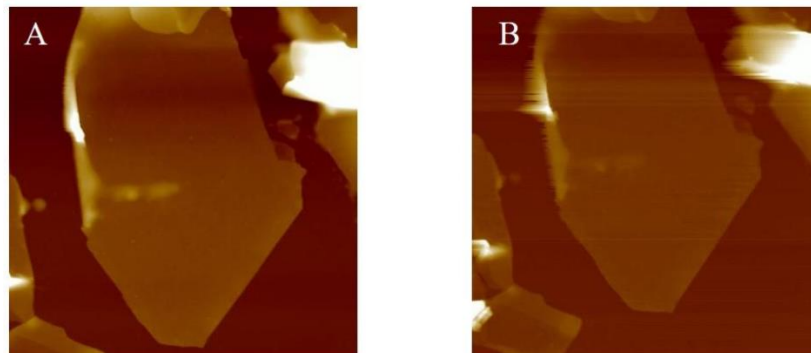

Fig. 5.11 Surface morphology of FGT flake. (A) AFM image of an exfoliated 16 nm FGT flake. (B) AFM image of the same flake after deposition of 5 nm of Pt. The rms roughness in the area within the 1 μm^2 box is 0.19 nm in (B) and 0.21 nm for the same area in (B). Since the single atomic step height of FGT is about 0.8 nm [2], we conclude that the FGT surface is atomically flat allowing for a good interface to form between FGT and Pt.

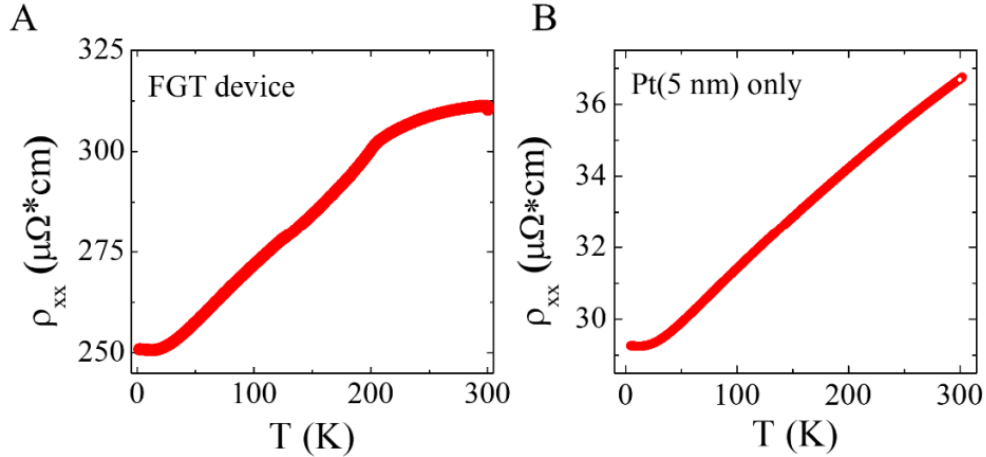## 5.12.3 Longitudinal resistivity of FGT flake and Pt film

Fig. 5.12 Resistivity vs. temperature of FGT and Pt. (A) Temperature dependence of the longitudinal resistivity ρ_{xx} of a 53 nm thick FGT device. (B) Temperature dependence of ρ_{xx} of a 5 nm thick Pt device. These two sets of resistivity data are used to estimate the current that is shunted into the FGT layers.
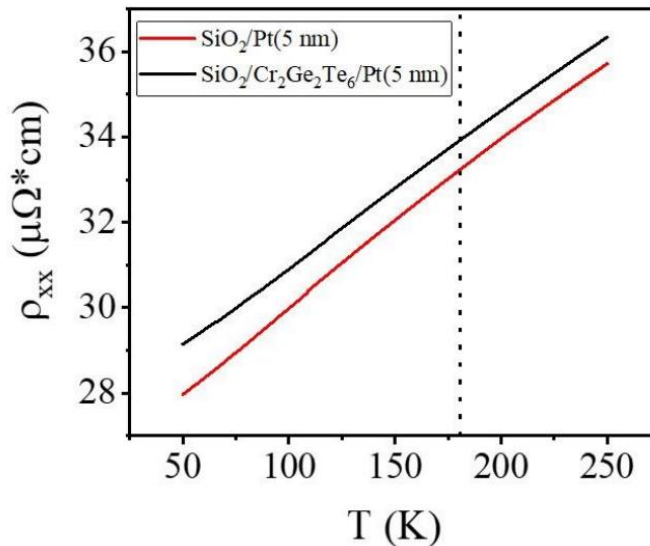

Fig. 5.13 Comparison of resistivity for 5 nm Pt Hall bar devices on SiO$_2$ vs. CGT. Longitudinal resistivity ρ_{xx} as a function of temperature for 5 nm Pt on SiO$_2$ and on CGT. The SiO$_2$/Pt (5 nm) device has a channel width of 6 µm and the distance between the contacts used to measure resistivity is 4 µm. The SiO$_2$/CGT/Pt (5 nm) device has a channel width of 5.5 µm and the distance between the contacts used to measure resistivity is 11 µm. Both devices were measured at the same bias current of 0.2 mA while the system was cooled down.

The resistivity of 53 nm FGT flakes in **Fig. 5.13(A)** shows a slight decrease from 310 μΩ.cm at 300 K to 305 μΩ.cm at 230 K and a more rapid decrease to 250 μΩ.cm at 2 K. The steep drop at 230 K coincides with the ferromagnetic phase transition. The FGT resistivity value we measured is relatively lower than the previously reported values, e.g., 615 μΩ.cm [1], 395 μΩ.cm [17] at 180 K. This lower variation is attributed to impurities and defects in FGT. The resistivity of 5 nm Pt shown in in Figure 4.12(A) decreases from 37 μΩ.cm at 300 K to 29.5 μΩ.cm at 2 K. We used the FGT resistivity of 285 μΩ.cm and Pt resistivity of 33.5 μΩ.cm at 180 K to estimate the current shutting in FGT. This allows us to estimate the percentage of the current that flows in Pt which is responsible for the SOT.

$Cr_2Ge_2Te_6$ (CGT) is a layered van der Waals ferromagnet which is similar to FGT but a semiconductor. Atomically smooth interface can be obtained in freshly cleaved CGT flakes. Because of the high resistivity, the current in CGT/Pt heterostructures is nearly completely circuited by the Pt layer. Therefore, the resistivity of Pt in FGT/Pt is expected to be similar to that in CGT/Pt, which offers a good way of estimating the resistivity of Pt in FGT/Pt. Our measurement shows that Pt (5 nm) on CGT has the similar resistivity to Pt (5 nm) on SiO2, which allows us to estimate the effective current flowing in Pt in FGT/Pt using the parallel resistor model.

5.12.4 Anomalous Hall resistivity and planar Hall resistivity of FGT flake
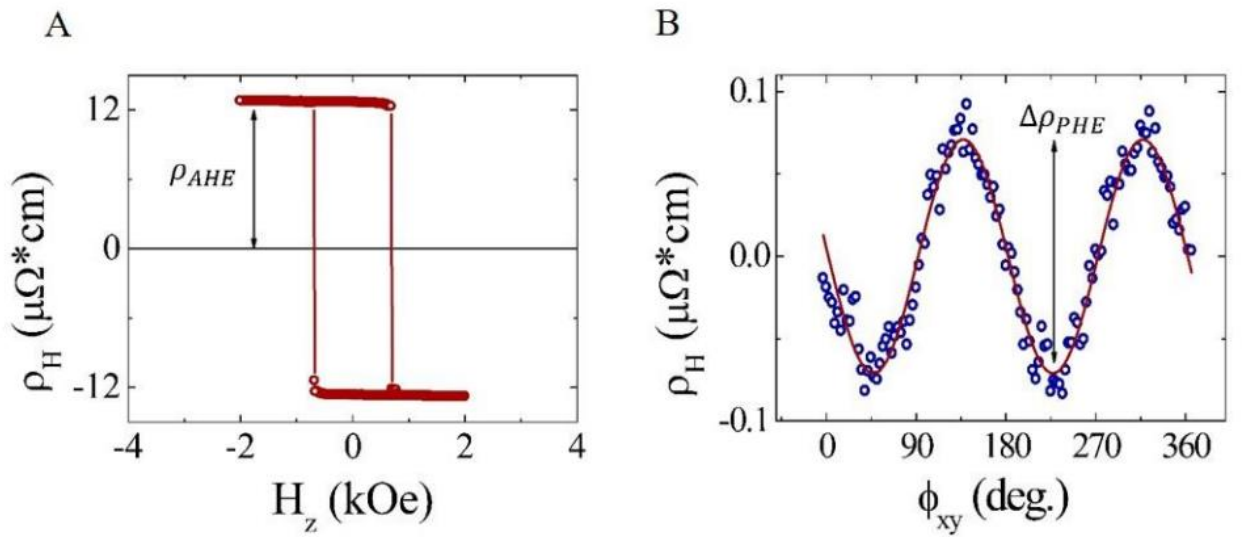

Fig. 5.14 Comparison of AHE and PHE resistivities of 53 nm FGT flake. (A) Hall resistivity as a function of the magnetic field applied along the z axis. We determine the AHE resistivity to be, $\rho_{AHE} = 12.7$ $\mu\Omega$*cm. (B) Hall resistivity as a function of the azimuthal angle with a fixed magnetic field, H = 80 kOe. A $\cos(\varphi)$ term due to the slight misalignment was removed. We determine the PHE resistivity to be, $\Delta\rho_{PHE} = 0.178$ $\mu\Omega$*cm. Both measurements were performed on the FGT device pictured in the inset of Fig. 4.3 with a fixed bias current, I = 0.1 mA, at T = 180 K.

5.12.5 Precise determination of in-plane magnetic field orientation by anomalous Hall signal
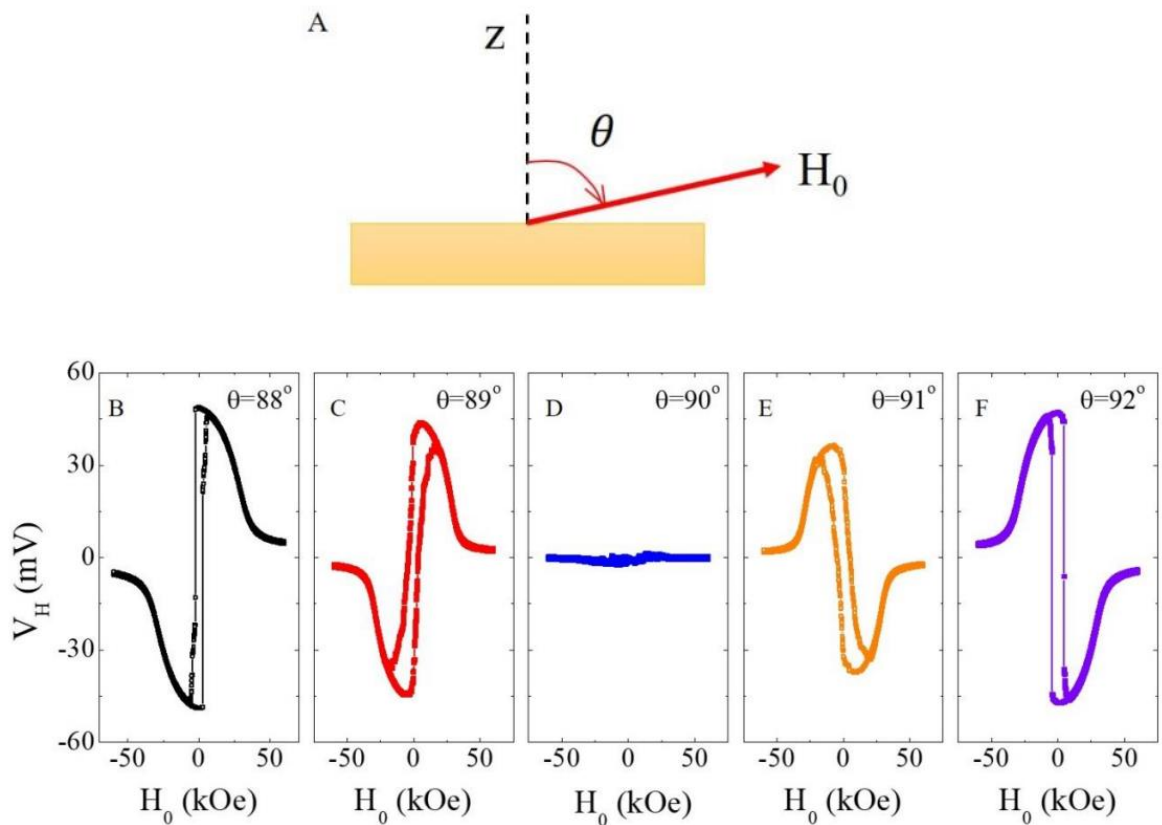

Fig. 5.15 Demonstration of the magnetic field alignment in the film plane. (A) Definition of the field orientation using angle θ. The anomalous Hall signal of one FGT/Pt device as a function of the applied magnetic field with $\theta = 88^o$ (B), 89° (C), 90° (D), 91° (E) and 92° (F), the DC current is 0.1 mA.

Here we demonstrate how to align the magnetic field with respect to the FGT/Pt device plane by monitoring the anomalous Hall signal. As shown in **Fig. 4.15**, the anomalous Hall signal of the FGT/Pt device changes sign once the magnetic field tilt an angle (1° or 2°) above and below the device plane. The precise field angle is determined by the saturated Hall signal value with respect to the full Hall signal when the field is applied along the z-axis. When the magnetic field is aligned perfectly in the device plane, multi domains are formed when the field is reduced from 6 T to 0 T. Nearly zero anomalous Hall signal is observed due to the equal distribution of the up and down-domains (Fig. 4.15(D)).

5.12.6 Magnetization switching via domains under pulsed current and bias magnetic field
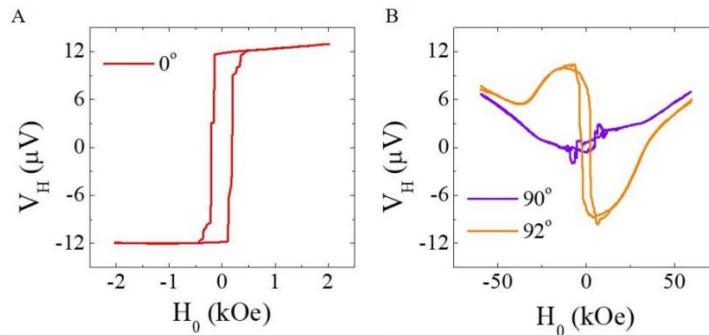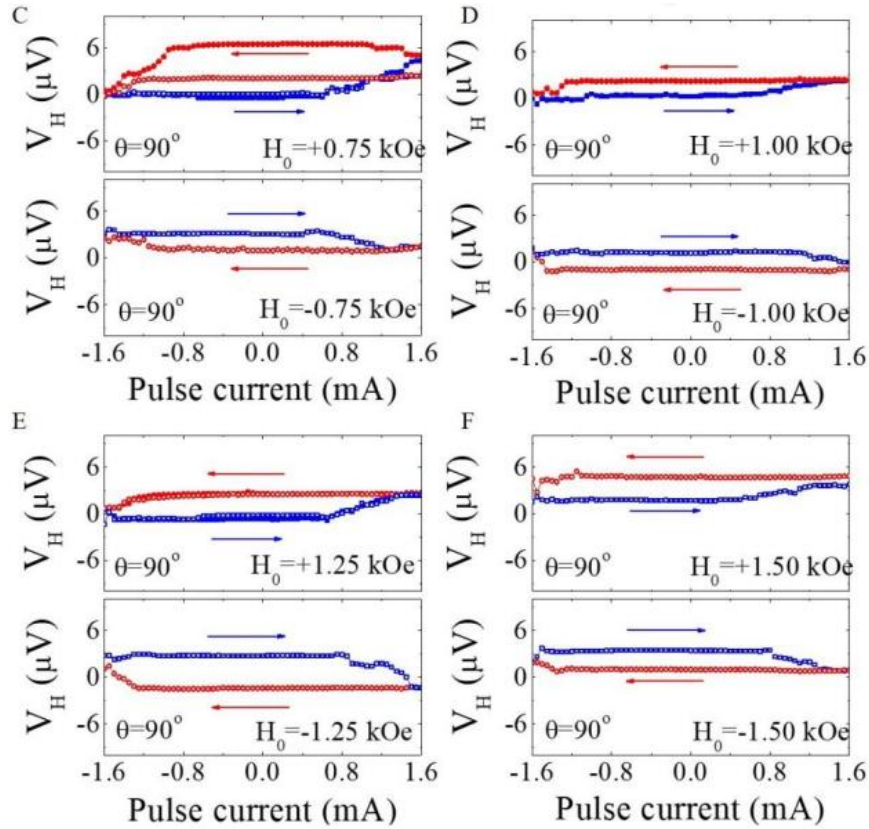
Fig. 5.16 Current induced magnetization switching for the FGT (19 nm)/Pt (5 nm) bilayer device at 180 K. (A) Anomalous Hall signal as a function of an out-of-plane magnetic field. (B) Anomalous Hall signal as a function of magnetic field with angles of 90 and 92 degrees to the z-axis. The symmetric background is from a mixture of the longitudinal magnetoresistance. Current induced magnetization switching under in-plane ($\theta = 90^o$) magnetic fields of ∓ 0.75 kOe (C), ∓ 1.00 kOe (D), ∓ 1.25 kOe (E) and ∓ 1.50 kOe (F). Arrows indicate the current scan directions. The in-plane magnetic field is aligned along the current direction. The width of the Pt Hall bar is 0.5 µm.

Here we demonstrate that the current-induced magnetization switching highly involves magnetic domain formation and movement. **Fig. 5.16(A)** shows the anomalous Hall signal of a FGT (19 nm)/Pt (5 nm) device. The squared loop indicates strong perpendicular magnetic anisotropy (PMA). This device is different from the device shown in **Fig. 5.15**. There is a longitudinal magnetoresistance signal mixed in the Hall signal, which can be clearly seen in the field-symmetric background **Fig. 5.16(B)**. **Fig. 5.16 (C)-(F)** presents the

current-induced magnetization switching under different in-plane magnetic field strengths. First of all, the change of anomalous Hall signal under pulsed currents is smaller than its full magnitude (as shown in **Fig. 5.16 (A)**). Only 8.9~29% of the magnetic domains are switched, which may be due to the fact that this FGT flake is too thick (~ 19 nm) and a larger critical current is needed to switch all domains. We did not apply very large current to avoid damaging the device. The critical current density required to switch the magnetization is ~3.2×10^{11} A/m^2 if we assume that all the current flows in the Pt layer (width is 0.5 µm and thickness is 5 nm), but the real value of current density is much lower than that because of the current-shunting effect of the relatively thick FGT layer. Second, the nearly symmetric V_{xy} vs. current loop can be observed under a fixed magnetic field. Third, the anomalous Hall loop changes its chirality when we reverse the magnetic field, which is consistent with the physical picture of SOT-induced magnetization switching. Above all, here we demonstrate that the current-induced magnetization switching in a thick FGT is a highly multi-domain process. Although only partial domain switching is shown in this figure for a relatively thick device, the physical picture of SOT for thinner devices should still be applicable.

5.12.7 Effect of tilting angle of magnetic field on current induced magnetization switching

Here we study the effect of field-orientation on current-induced magnetization switching. As we know, there is always a small H_z component when the field is not perfectly aligned in the sample plane. This H_z component may favor or disfavor the switching process and act like a bias.

However, without help of a DC current, if the in-plane field is below a threshold value, the small Hz field alone cannot switch the magnetization. Since in our **Fig. 5.5**, the tilting angle is around 1.48º, so here we also check the current-induced magnetization switching under a tilted magnetic field. As shown in **Fig. 5.17**, the effect of tilting angle on switching current is not obvious in this partial switching experiment. Clearly, the domain nucleation process is not so sensitive to the small tilting angle of the applied magnetic field.
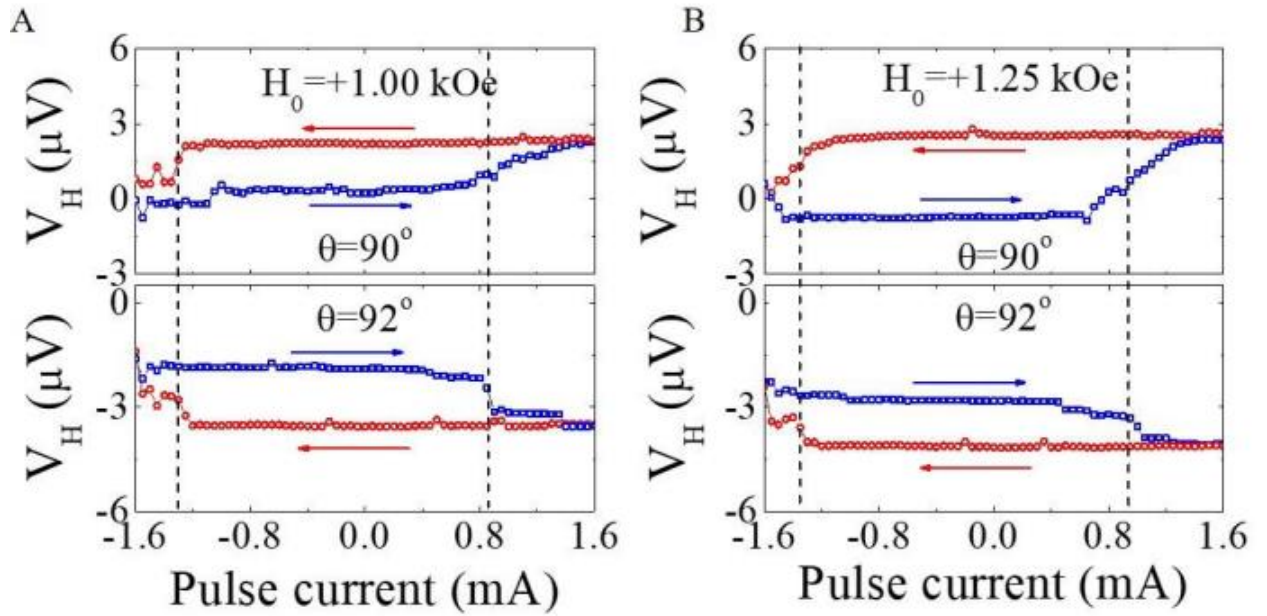
Fig. 5.17 Effect of the tilting angle of magnetic field on current induced magnetization switching. (A) Anomalous Hall signal as a function of current under the magnetic field of 1 kOe with different title angles, i.e., $\theta = 90^o$ and 92°. (B) Anomalous Hall signal as a function of current under the magnetic field of 1.25 kOe with different title angles, i.e., $\theta = 90^o$ and 92°. The experiments are performed at 180 K. The chiralities of the current-dependence loops for 90° and 92° are opposite is due to different initial magnetic states.

References

1. Fei, Z.; Huang, B.; Malinowski, P.; Wang, W.; Song, T.; Sanchez, J.; Yao, W.; Xiao, D.; Zhu, X.; May, A. F.; Wu, W.; Cobden, D. H.; Chu, J.; Xu, X. Two-dimensional itinerant ferromagnetism in atomically thin Fe3GeTe2. Nat. Mater. 2018, 17, 778−782.

2. Deng, Y.; Yu, Y.; Song, Y.; Zhang, J.; Wang, N. Z.; Sun, Z.; Yi, Y.; Wu, Y. Z.; Wu, S.; Zhu, J.; Wang, J.; Chen, X. H.; Zhang, Y. Gatetunable room-temperature ferromagnetism in two-dimensional Fe3GeTe2. Nature 2018, 563, 94−99.

3. Gong, C.; Li, L.; Li, Z.; Ji, H.; Stern, A.; Xia, Y.; Cao, T.; Bao, W.; Wang, C.; Wang, Y.; Qiu, Z. Q.; Cava, R. J.; Louie, S. G.; Xia, J.; Zhang, X. Discovery of intrinsic ferromagnetism in two-dimensional van der Waals crystals. Nature 2017, 546, 265−269.

4. Huang, B.; Clark, G.; Navarro-Moratalla, E.; Klein, D. R.; Cheng, R.; Seyler, K. L.; Zhong, D.; Schmidgall, E.; McGuire, M. A.; Cobden, D. H.; Yao, W.; Xiao, D.; Jarillo-Herrero, P.; Xu, X. Layer-dependent ferromagnetism is van der Waals crystals down to the monolayer limit. Nature 2017, 546, 270−273.

5. Liu, S.; Yuan, X.; Zou, Y.; Sheng, Y.; Huang, C.; Zhang, E.; Ling, J.; Liu, Y.; Wang, W.; Zhang, C.; Zou, J.; Wang, K.; Xiu, F. Wafer-scale two-dimensional ferromagnetic Fe3GeTe2 thin films were grown by molecular beam epitaxy. 2D Mater. Appl. 2017, 1, 30.

6. Ma, Q.; Li, Y.; Gopman, D. B.; Kabanov, Y .P..; Shull, R. D.; Chien, C. L. Switching a Perpendicular Ferromagnetic Layer by Competing Spin Currents. Phys. Rev. Lett. 2018, 120, 117703.

7. Chen, Y.; Takahashi, S.; Nakayama, H.; Althammer, M.; Goennenwein, S. T. B.; Saitoh, E.; Bauer, G. E. W. Theory of spin Hall magnetoresistance. Phys. Rev. B: Condens. Matter Mater. Phys. 2013, 87, 144411.

8. Shao, Q.; Tang, C.; Yu, G.; Navabi, A.; Wu, H.; He, C.; Li, J.; Upadhyaya, P.; Zhang, P.; Razavi, S. A.; He, Q. L.; Liu, Y.; Yang, P.; Kim, S. K.; Zheng, C.; Liu, Y.; Pan, L.; Lake, R. K.; Han, X.; Tserkovnyak, Y.; Shi, J.; Wang, K. L. Role of dimensional crossover on spin-orbit torque efficiency in magnetic insulator thin films. Nat. Commun. 2018, 9, 3612.

9. Li, J.; Yu, G.; Tang, C.; Liu, Y.; Shi, Z.; Liu, Y.; Navabi, A.; Aldosary, M.; Shao, Q.; Wang, K. L.; Lake, R.; Shi, J. Deficiency of the bulk spin Hall effect model for spin-orbit torques in magnetic insulator/heavy-metal heterostructures. Phys. Rev. B: Condens. Matter Mater. Phys. 2017, 95, No. 241305.

10. Zhang, Y.; Lu, H.; Zhu, X.; Tan, S.; Feng, W.; Liu, Q.; Zhang, W.; Chen, Q.; Liu, Y.; Luo, X.; et al. Emergence of Kondo lattice behavior in a van der Waals itinerant ferromagnet. Sci. Adv. 2018, 4, No. eaao6791.

11. May, A. F.; Calder, S.; Cantoni, C.; Cao, H.; McGuire, M. A. Magnetic structure and phase stability of the van der Waals bonded ferromagnet Fe3−xGeTe2. Phys. Rev. B: Condens. Matter Mater. Phys. 2016, 93, 014411.

12. Drachuck, G.; Salman, Z.; Masters, M. W.; Taufour, V.; Lamichhane, T. N.; Lin, Q.; Straszheim, W. E.; Bud'ko, S. L.; Canfield, P. C. Effect of nickel substitution on magnetism in the layered van der Waals ferromagnet Fe3GeTe2. Phys. Rev. B: Condens. Matter Mater. Phys. 2018, 98, 144434.

13. Deiseroth, H.-J.; Aleksandrov, K.; Reiner, C.; Kienle, L.; Kremer, R. K. Fe3GeTe2 and Ni3GeTe2□two new layered transition metal compounds: crystal structures, HRTEM investigations, and magnetic and electrical properties. Eur. J. Inorg. Chem. 2006, 2006, 1561−1567.

14. Chen, B.; Yang, J.; Wang, H.; Imai, M.; Ohta, H.; Michioka, C.; Yoshimura, K.; Fang, M. Magnetic properties of layered itinerant electron ferromagnet Fe3GeTe2. J. Phys. Soc. Jpn. 2013, 82, 124711.

15. Leon-Brito, N.; Bauer, E. D.; Ronning, F.; Tompson, J. D.; Movshovich, R. Magnetic microstructure and magnetic properties of uniaxial itinerant ferromagnet Fe3GeTe2. J. Appl. Phys. 2016, 120, 083903.

16. Verchenko, V.; Tsirlin, A.; Sobolev, A.; Presniakov, I.; Shevelkov, A. Ferromagnetic Order, Strong Magnetocrystalline Anisotropy, and Magnetocaloric Effect in the Layered Telluride Fe3−δGeTe2. Inorg. Chem. 2015, 54, 8598.

17. Wang, Y.; Xian, C.; Wang, J.; Liu, B.; Ling, L.; Zhang, L.; Cao, L.; Qu, Z.; Xiong, Y. Anisotropic anomalous Hall effect in triangular itinerant ferromagnet Fe3GeTe2. Phys. Rev. B: Condens. Matter Mater. Phys. 2017, 96, 134428.

18. Yi, J.; Zhuang, H.; Zou, Q.; Wu, Z.; Cao, G.; Tang, S.; Calder, S. A.; Kent, P. R. C.; Mandrus, D.; Gai, Z. Competing antiferromagnetism in a quasi-2D itinerant ferromagnet: Fe3GeTe2. 2D Mater. 2017, 4, 011005.

19. Tan, C.; Lee, J.; Jung, S.; Park, T.; Albarakati, S.; Partridge, J.; Field, M. R.; McCulloch, D. G.; Wang, L.; Lee, C. Hard magnet properties in nanoflake van der Waals Fe3GeTe2. Nat. Commun. 2018, 9, 1554.

20. Zhang, X.; Zhao, Y.; Song, Q.; Jia, S.; Shi, J.; Han, W. Magnetic anisotropy of the single-crystalline ferromagnetic insulator Cr2Ge2Te6. Jpn. J. Appl. Phys. Part 1 2016, 55, 033001.

21. Garello, K.; Miron, I. M.; Avci, C. O.; Freimuth, F.; Mokrousov, Y.; Blugel, S.; Auffret, S.; Boulle, O.; Gaudin, G.; Gambardella, P. Symmetry and magnitude of spin-orbit torques in ferromagnetic heterostructures. Nat. Nanotechnol. 2013, 8, 587.

22. Avci, C. O.; Garello, K.; Gabureac, M.; Ghosh, A.; Fuhrer, A.; Alvarado, S. F.; Gambardella, P. Interplay of spin-orbit torque and thermoelectric effects in ferromagnet/normal-metal bilayers. Phys. Rev. B: Condens. Matter Mater. Phys. 2014, 90, 224427.

23. Avci, C. O.; Quindeau, A.; Pai, C.; Mann, M.; Caretta, L.; Tang, A. S.; Onbasli, M. C.; Ross, C. A.; Beach, G. S. D. Current-induced switching in a magnetic insulator. Nat. Mater. 2017, 16, 309.

24. Pai, C.; Mann, M.; Tan, A. J.; Beach, G. S. D. Determination of spin torque efficiencies in heterostructures with perpendicular magnetic anisotropy. Phys. Rev. B: Condens. Matter Mater. Phys. 2016, 93, 144409.

Appendix

A.1 List of the measured devices

All of the measured devices in the dissertation were fabricated in the UCR facilities. The FGT and FG2T crystals were grown in the chemistry department. Microscope pictures of the devices are the figures below with scale bars. Atomic force microscope from Veeco Dimension 5000 was used to find the thickness of the devices.
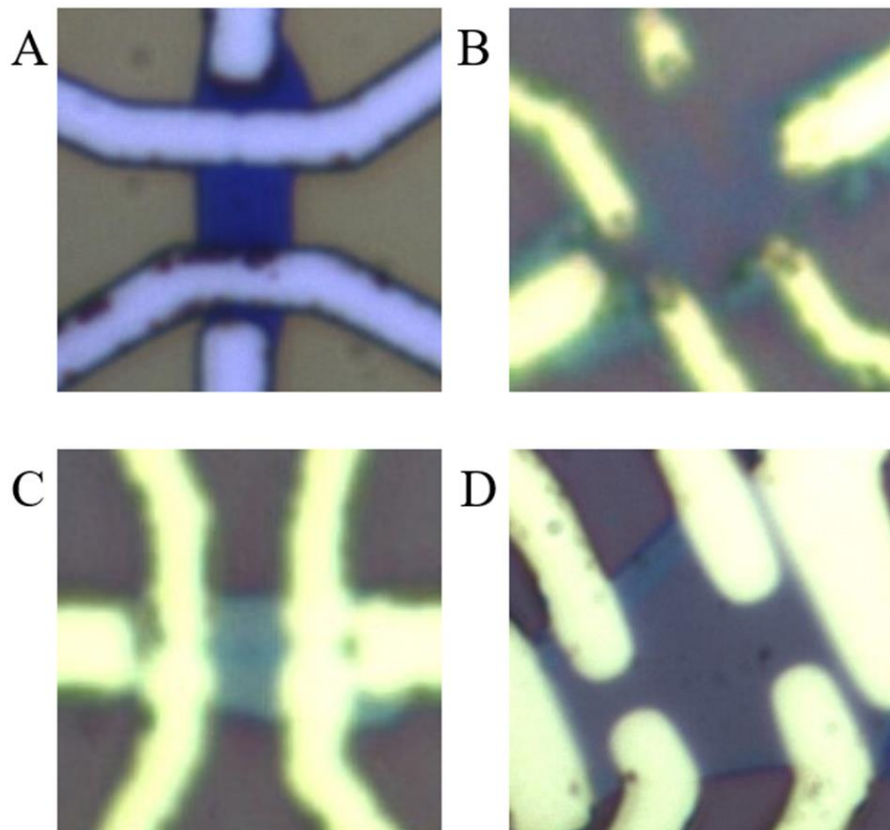

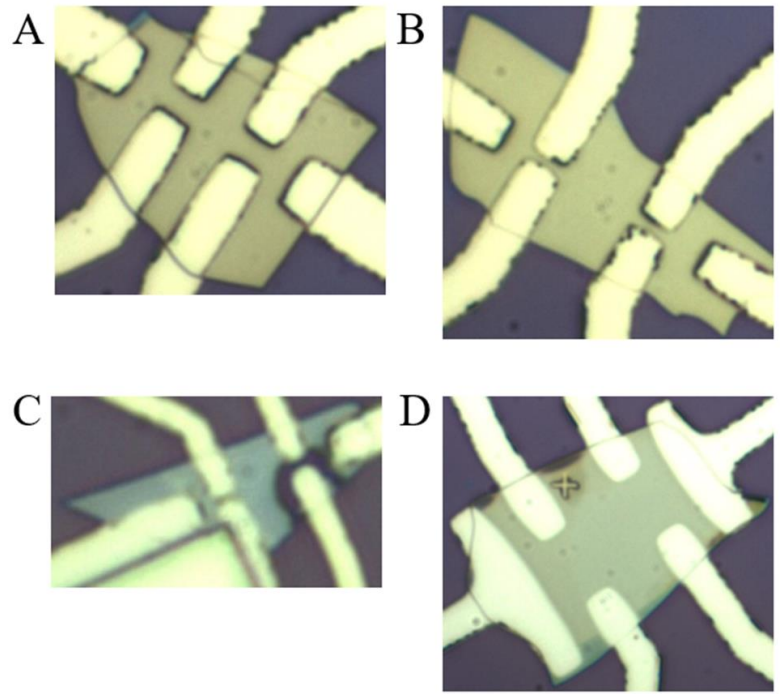**Fig. A.1 Microscope picture of selected Devices of FG2T.** (A) 1L, (B) 3L, (C) 6L, (D) 5L.

Fig. A.2 Microscope picture of selected Devices of FG2T. (A) 135L, (B) 53L, (C) 12L, (D) 20L.
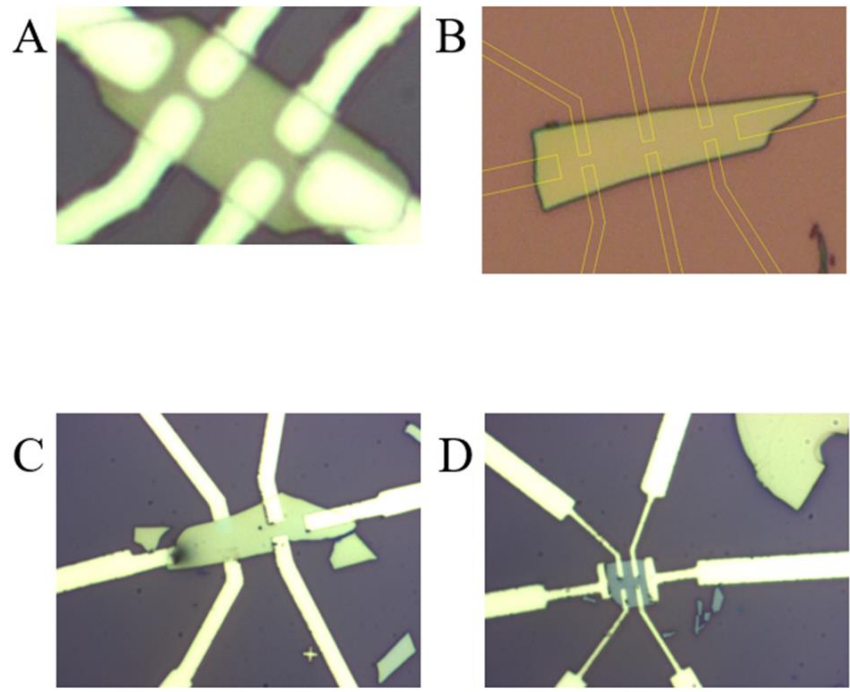
Fig. A.3 Microscope picture of selected Devices of FG2T. (A) 75L, (B) 30L, (C) 22L, (D) 18L.
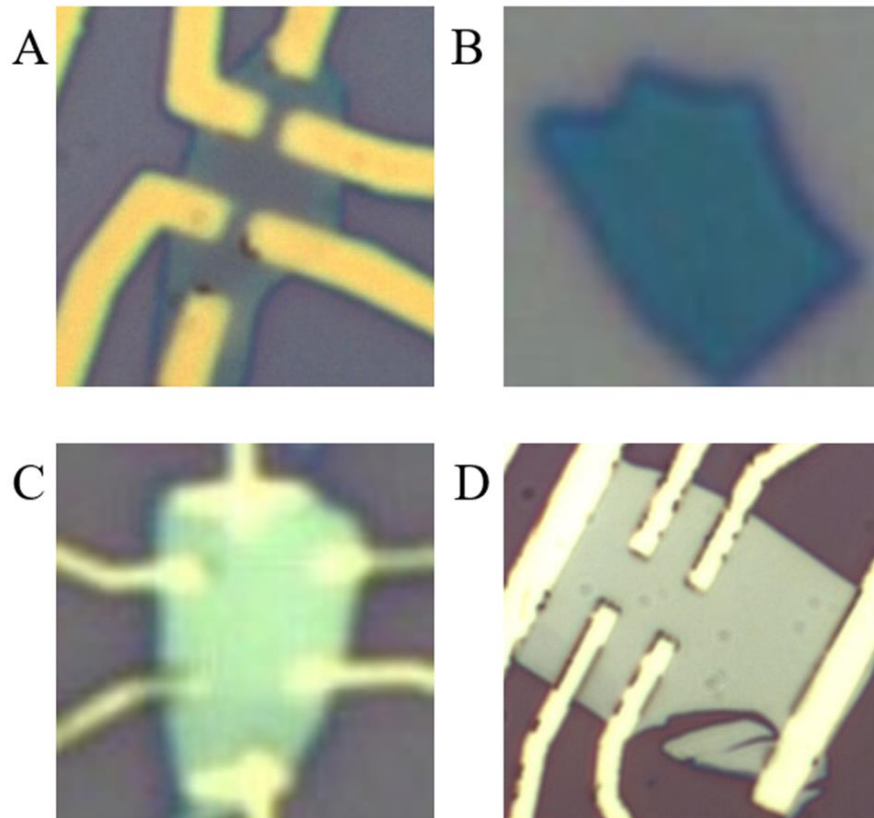

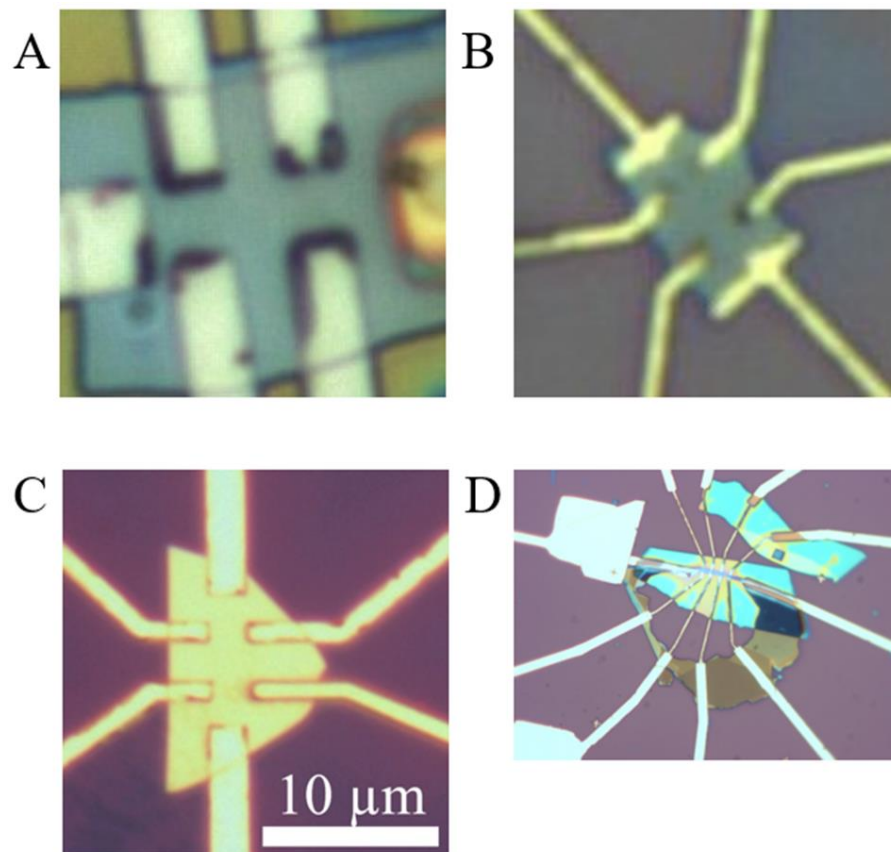**Fig. A.4 Microscope picture of selected Devices of FGT.** (A) 3L, (B) 4L, (C) 11L, (D) 22L.

Fig. A.5 Microscope picture of selected Devices of FGT. (A) 42L, (B) 12L, (C) 41L, (D) 9L.